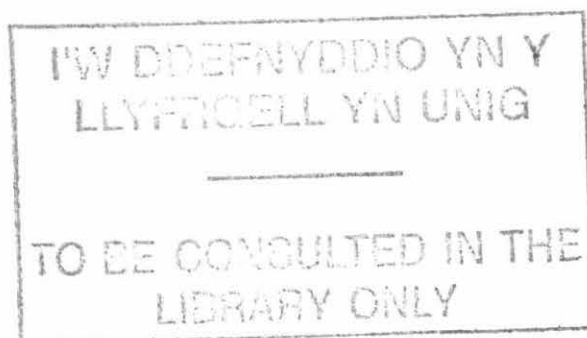# Analysis and Design of Organic

Semiconductor Lasers

Submitted by Guy F. Barlow for the degree of PhD

University of Wales, Bangor

April 20, 2001

Summary

There is much current interest in the use of organic materials for applications in the opto-electronics industry. This thesis is concerned with the investigation into the theoretical properties of so called Organic Semiconductor Lasers (OSLs), which may have applications in display technologies and low-power communications as a low cost alternative to inorganic devices.

The work presented in this thesis represents, to the best knowledge of the author, the only theoretical investigation of OSL's to date. Many of the physical processes associated with the electrical excitation of OSLs are yet to be understood completely, the analyses in this thesis are therefore mainly concerned with the optical properties and lasing thresholds of the OSL structures, demonstrating how the differing optical properties of organic compared to in-organic materials effect the performance of various device configurations. This analysis is extended to theoretical devices such as Circular Grating CG-DFB OSLs, which are yet to be demonstrated experimentally.

Due to well published and thorough experimental investigation of a certain group of materials, the $Alq_3 : DCM$ combination, it has recently become possible to begin to investigate the lasing thresholds of these lasers in terms of the amount of current they would require under electrical pumping schemes. Initial data showing how the threshold current is affected by changes in the geometry of a range of devices is also presented.

To Tabitha and my Parents

Acknowledgements

Contents

1

2

3

Chapter 1

Introduction

1.1 Organic Materials and Their Properties

1.1.1 Definition of Organic Semiconductor Materials

The *Organic Semiconductor* materials referred to in this thesis are composed of low molecular weight [1] organic molecules. The structure of *tris-(8-Hydroxyquinolene) Aluminium* (Alq$_3$), the material of most interest in this thesis, is shown in Figure 1.1. The molecule is constructed around a central Aluminium atom, with three Quinolate *ligands* arranged symmetrically around it. Each ligand is identical, being composed of two adjoined carbon rings.
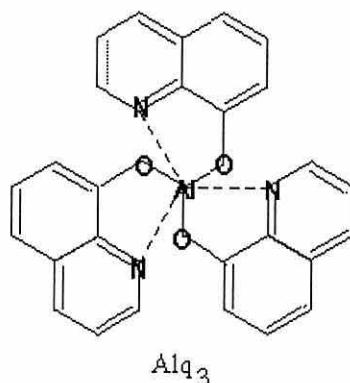
Figure 1.1: *Molecular structure of Alq$_3$*

The Organic Semiconductor Laser (OSL) devices discussed in this thesis use amorphous organic semiconductor materials, the molecules are not arranged in any order in the bulk material and only relatively weak intermolecular forces allow interaction between adjacent molecules. Unlike crystalline materials therefore, the properties of the bulk material are largely governed

---

[1]i.e. of small physical size compared to polymer materials for example, which are said to be of large molecular weight

by the properties of the individual molecules. The random orientation of the molecules ensures that the electromagnetic properties of the material are isotropic.

Figure 1.1 shows that each ligand is composed primarily of carbon atoms, with alternating single and double bonds between them. The alternating bond structure, known as *conjugation*, results in de-localisation of the bonding (valence) electrons in the molecule. Each molecule can therefore be thought of as a miniature crystal, and the allowed electronic wave-functions (or *molecular orbitals*) correspond approximately to the energy levels of a crystalline semiconductor material. Depending on the structure of the molecule, a 'band gap' may result between the *Highest Occupied Molecular Orbital* (HOMO) and the *Lowest Unoccupied Molecular Orbital* (LUMO), which can be compared to the valence and conduction band of a semiconductor crystal.

1.1.2 Optoelectronic Properties of Organic Materials

In comparison to in-organic semiconductor materials, organic semiconductors exhibit considerably lower indexes of refraction, typically of about 1.5. The other optical properties of organic semiconductor materials are therefore largely a result of the arrangement of the HOMO and LUMO. As these energy levels are created by the formulation of the molecule, and even the physical orientation of the atoms from which it is comprised, it is theoretically possible to alter the spacing of the HOMO and LUMO by adjusting the chemistry of the molecule, which is an attractive advantage of organic

materials for the design of low cost lasers operating at wavelengths difficult to obtain using crystalline in-organic semiconductors.
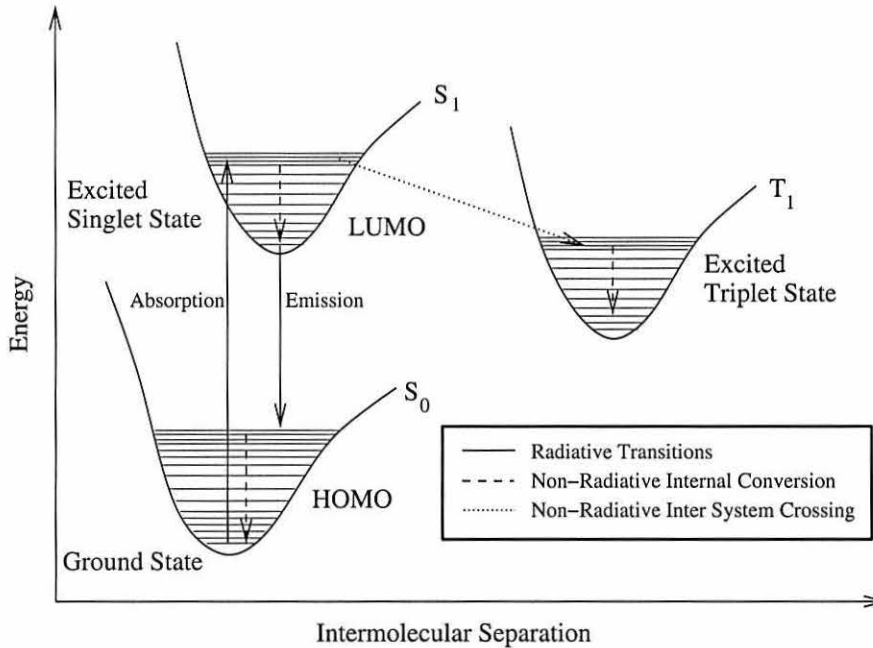
Figure 1.2: *Energy levels in an organic semiconductor material.*

Absorption and emission of photons is accompanied by upward or downward transitions of available electrons in the molecule between the HOMO and LUMO levels (Figure 1.2). The HOMO and LUMO are broadened by numerous energy levels representing vibrionic states of the molecule and transitions between these states are non-radiative. An electron excited from the bottom of the HOMO to the top of the LUMO energy level decays rapidly to the bottom of the LUMO via vibrionic (phonon) transitions in a process known as *Internal Conversion* (IC). Emission of radiation is then accompanied by a downward transition from the bottom of the LUMO to the top of the HOMO. The result of non-radiative IC is a significant difference in the

9

absorption and emission energies, resulting in a large *Stokes* shift between the singlet absorption and emission spectra of organic semiconductors. The allowed energies of an organic semiconductor molecule therefore form a natural four level laser system, and very little of the emission radiation of the laser is re- absorbed into the material under stimulated emission.

There is approximately a 70% probability that, instead of decaying radiatively to the ground state orbital, an excited molecule will decay non-radiatively into a *triplet* state via a non-radiative process known as *Inter System Crossing* (ISC). The decay time of the triplet state is comparatively long and triplet absorption results in the quenching of any optical gain if the pump is constant. Even optically pumped Organic Semiconductor Lasers (OSLs) are generally operated on a pulsed basis. In [16], for example, a 337nm nitrogen gas laser is used to supply the pump energy in $1ns$ pulses at a rate of $40Hz$.

Although it had been previously stated that little interaction occurs between the molecules of the bulk material, energy transfer between molecules may take place from one molecular dipole to another via electromagnetic coupling trough the weak intermolecular forces. This is a non-radiative processes, and gives rise to *Förster* [18] energy transfer between molecules within a 5-10nm radius of each other. Förster transfer is a highly efficient energy transfer process, requiring that the emission and absorption spectra of the molecules involved overlap. Förster transfer is commonly used in OSLs to further decrease the degree of re-absorption of emission radiation. In the laser systems of interest in this work, Alq_3 molecules form the bulk of the active material, doped with *4-(Dicyanomethylene)-2-methyl-6-(p-*

10

dimethylaminostyryl)-4H-pyran (DCM) dye in a concentration of about 2%. This combination results in an absorption peak at around 440nm and an emission peak at around 640nm, ensuring that re-absorption is minimised.

Problems with implementing electrically pumped OSLs arise due to induced losses in the material quenching the output. Current thinking suggests that this results from *polaron* absorption [28], which occurs due to the injected charge carriers altering the electronic states of individual molecules. This creates charged molecular species (polarons) which have different atomic transitions available to them than the bulk Alq_3 and are able to absorb the emitted radiation. The exact nature of this process is not well understood however, and the effects may be greatly reduced by the inclusion of thin buffer layers in the laser multi-layer to inhibit their diffusion into the active layer of the laser.

Charge transport and conduction in an amorphous Organic Semiconductor has been likened [29] to that in a crystalline semiconductor containing a large number of traps and defects, resulting in very low carrier mobilities. Such Trap Charge Limited (TCL) conduction in organic semiconductor materials is known to lead to a power law relationship between current and voltage at current densities normally associated with lasing.

In the following analysis, it will be seen how the unusual opto-electronic properties of organic materials effect the design and performance of Organic Semiconductor Lasers.

1.2   Structure of This Thesis

The chapters of this thesis have been arranged in the same order as the work that they represent was performed. Where possible a theory chapter is followed by a chapter documenting results. The work can be divided into three parts:

Analysis and Design of a Fabry-Perot Cavity OSL

This part of the thesis (Chapters 2 and 3) describes an investigation into the lasing threshold of an experimental OSL [16]. In Chapter 2, techniques are presented that are later used in the analysis of the laser modes. Chapter 3 presents the results of the analysis.

Analysis and Design of DFB OSLs

In Chapters 4 and 5, the suitability of Distributed Feed-Back (DFB) gratings for use in the design of Organic Semiconductor Lasers is assessed.

Chapter 4 explains the techniques used to analyse the modes of such a laser. An analysis of a number of possible configurations of a DFB-OSL is performed in Chapter 5 using the techniques previously derived.

Chapter 6 documents a threshold current analysis of the linear (parallel) grating DFB discussed in the previous section and includes details on the analysis method used.

Analysis and Design of CG-DFB OSLs

In Chapter 7, techniques by which the modes of Circular Grating DFB (CG-DFB) lasers may be analysed are presented. Chapter 8 uses these methods to investigate the properties of theoretical CG-DFB OSLs. Both threshold gain, and threshold current analyses are performed.

Chapter 2

Analysis of Multilayer Optical Waveguides

2.1 Introduction

Methods by which the analysis of semiconductor waveguides consisting of a few layers of homogeneous material are well documented [1]. For the subsequent analysis of semiconductor lasers however, techniques must be used that are applicable to channel waveguides composed of many homogeneous regions. To examine the result of stimulated emission on the properties of the waveguide, it is also a requirement that the effects of optical gain are accounted for in the analysis.

In this chapter, techniques suitable for the investigation of channel waveguides in semiconductor lasers are discussed.

2.2 Optical Propagation in a Waveguide

A *planar* or *slab* waveguide is a theoretical structure comprised of several semi-infinite layers of homogeneous material. A typical three layer structure is depicted in Figure 2.1.
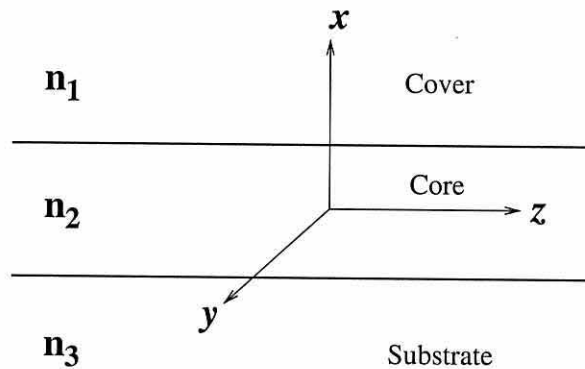
Figure 2.1: *A three layer planar waveguide, with Cartesian axes superimposed*

The waveguide is characterised only by the refractive indices (n_1, n_2 and

n_3) of the layers and the thicknesses of the layers between the *cover* and *substrate*. Assuming a harmonic time dependence for the electromagnetic field (see Appendix A), light propagating in the waveguide must satisfy the time-independent wave equation;

$$\nabla^2 \mathbf{E}(\mathbf{r}) = k_0^2 n_j^2(\mathbf{r}) \mathbf{E}(\mathbf{r}) \tag{2.1}$$

in each of the $j = 1, 2, 3$ layers, where n_j represents the refractive index of the jth layer.

A Cartesian coordinate system is adopted where the transverse plane is taken to be the plane formed by the x and y coordinates and the z direction is chosen as the direction of propagation. The optical field is assumed invariant in the y direction. The z dependence of the wave may be considered to be harmonic and characterised by a propagation constant, β, so that;

$$\mathbf{E}(x, y, z) = \mathbf{E}(x, y) e^{-j\beta z} \tag{2.2}$$

The actual electromagnetic field in the structure is a summation of components having harmonic dependence on the z coordinate. The harmonic components are characterised by a value of β, and are known as the *modes* of the waveguide.

In a planar waveguide having three layers, the spatial dependence of the refractive index is limited to the x coordinate only. By substitution of (2.2) into (2.1) and setting $\partial/\partial y = 0$, wave equations for the homogeneous regions of the waveguide can then be written

16

$$\frac{\partial^2}{\partial x^2}\mathbf{E}(x,y) + (\beta^2 - k_0^2 n_1^2)\mathbf{E}(x,y) = 0 \qquad (2.3)$$

$$\frac{\partial^2}{\partial x^2}\mathbf{E}(x,y) + (\beta^2 - k_0^2 n_2^2)\mathbf{E}(x,y) = 0 \qquad (2.4)$$

$$\frac{\partial^2}{\partial x^2}\mathbf{E}(x,y) + (\beta^2 - k_0^2 n_3^2)\mathbf{E}(x,y) = 0 \qquad (2.5)$$

Solutions to these equations may be sought as values of β that correspond to the allowed field distributions, $\mathbf{E}(x,y)$, in the waveguide.

2.2.1 TE and TM Modes in a Planar Waveguide

In the planar waveguide, Maxwells equations can be written in the following form;

$$\beta E_y = \omega\mu H_x \qquad (2.6)$$

$$\beta E_x + \frac{\partial}{\partial x}E_z = \omega\mu H_y \qquad (2.7)$$

$$\frac{\partial}{\partial x}E_y = -j\omega\mu H_z \qquad (2.8)$$

$$\beta H_y = \omega\epsilon E_x \qquad (2.9)$$

$$j\beta H_x + \frac{\partial}{\partial x}H_z = -j\omega\epsilon E_y \qquad (2.10)$$

$$\frac{\partial}{\partial x}H_y = j\omega\epsilon E_z \qquad (2.11)$$

An inspection of the above equations reveals that there are two separable, self consistent groups of components: *Transverse Electric* or TE modes,

17

consisting of E_y, H_x and H_z, and *Transverse Magnetic* or TM modes having H_y, E_x and E_z components.

The TE solutions require that $E_z = 0$ and the TM require $H_z = 0$. By seeking the TE and TM mode solutions separately, the wave equations for the planar waveguide may be cast in a scalar form, known as the *Helmholtz* equations;

$$\frac{\partial^2}{\partial x^2} E_y(x, y) + (\beta_{TE}^2 - k_0^2 n^2(x)) E_y(x, y) = 0 \qquad (2.12)$$

for the TE modes and

$$\frac{\partial^2}{\partial x^2} H_y(x, y) + (\beta_{TM}^2 - k_0^2 n^2(x)) H_y(x, y) = 0 \qquad (2.13)$$

for the TM modes, where $n(x)$ is the x dependent refractive index. The TE and TM modes are found in a similar manner and initial discussion will be restricted to the case of TE modes.

2.2.2 The Complex Dielectric Constant

The time independent electric field component of a TE mode in a planar waveguide has the form:

$$E_y(x, z) = E_y(x)^{j(k_0 n z)} \qquad (2.14)$$

If the refractive index, n, is complex, the imaginary part of n will represent exponential growth or decay of the wave amplitude in the z direction. It is useful to use complex dielectric constants when analysing active devices, as the optical gain or loss can be incorporated in the imaginary part of the

18

refractive index of the material. Assuming the refractive index to be of the form; $n = n' + jn''$, the imaginary part of the refractive index is related to the field loss coefficient, $\alpha/2$, by the relation

$$n'' = \frac{\alpha}{2k_0} \qquad (2.15)$$

The complex propagation constant, β, is then related to the complex refractive index by; $\beta = k_0(n' + jn'')$.

2.3 Solving The Wave Equation

For the three layer case of Figure 2.1, solutions can be sought by deriving transcendental equations using the continuity of the electric and magnetic fields at the interfaces [1] [2]. The use of explicit transcendental equations is limited, however, to waveguides of just a few layers before the analysis becomes unwieldy. The requirement that a single equation be derived describing the matching of the field and its derivative at each interface makes the entirely analytic approach time consuming and exceptionally tedious as the number of layers increases.

2.3.1 Transfer Matrix Techniques

The use of transfer matrix techniques to analyse multi-layered optical waveguides is used in [4] as a means of reducing the complexity of matching the boundary conditions of the fields at the layer interfaces.

For a multi-layered planar waveguide having only an x dependent refractive index variation, as shown in Figure 2.2, a general solution to TE wave

19
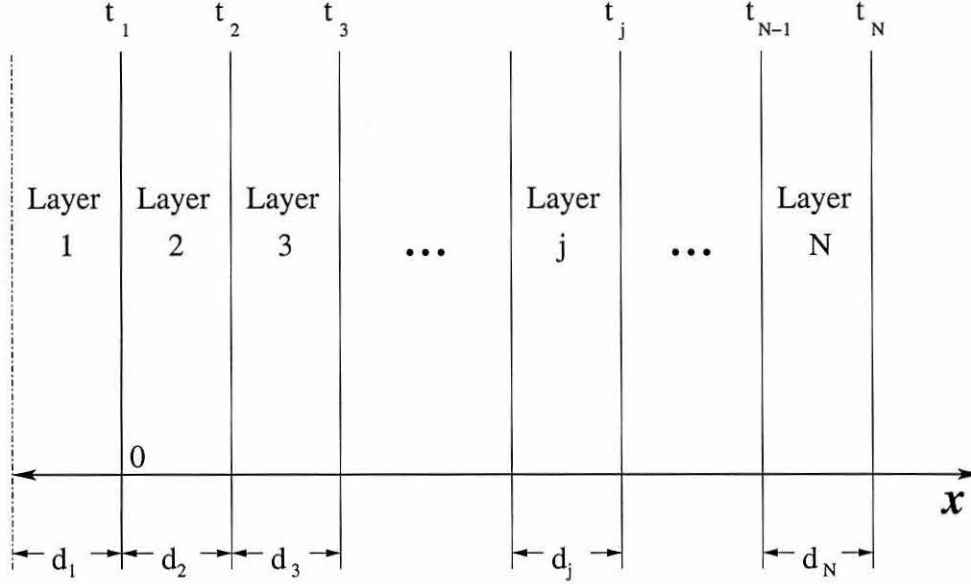
Figure 2.2: *Multilayer Waveguide Structure*

equation (2.12) in the j'th layer may take the form of the wave function;

$$E_j(x) = A_j e^{\alpha_j(x-t_j)} + B_j e^{-\alpha_j(x-t_j)} \tag{2.16}$$

where $\alpha_j = \sqrt{\beta^2 - k_0^2 n_j^2}$ and t_j is the position of the interface of the j'th layer, as seen in Figure 2.2. A_j and B_j are complex constants for each layer.

Using equations (2.6-2.11), the boundary conditions for the continuity of the electromagnetic field at the interfaces can be written as;

$$E_j(t_j) = E_{j+1}(t_j) \tag{2.17}$$

for the E_y field. Using equations (2.6) and (2.8);

$$\frac{\beta}{\omega\mu_j} E_j(t_j) = \frac{\beta}{\omega\mu_{j+1}} E_{j+1}(t_j) \tag{2.18}$$

is obtained for the for the H_x component and;

20

$$\frac{-j}{\omega\mu_j}\frac{\partial}{\partial x}E_j(t_j) = \frac{-j}{\omega\mu_{j+1}}\frac{\partial}{\partial x}E_{j+1}(t_j) \tag{2.19}$$

for the H_z component. With $\mu_j = \mu_{j+1}$, the above expressions reduce to two equations matching the $\varepsilon(x)$ field and its derivative at the j'th interface. Equation (2.16) may then be substituted into the boundary conditions to give;

$$A_j + B_j = A_{j+1}e^{\alpha_{j+1}d_{j+1}} + B_{j+1}e^{-\alpha_{j+1}d_{j+1}} \tag{2.20}$$

$$\alpha_j A_j + \alpha_j B_j = \alpha_{j+1}A_{j+1}e^{\alpha_{j+1}d_{j+1}} + \alpha_{j+1}B_{j+1}e^{-\alpha_{j+1}d_{j+1}} \tag{2.21}$$

where $d_{j+1} = t_j - t_{j+1}$ is the thickness of the next layer. The above equations may be re-arranged into a form relating the A and B coefficients of the current layer to those of the subsequent layer;

$$A_j = A_{j+1}\frac{1}{2}(1 + \frac{\alpha_{j+1}}{\alpha_j})e^{\alpha_{j+1}dj+1} + B_{j+1}\frac{1}{2}(1 - \frac{\alpha_{j+1}}{\alpha_j})e^{-\alpha_{j+1}dj+1} \tag{2.22}$$

$$B_j = A_{j+1}\frac{1}{2}(1 - \frac{\alpha_{j+1}}{\alpha_j})e^{\alpha_{j+1}dj+1} + B_{j+1}\frac{1}{2}(1 + \frac{\alpha_{j+1}}{\alpha_j})e^{-\alpha_{j+1}dj+1} \tag{2.23}$$

which may be written in a matrix form as;

$$\begin{bmatrix} A_j \\ B_j \end{bmatrix} = m_j \begin{bmatrix} A_{j+1} \\ B_{j+1} \end{bmatrix} \tag{2.24}$$

where;

21

$$m_j(\beta) = \begin{bmatrix} \frac{1}{2}(1 + \frac{\alpha_{j+1}}{\alpha_j})e^{\alpha_{j+1}d_{j+1}} & \frac{1}{2}(1 - \frac{\alpha_{j+1}}{\alpha_j})e^{-\alpha_{j+1}d_{j+1}} \\ \frac{1}{2}(1 - \frac{\alpha_{j+1}}{\alpha_j})e^{\alpha_{j+1}d_{j+1}} & \frac{1}{2}(1 + \frac{\alpha_{j+1}}{\alpha_j})e^{-\alpha_{j+1}d_{j+1}} \end{bmatrix} \qquad (2.25)$$

with the α_j's defined as;

$$\alpha_j = \sqrt{\beta^2 - k_0^2 n_j^2} \qquad (2.26)$$

For a multi-layer structure having N homogeneous layers, a transfer matrix for the entire waveguide can be defined as the product, T, of the intermediate m_j layer matrices.:

$$T(\beta) = \prod_{j=1}^{N-1} m_j(\beta) \qquad (2.27)$$

The T matrix thus connects the A and B coefficients of the first and last layers, that is; A_0 to A_N and B_0 to B_N:

$$\begin{bmatrix} A_1 \\ B_1 \end{bmatrix} = T(\beta) \begin{bmatrix} A_N \\ B_N \end{bmatrix} \qquad (2.28)$$

Setting the A or B coefficient in (2.16) to zero in the cover or substrate layer results in a field growing or decaying exponentially away from the centre of the structure, corresponding to leaky or confined modes of the waveguide. In the most common case of confined mode solutions, the field is required to decay exponentially in layers 1 and N, requiring $B_1 = 0$ and $A_N = 0$. In terms of the matrix, $T(\beta)$

$$\begin{bmatrix} A_1 \\ 0 \end{bmatrix} = \begin{bmatrix} T_{11}(\beta) & T_{12}(\beta) \\ T_{21}(\beta) & T_{22}(\beta) \end{bmatrix} \begin{bmatrix} 0 \\ B_N \end{bmatrix} \qquad (2.29)$$

Multiplying out the matrices reveals that equation (2.29) is only satisfied when $T_{22} = 0$. The expression $T_{22}(\beta) = 0$ therefore has solutions in terms of discrete values for β that represent the confined modes of the waveguide. $T_{22}(\beta) = 0$ is therefore the *dispersion relation* of the multi-layer structure.

Modes which are exponentially increasing away from the centre of the wave-guide (so-called *lossy* or *anti-guiding* modes) may be located by selection of a different element of the T matrix. By selecting $A_1 = 0$ and $B_N = 0$ in 2.29, corresponding to having exponentially growing fields in the cover and substrate, it can be proven that a suitable dispersion relation for anti-guiding modes would be $T_{11} = 0$.

The derivation of the TM mode dispersion relation is similar to that of the TE case. In practical terms, the only difference is seen in the individual elements of the m_j layer matrix. The dispersion relation for TM modes is derived in Appendix B.

2.3.2 The Dispersion Relation Described using Riemann Constructs

For a waveguide having complex refractive indices, and therefore complex propagation constants, the computation of the α_j coefficients for the m_j layer matrices involves the evaluation of a complex square root function. The implications of the complex square roots in the evaluation of the dispersion relation will now be discussed.

It is well known that the square root of a real number is bi-valued. Although both solutions are valid the choice of solution to a square root func-

tion is often a matter of whether one requires continuity of the function at its singular point, the origin. Many computer implementations of the square root function use a simple rule whereby the solution is always taken to be positive. Although for most cases this assumption is adequate, it does mean that the function is only piecewise-continuous about the origin (the solid line in Figure 2.3).
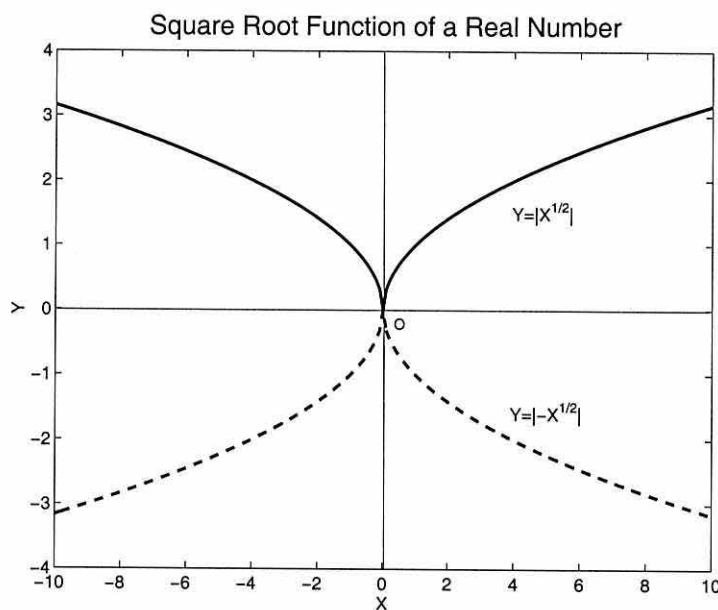
Figure 2.3: *Square root of a real number.*

Mathematically, this is hard to justify, the exponential function, x^n, is continuous for $n > 1$, so the function $x^{1/2}$ must also be continuous. For proper implementation of the square root function on a computer, the sign of the result should be manually inverted every time the origin is crossed.

An expression such as $y = f(\mathbf{z})$, where $f(\mathbf{z})$ is the *complex function* may be visualised as a *Riemann surface* on the complex plane. The features of the surface are then a result of the variation in amplitude of the dependent variable, y, with real and imaginary parts of $\mathbf{z}$. For the complex square root

24

$y = \sqrt{\mathbf{z}}$, y will reside simultaneously on two surfaces, corresponding to the positive and negative roots of the previous example (Figure 2.4).
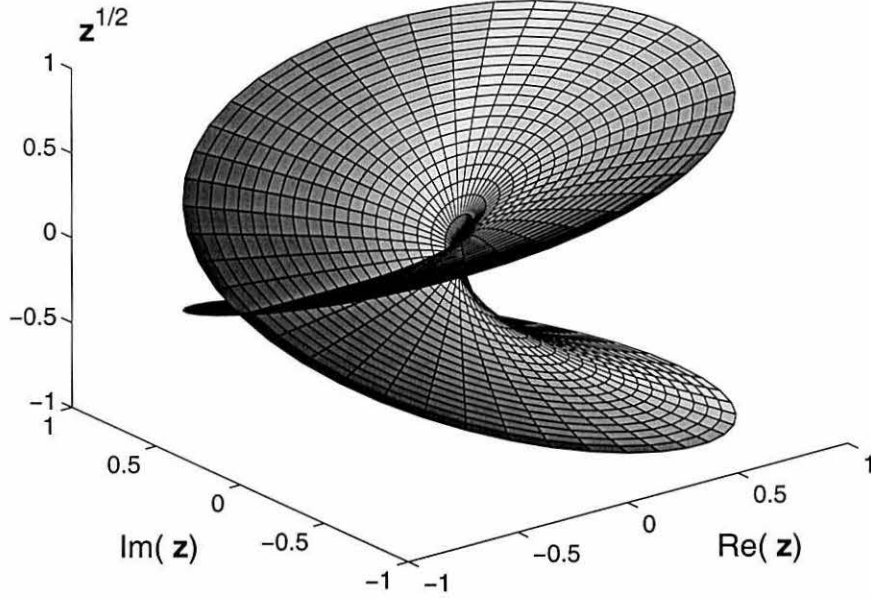
Figure 2.4: *Riemann surface for the complex square root function.*

As seen in Figure 2.4, for the complex square root, the discontinuity arises not only at the origin, but also along the line section formed along the negative real axis. It is also important to note that, if continuity of the function is maintained, any contour encircling the origin must make two revolutions in order to close. A *Riemann surface* is shown for the complex square root function in Figure (2.4).

By inspection of the layer matrices (2.25) of which the dispersion function is composed, it can be seen that, with complex refractive indices assumed, the waveguide matrix, T, contains complex square roots in its four elements. The complex roots in the individual m_j layer matrices make α_j bi-valued for

25

all values of β except at the singular point $\beta^2 = k_o \mathbf{n}_j^2$.

The way in which the multi-valued nature of the α_j coefficients affects the multi-layer waveguide dispersion relation is addressed in [5], where it was noted that during multiplication of the layer matrices, the intermediate α_j singular points are removable in the solution space of the elements of the dispersion matrix, T, leaving only the singular points of α_1 and α_N to characterise the function. The elements of T are found to be four-valued as a result of the combination of the two complex square root functions α_1 and α_N.

It was shown in [5] how the nature of the solutions changes depending on which surface they occupy, and their position in relation to the two singular points. The four valued dispersion function results from the ambiguity of the sign of two complex square root functions in α_1 and α_N appearing in the argument and magnitude of the exponentials forming the T matrix elements. However a multiplication of several of the m_j matrices demonstrates that the T matrix elements only differ from one another in terms of the signs of their arguments and magnitudes, in a similar manner to the m_j matrix elements. It is therefore apparent that any element of T may be chosen as the dispersion relation and may be used to find solutions of a bound or lossy nature. Selecting a different element of T as the dispersion relation therefore merely changes which region of the four sheeted Riemann surface contains the required solutions. For example, by selecting the dispersion relation as T_{22}, the bound mode solutions lie near the line segment extending in a positive direction parallel with the real axis from the singular point $\alpha_N = 0$. Using the T_{11} element as the dispersion relation places the bound solutions on the

line segment between the two singular points, $\alpha_1 = 0$ and $\alpha_N = 0$

2.3.3 Unfolding The Multi-valued Dispersion Relation

In order to locate the zeros of the dispersion relation more easily, it is possible to map the multi-valued dispersion relation onto a single complex plane. This is achieved by employing a variable substitution to ensuring that the complex square root functions are removed. The elements of the T matrix for the waveguide are four-valued by virtue of the complex square roots in α_1 and α_N. By selecting V to be the new independent variable, making the substitution;

$$V = \alpha_1 = \sqrt{\beta^2 - k_0^2 n_1^2} \tag{2.30}$$

The elements of T are now just two-valued by virtue of the complex square root in α_N. The substitution, known as a *conformal mapping*, unfolds the four valued function in β onto a bi-valued solution space, V. In a similar manner, the technique described in [6] unfolds the four valued solution space onto a single plane by means of the conformal mapping substitution;

$$U = \sqrt{\beta^2 - k_0^2 n_1^2} + \sqrt{\beta^2 - k_0^2 n_N^2} \tag{2.31}$$

where U is the new independent variable after the unfolding. This mapping projects the multi-valued dispersion relation onto a single complex plane of the variable U. Using this approach, solutions can be more conveniently observed as they move across the chosen region of interest. Unfolding the dispersion function also greatly simplifies any root-finding algorithms by re-

moving the need to impose branch cuts on the complex root functions. The various regions of the four-sheeted dispersion relation yielding different types of solutions are mapped onto the unfolded, U, plane as shown in Figure (2.5) after [6]. It can be seen from the figure that the origin of the unfolded dispersion function corresponds to the singular point $\beta^2 = k_0^2 n_0^2$. Solutions that are lossy or bound in both the cover and substrate are found outside a circular region enclosing the origin, having a radius defined by the singular point $\beta^2 = k_0^2 n_N^2$. Therefore when $n_0 = n_N$, and the waveguide is symmetric, only symmetric solutions will exist. The region of interest for bound modes lies close to $\beta^2 = k_0^2 n_N^2$ and is indicated by a dotted line on the figure.
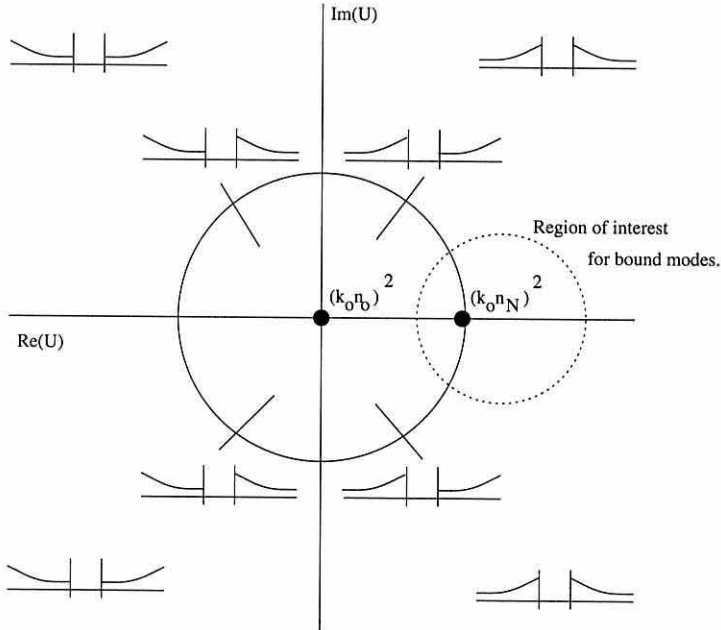
Figure 2.5: *Conformal mapping of the dispersion relation onto a single plain, The forms of the fields found as solutions to the dispersion relation in each region are shown.*

2.3.4 Discussion

In the preceding analysis, it has been demonstrated how the transfer matrix method may be applied to the analysis of a multi-layered planar waveguide structure to yield a single transfer matrix, the elements of which have zeros representing the bound or *guided* mode solutions of the waveguide. The *dispersion relation* of the waveguide is obtained from the elements of the transfer matrix, T, and has been shown to be four-valued in the solution space representing values of the complex propagation constant, β. A method of unfolding the dispersion relation using a conformal mapping variable substitution may then be employed to avoid the problems associated with maintaining the continuity of the function over its branch points. The problem of finding the modes of a multi-layer waveguide with complex refractive indices has therefore been reduced to that of locating the zeros of a complex function in the unfolding variable, U.

2.4 The Effective Index Method (EIM)

The effective index method is a technique allowing the analysis of two dimensional *channel* or *rib* waveguides where the refractive index has variation in both x and y transverse coordinates. The EIM method makes a number of approximations concerning the form of the optical field but is known to be reasonably accurate for a wide range of structures.

29

2.4.1 Plane Wave Approximation of a Channel Waveguide

The first assumption of the EIM is that the optical field is a combination of two orthogonal planar waveguide modes, as shown in figure(2.6);
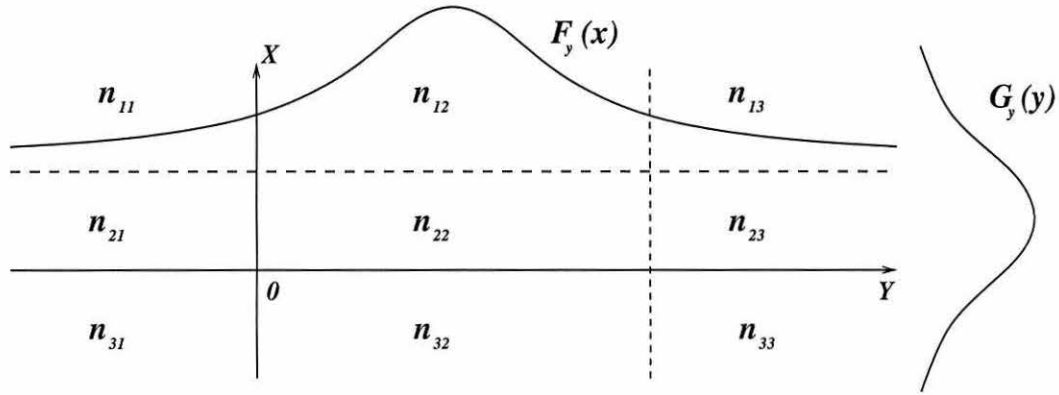
Figure 2.6: *Two dimensional waveguide cross section.*

$$E_y(x, y) = F_y(x)G_y(y) \qquad (2.32)$$

Substitution of (2.32) into (2.12) gives;

$$\left(\frac{\partial^2}{\partial x^2} + \frac{\partial^2}{\partial y^2}\right)F_y(x)G_y(y) + (\beta_{xy}^2 - k_0^2 n(x, y)^2)F_y(x)G_y(y) = 0 \qquad (2.33)$$

The wave equation may be separated into two planar wave equations provided that the refractive index and propagation constant may be decomposed into a combination of x and y dependent components:

$$n(x, y)^2 = n(x)^2 + n(y)^2 \qquad (2.34)$$

$$\beta_{xy}^2 = \beta_x^2 + \beta_y^2 \qquad (2.35)$$

30

The approximation is made that the refractive index of the waveguide components varying only in the y direction, $n(y)$, are *effective indices* derived from the analysis of the orthogonal planar waveguide, having a refractive index $n(x)$.

$$n(y) \approx \frac{\beta_x^2}{k_0^2} \tag{2.36}$$

Where β_x^2 has been found previously as a solution to

$$\frac{\partial^2}{\partial x^2} F_y(x) + (\beta_x^2 - k_0^2 n(x)^2) F_y(x) = 0 \tag{2.37}$$

and $n(x)^2$ is taken to be the actual refractive index variation of the n_{12}, n_{22}, n_{32}waveguide with x. Substituting (2.36) into (2.33) then yields

$$(\frac{\partial^2}{\partial x^2} + \frac{\partial^2}{\partial y^2}) F_y(x) G_y(y) + (\beta_y^2 - k_0^2 n(x)^2) F_y(x) G_y(y) = 0 \tag{2.38}$$

Comparison of (2.38) with (2.33) reveals that $\beta_y^2 \approx \beta_{xy}^2$ with the effective index assumption of (2.36) made. It is also an implication from equation (2.38) that $n(x,y) \approx n(x)$. This suggests that the effective index approximation is more accurate when variation of the refractive index in the y direction is negligible compared to index variation in the x direction. For this reason it is advantageous to choose the order of the calculation in such a way as to ensure that the planar waveguide component having the most variation in refractive index is solved first, before the assumption of (2.36) is made.

If $F_y(x)$ and $G_y(y)$ are mode solutions to the corresponding orthogonal planar waveguides (a) and (b) in Figure (2.7), then for modes having the

31

electric field component in the y direction, $F_y(x)$ is the electric field component of the TE solution to the planar waveguide (b) characterised by $\frac{\partial}{\partial y} = 0$, and $G_y(y)$ must be the electric field component of the TM solution to the planar waveguide (a) where $\frac{\partial}{\partial x} = 0$. The solutions for this combination are normally denoted E_{nm}^{y} modes, where n and m are the mode orders of the x and y dependent waveguide solutions respectively. Similarly E_{nm}^{x} modes may be approximated by a combination of TM modes to the x dependent waveguide component and TE solutions to the y dependent waveguide.

Of particular interest here is the analysis of *rib* or *channel* waveguides. An example is shown in Figure (2.6). The waveguide can be separated into three regions in the y coordinate, labelled I, II and III. For each region there can be defined a planar structure having a refractive index variation only in the x direction. Typically, the width of the active region in the y (lateral) direction is much larger than its width in the x (transverse) direction.
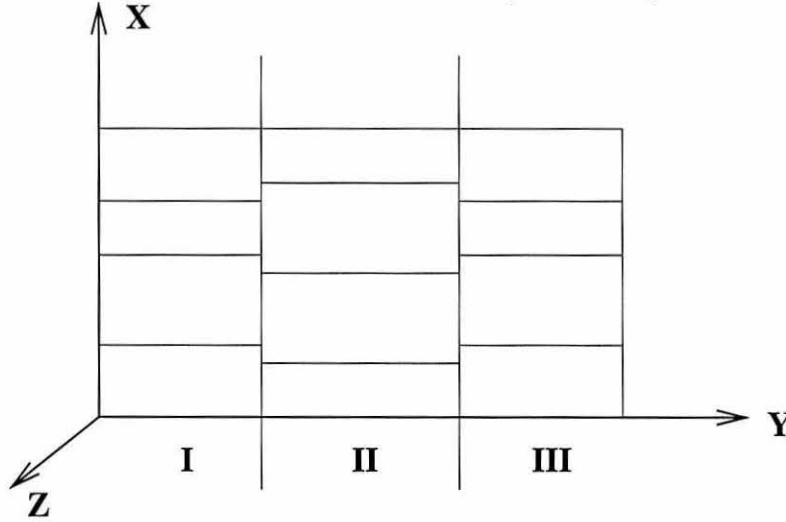
Figure 2.7: *Example of a multilayer channel waveguide.*

To obtain the E_y^{nm} modes of this structure, the TE solutions to the three

x dependent waveguides in regions I, II and III are sought. This provides three values of effective index $n_{eff,I,x}$, $n_{eff,II,x}$ and $n_{eff,III,x}$ via the approximation of (2.36). The number of modes found in the centre region (II), is taken as the integer n in E_y^{nm}. Locating the TM modes of the three layer waveguide formed by $n_{eff,I,x}$, $n_{eff,II,x}$ and $n_{eff,III,x}$ then yields the propagation constants of the waveguide. The number of TM solutions found is taken to be m in E_y^{nm}.

The E^x modes may be similarly located by substituting the TM solution for the x dependent waveguide and a TE solution for the y dependent component.

2.4.2 Accuracy of the EIM

It is known [8]-[12] that the effective index approximation can overestimate the propagation constant for the lateral waveguide by a considerable amount. Various improvements have been suggested to improve the accuracy of this technique [13][14]. Alternative techniques, such as the spectral index method [15] can be used if more accurate results are required. These alternative methods may be of particular interest in structures where the lateral mode is near cut-off, which is known to be the region of highest error in effective index calculations. Rib waveguides having an exceptionally high index step are also prone to error because of the effect of the corners of the rib on the field profile.

The effective index method is most accurate when analysing structures having comparatively small variations in refractive index. The maximum

refractive index variation in a semiconductor laser is usually found at the air interface. A typical index step at the air interface of an organic laser is $\Delta n \approx 1$, whereas for an in-organic material like InGaAs, $\Delta n > 2$ is typical. The basic EIM method should therefore provide results to a greater accuracy in the analysis of organic laser waveguides than in-organic structures.

2.5 Determining Solutions of the Dispersion Relation

There are many ways of efficiently finding the zeros of a complex function and the selection of a suitable technique is highly dependent upon the nature of the problem. To locate the solutions of the unfolded dispersion relation, it is more convenient to use an algorithm that operates within a fixed region of interest on the complex plane, rather than requiring an initial estimate of the propagation constant. For the analysis of the waveguide modes in a semiconductor laser, it is also an advantage if all the solutions within that region of interest are sought simultaneously rather than consecutively, so that the modes can be seen to move across the solution space as changes in the device geometry are made. The Argument Principle Method (APM) was first suggested in [3] and fulfils all of these criteria whilst offering reasonable execution times and required accuracy on a desktop PC.

2.5.1 The Argument Principle Method (APM)

The Argument Principle Method [3], is based on the argument principle theorem in complex analysis. The argument principle theorem states that, for any closed curve, C on a complex plane, z;

$$\frac{1}{2\pi i} \oint_c \frac{f'(z)}{f(z)} dz = n \tag{2.39}$$

where n is the number of zeros of $f(z)$ within the contour, C, and $f'(z)$ is the derivative of the function.

It is possible to obtain a summation of the values of the complex variable at the zeros of the function by evaluating;

$$S_m = \frac{1}{2\pi i} \oint_c z^m \frac{f'(z)}{f(z)} dz = \sum_{i=1}^{n} Z_i^m \tag{2.40}$$

where Z_i are the $i = 1, 2, ..., n$ zeros of $f(z)$ inside C. From (2.39) the integral in (2.40) returns the number of zeros, n, within C when $m = 0$. The summations given by (2.40) for $m = 1, ..., n$, can then be used to evaluate the coefficients of a polynomial $p(z)$, having the same roots, $Z_1, ..., Z_n$ as the function $f(z)$.

$$p(z) = C_1 z^1 + C_2 z^2 + C_3 z^3 + ... + C_n z^n \tag{2.41}$$

After [5], the coefficients $C_1, ..., C_n$ are then found using the recurrence relation:

$$C_k = \frac{1}{(k-n)} \sum_{j=0}^{k} S_j C_{k+j} \tag{2.42}$$

By setting $C_n = 1$, all of the coefficients of (2.41) can be found by recursive

35

application of (2.42). The roots of the polynomial can then be located using any well known root finding algorithm, such as Laguerres method.

2.5.2 Application of the APM

The APM may be applied to locating the zeros of the dispersion relation within a particular region of the unfolded complex plane, U. Where the contour integral used in the calculation becomes;

$$S_m = \frac{1}{2\pi i} \oint_c U^m \frac{T'_{11}(U)}{T_{11}(U)} dU \qquad (2.43)$$

where U is the unfolded complex variable given by (2.31) and the derivative of the dispersion function, $T'_{11}(U)$, is obtained by a simple application of the chain rule to the individual m_j layer matrices.

In a waveguide, the contour for the integral may be selected so as to enclose a region within which the confined mode solutions are to be found. Using the matrix element $T_{11}(U)$ as the dispersion relation, the confined modes reside near the line segment between $\beta = k_0 n_N$ ($U = \sqrt{k_0^2 n_N^2 - k_0^2 n_1^2}$) and $\beta = k_0 n_{max}$ (where n_{max} is the highest refractive index in the structure) as seen in Figure (2.5).

2.6 Summary

It has been shown how the *Transfer Matrix Method* (TMM), the *Argument Principle Method* (APM) and the *Effective Index Method* (EIM) may be used to find solutions to the Helmholtz wave equation for a two dimensional optical field in a channel waveguide having material gain or absorption. In

the following section, these methods will be applied to a prototype Organic Semiconductor Laser structure.

Chapter 3

Investigation of an Organic Semiconductor Laser (OSL)

3.1 A Prototype OSL

In the preceding chapter, it was shown how various analytic and semi-analytic techniques may be combined to extract the optical modes of planar and channel waveguides. In the following, a prototype OSL is analysed using these methods. The optical modes supported by the OSL are found, leading to an analysis of the material gain required to operate the laser under optical pumping (the *threshold gain*). Variations in the device geometry are considered with a view to reducing the threshold gain.

3.1.1 Structure

Attention is given to the organic semiconductor laser structure described in [16]. The laser is an optically pumped device with an operating wavelength of around 630nm.

The OSL in [16] is constructed from a *tris-(8-hydroxyquinoline) aluminium* (Alq_3) multilayer that has been vapour deposited onto an SiO_2 cladding. The laser is of the double heterostructure[1] (DH) type and has parallel reflective facets at either end forming a Fabry-Perot resonant cavity. The facets are formed by the deposited layers of organic material conforming to the shape of the underlying InP substrate, which is cleaved prior to vapour deposition of the Alq_3. The structure of the laser waveguide is shown in Figure 3.1.

In this example structure, a 2μm layer of SiO_2 is used for the cladding which acts as a buffer between the confining layers and the substrate. Light

---

[1]DH lasers are characterised by having separate homogeneous layers above and below the active region, typically to assist in charge transport
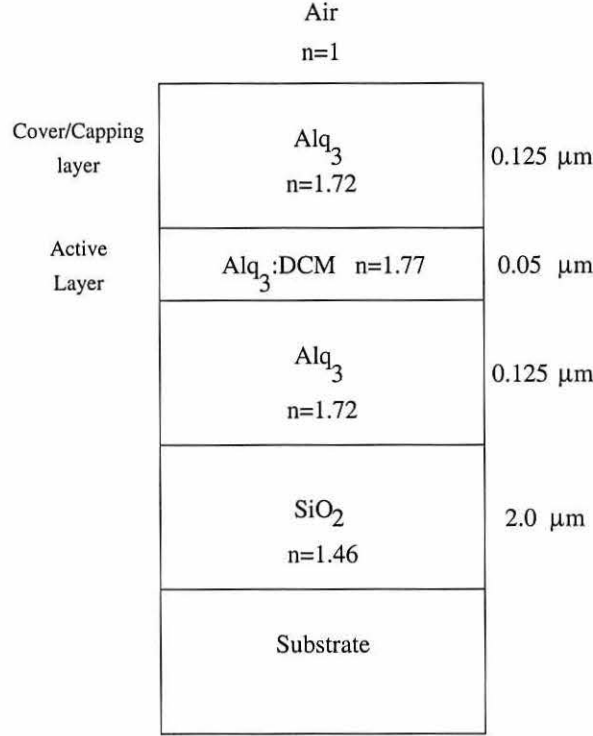
Figure 3.1: *Structure of the laser waveguide; the transverse composition of the OSL is shown with associated refractive indices for the layers*

is confined to a 0.3μm thick film of Alq$_3$, with the middle 0.05μm being doped with *4-(Dicyanomethylene)-2-methyl-6-(p-dimethylaminostyryl)-4H-pyran* (DCM) dye to act as the active region. Initial measurements described in [16] reported the end facets to have a reflectivity of approximately 7%.

In [16], the laser waveguide is optically pumped using a 337nm nitrogen laser focussed, using a cylindrical lens, onto a 50μm wide stripe perpendicular to the plane of the facets. A schematic diagram showing the structure of the laser cavity is shown in Figure 3.2. In [16] The operating wavelength of the laser was reported to be 632nm, with a gain threshold of around 1μJ/cm^2.

The laser was also seen to support a single transverse mode.

Transverse single mode or *monomode* operation is desirable in lasers designed for a wide variety of applications where narrow band emission and small spot size may be required.
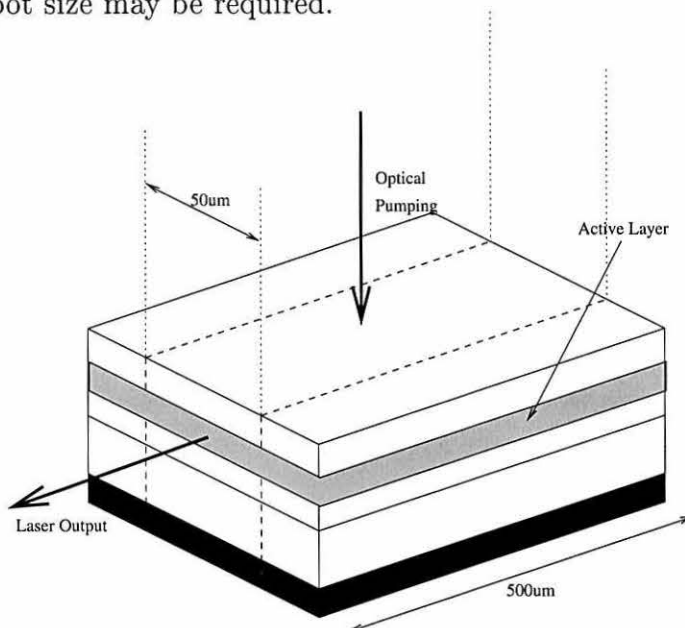
Figure 3.2: *Structure of the laser cavity*

3.1.2   Modal Gain

The gain threshold in a laser is defined as the level of gain required to overcome the total optical losses in the structure. The *modal gain* threshold of the OSL can be estimated using the standard expression for the losses in a Fabry-Perot cavity, derived by a consideration of the repeated reflection of the electro-magnetic waves at the end reflectors [1],[2]:

$$\gamma = \frac{1}{L} \ln \frac{1}{R} + \alpha \tag{3.1}$$

41

where L is the length of the cavity, R is the reflectivity of the end mirrors and α represents internal losses due to absorption and scattering in the bulk material. γ may be considered to approximate the gain required to overcome material losses in the cavity and the partial transmission of light at the end facets. The name *modal gain* refers to the fact that γ is the gain of a particular transverse mode supported by the laser waveguide.

As well as losses at the reflectors, the other main cause of loss arises from imperfect confinement of the light as it propagates along the waveguide. Account may be taken of this by means of a confinement factor, Γ, obtained numerically from the transverse mode field profile as:

$$\Gamma = \frac{\int_A |e(x,y)|^2 dxdy}{\int_\infty |e(x,y)|^2 dxdy} \tag{3.2}$$

Where A is the active region area and $e(x,y)$ is the transverse field profile. A confinement factor, Γ, of unity thus implies a well confined mode in the transverse direction, and may be a reasonable approximation for lower order modes far from cut-off in a multi-mode structure. The material gain required to overcome the total cavity losses in the structure, g_{th}, is thus given by:

$$g_{th} = \frac{\gamma}{\Gamma} \tag{3.3}$$

In [2] the total loss (and therefore total threshold gain) in a laser cavity is defined as a sum of the modal, scattering and re-absorption losses in the laser waveguide. In the Alq$_3$:DCM material used in the OSL of reference [16] however, the large upward shift in wavelength between the peaks of the absorption and emission spectra ($\approx 300nm$) ensures that the wavelength of

42

the emission radiation is beyond the maximum absorption wavelength for the Alq$_3$ host material and so re-absorption of radiation in the laser is negligible. Scattering losses at the interfaces between the thin films are usually small in comparison to modal losses, and are disregarded in this analysis.

3.1.3 Gain Guiding

In the prototype OSL, optical confinement to the pump stripe is provided by *gain guiding*, in which the presence of optical gain over the pump stripe width gives rise to a weak confinement of the light due to the greater extinction of the electromagnetic field in the surrounding material.

Although in an in-organic semiconductor both the real and imaginary parts of the refractive index are affected by the presence of gain, the variation in the real part can be less than 1% and in most cases be assumed to be zero as it does not affect the waveguiding of the laser significantly. This assumption is especially valid for organic, optically pumped lasers, where changes in refractive index due to optical pumping have yet to be observed in experiment.

To design a laser to operate at gain levels just above threshold, the minimum gain over the active stripe is made equal to the threshold gain of the fundamental mode. However, as the threshold gain is dependent upon the confinement of the gain-guided laser, minimum values for the threshold gain must be sought by successive approximation.

This is achieved by initially setting the confinement of the gain guiding waveguide to unity. The material gain of the laser is then found using (3.1)

and (3.3) with the reflectivity of the end facets of the laser calculated as 0.07 using the expression:

$$R = (\frac{n_a - 1}{1 + n_a})^2 \qquad (3.4)$$

Where $n_a = 1.72$ is the refractive index of the Alq$_3$:DCM material. Substituting this value into equation (3.1) for a laser of length $500\mu m$, results in a gain value of $g = 53\text{cm}^{-1}$ and a value for the imaginary refractive index of $Im(n)=2.7\text{x}10^{-4}$ using the relation:

$$Im(n) = \frac{g}{2k_0} \qquad (3.5)$$

The fundamental modes of the waveguide are then sought to give a confinement factor for the waveguide. A more accurate value of threshold gain for the laser is then calculated using (3.3). This procedure may be repeated until the confinement factors of subsequent calculations are identical, whereupon the threshold gain calculated from (3.3) is at a minimum.

3.1.4 Calculated Modes of the Prototype OSL

Figure 3.3 shows the transverse structure used for the modal investigation. Consideration is given to $E_n^x(x, y)$ modes having the electric component in the x direction. Similarly, modes having the electric field component in the lateral, y, plane will be denoted $E_n^y(x, y)$.

The E^x or *quasi-TE* fundamental modes normally have higher values of confinement than the E^y modes. As the maximum levels of confinement possible are being sought, further discussion will focus on the $E_n^x(x, y)$ solutions.

44

X

n=1	n=1	n=1
n=1.72	n=1.72	n=1.72
n=1.77	n=1.77+j n	n=1.77
n=1.72	n=1.72	n=1.72
n=1.46	n=1.46	n=1.46

50um

Y

n_{eff_x}(cladding) n_{eff_x}(core) n_{eff_x}(cladding)
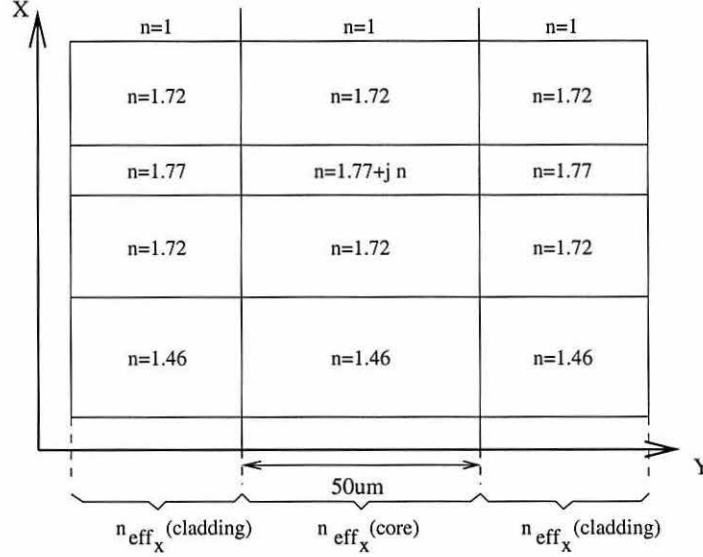
Figure 3.3: *Transverse structure of the channel OSL waveguide*

In the Effective Index Method (EIM), described previously, the two dimensional field is separated into one dimensional x and y dependent components. The quasi-TE modes are therefore decomposed into orthoganol components $E_0^x(x)$ and $E_0^x(y)$.

Using the *effective index method (EIM)* and the *Argument Principal Method (APM)*, the $E_0^x(x)$ modes for the OSL in [16] are calculated for a wavelength of 632nm as: $n_{eff_x}(cladding) = 1.6083$; $n_{eff_x}(core) = 1.6083 + j5.33 \times 10^{-5}$

The effective index for the fundamental lateral mode is found to be, $E_0^x(y)$: $n_{eff_y} = 1.6083 + j5.04 \times 10^{-5}$. Both the transverse and lateral fundamental modes are depicted in Figure (3.4). Although no higher order modes are supported for the x component of the waveguide, modes of beyond the tenth order are supported by the y dependent waveguide at a wavelength of 632nm. In general, higher order modes are less well confined than the fundamental. In this analysis, where the minimum threshold gain of the laser is sought,

45
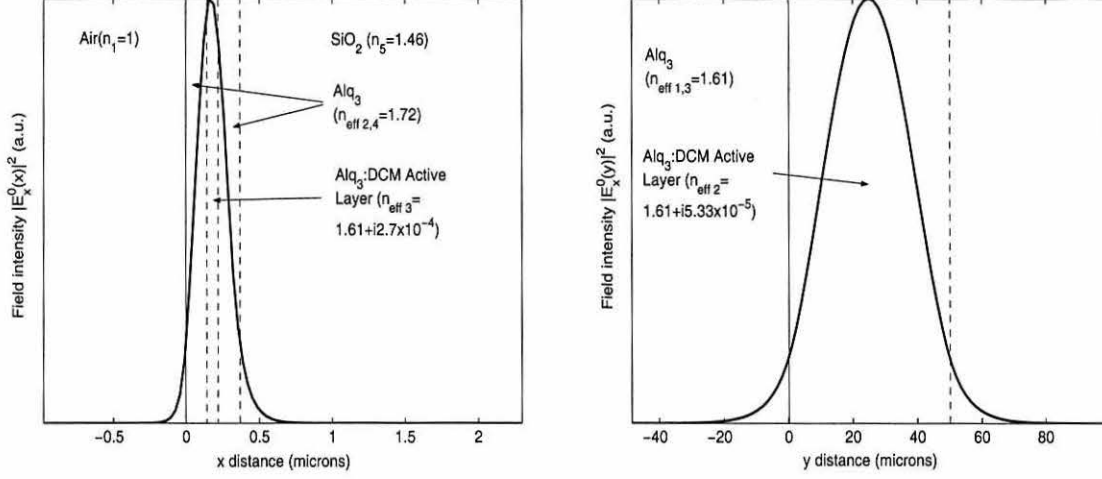
Figure 3.4: x and y dependent components of $E_x^0(x,y)$ mode.

attention is given to the fundamental mode of the y dependent waveguide, as it provides the lowest threshold gain.

3.1.5 Optical Confinement in the Transverse Direction

The confinement factors of the transverse $E_x^0(x)$ and $E_x^0(y)$ modes shown in Figure (3.4) are evaluated from the obtained field profiles as $\Gamma_0^x = 0.2$ and $\Gamma_0^y = 0.95$ respectively. The much lower confinement of the transverse mode is due to the thin (0.05μm) active layer thickness used. The confinement factor of the fundamental mode is found to be $\Gamma_{00}^{xy} \approx 0.2$. Substituting this value for confinement into (3.1) gives a revised value for the threshold gain of $g = 265$cm^{-1}, higher than the initial value. Optical confinement in the transverse, x direction is due to variation in the real refractive indices of the layers of the heterostructure, and is essentially independent of the optical gain. Also, as the lateral waveguide is multi-moded and the fundamental mode is far

46

from cutoff, changing the threshold gain does not alter the confinement of the lateral waveguide fundamental mode by a significant amount.

3.2   Optimising The Waveguide Geometry

The preceding investigation illustrates the lower transverse confinement of the fundamental mode of the OSL structure compared with confinement of the fundamental mode of the gain-guided lateral structure. In order to minimise gain threshold it is of interest to increase, as much as possible, the confinement in the transverse and lateral coordinates. It is also desirable that single mode operation in the transverse direction is maintained, and it is known that higher order transverse modes will be supported by a waveguide having a greater confinement layer width. It is therefore of interest to increase the thickness of the active (confinement) layer whilst avoiding the cut-in of higher order transverse modes. It is recognised, however, that practical problems such as imperfections in the growth of the ALq_3:DCM film may limit the thickness of the active layer.

3.2.1   Varying the Active Layer Thickness

Transverse confinement can be improved by simply increasing the thickness of the active layer. Fig. 3.5 shows a graph of optical confinement versus active layer thickness for the fundamental $E_0^x(x)$ mode of the OSL. It can be seen from Figure 3.5 that the thickness of the active layer can be increased to 0.17μm whilst maintaining single mode operation. This increases the confinement to around 0.5. Calculations show that such a change in thickness

47
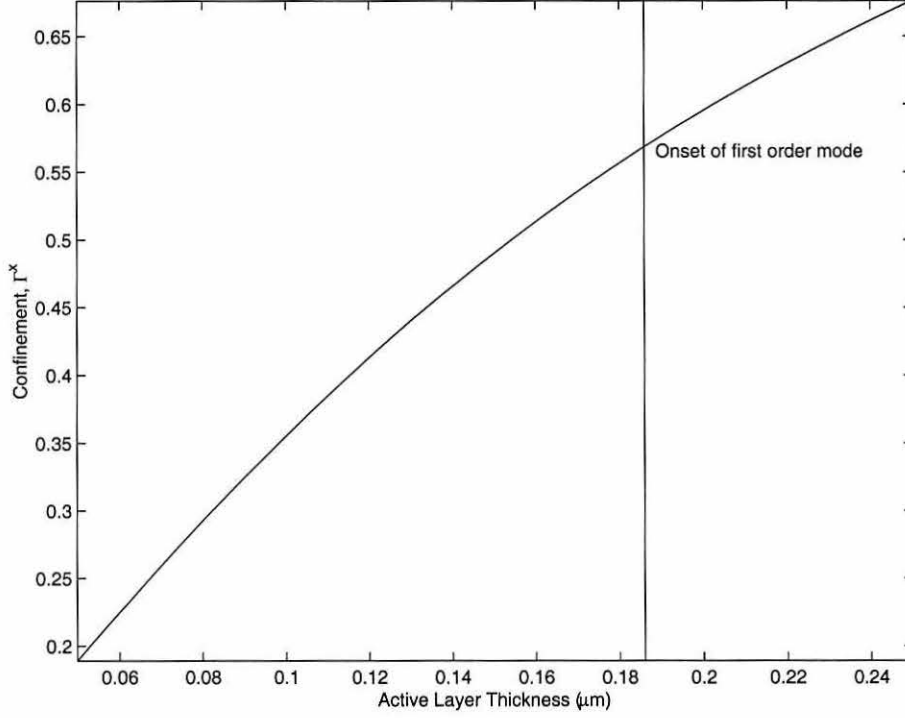
Figure 3.5: *Effect of varying active layer thickness on confinement for a laser having (a)7% and (b) 90% reflectors.*

would give the following modal characteristics: $n_{eff_x}(cladding) = 1.6678$; $n_{eff_x}(core) = 1.6678 + j1.534\text{x}10^{-4}$; $\Gamma_0^x = 0.54$, resulting in an effective index for the fundamental lateral mode of: $n_{eff_y} = 1.6678 + j1.513\text{x}10^{-5}$.

Higher order bound modes also exist for the lateral waveguide given in this configuration. Confinement of the fundamental mode is calculated as: $\Gamma_0^y = 0.99$.

The overall confinement for the fundamental mode of the waveguide is therefore $\Gamma^{xy} = 0.54$ which, used in (3.1), gives a value for the threshold gain of $g = 98\text{cm}^{-1}$, a significant decrease from the initially estimated value of 265cm^{-1}.

48

3.2.2 Varying the Pump Stripe Width

Lateral optical confinement in the OSL is provided by gain-guiding arising from the optically pumping of the laser. It has been shown in the previous section that lateral wave-guide operation is highly multi-mode and confinement of the fundamental approaches unity. The high confinement of a multimode waveguide is of benefit to the efficiency of the laser and minimises the threshold gain. However, it is of interest to re-design the laser for single mode operation in the lateral direction whilst maintaining as high a confinement as possible.

For various values of gain, it was found that first order mode cut-in occurred when lateral confinement of the fundamental exceeded about 0.7. Choosing a minimum value for the lateral confinement of 0.6, the gain threshold of the laser is, from (3.1): $g = 164 \text{cm}^{-1}$.

The confinement curve for the fundamental lateral mode at this level of gain is shown in Figure 3.6. From the figure, it can be seen that a pump beam width of about $6\mu m$ would be required for a single mode operation with a confinement of 0.6.

Reducing the gain will reduce the imaginary effective index of the active stripe, and hence the confinement of the fundamental will be optimum at broader pump widths. This is desirable because optical pump beam widths of below a few tens of microns are physically difficult to achieve.

The threshold gain can be lowered by increasing the reflectivity of the mirrors defining the laser cavity. High reflectivity is obtainable by the use of distributed Bragg reflectors (DBR), which may exhibit reflectivities in excess
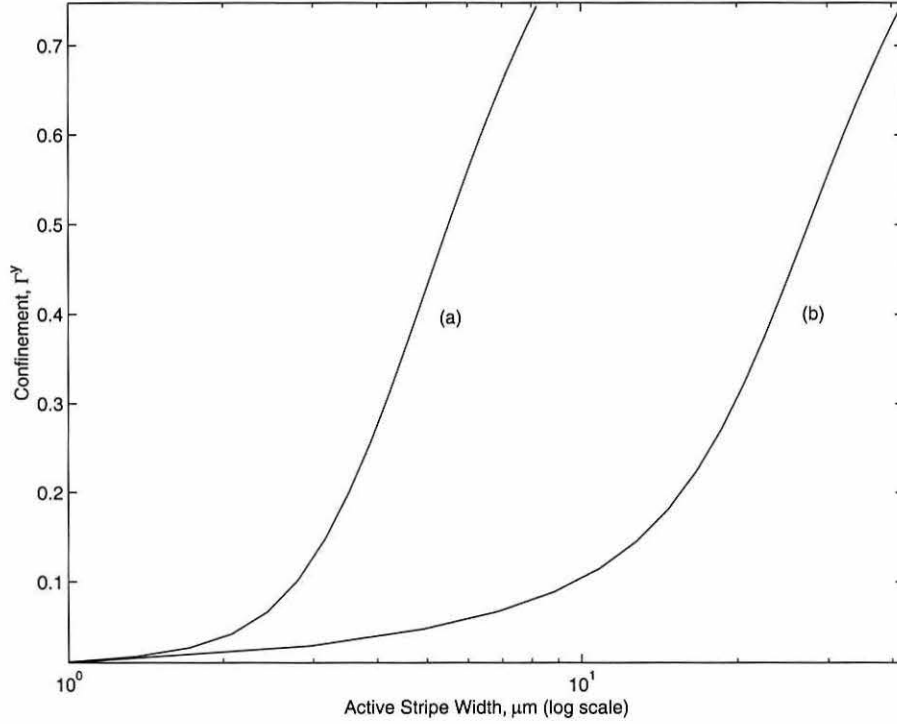
Figure 3.6: *Effect of varying active stripe width on confinement*

of 90%.

Recent reports show favourable results from DBR lasers with both Alq [17] and conjugated polymer [22] gain media. Using a typical value of 90% for the reflectivity, R, in (3.1) gives a threshold gain value of 4cm^{-1} for the OSL with an assumed minimum confinement factor of 0.6. The effect on confinement of this much lower gain threshold can be seen in Figure 3.6(b). The active stripe width at which the optical confinement reaches 0.6 is shown to be around $40\mu m$.

It is recognised that the lateral optical pump profile across the active region will not give rise to an abrupt step in the gain (and hence the imaginary part of the refractive index). It is likely that the intensity of the pump beam

will follow some profile having a maxima along the centre of the active stripe. If the profile of the pump intensity is known, the accuracy of the analysis may be improved slightly by adopting a multi-layer structure for the lateral waveguide having quantised values of imaginary index following the pump profile.

3.3 Designing a Ridge Guided OSL
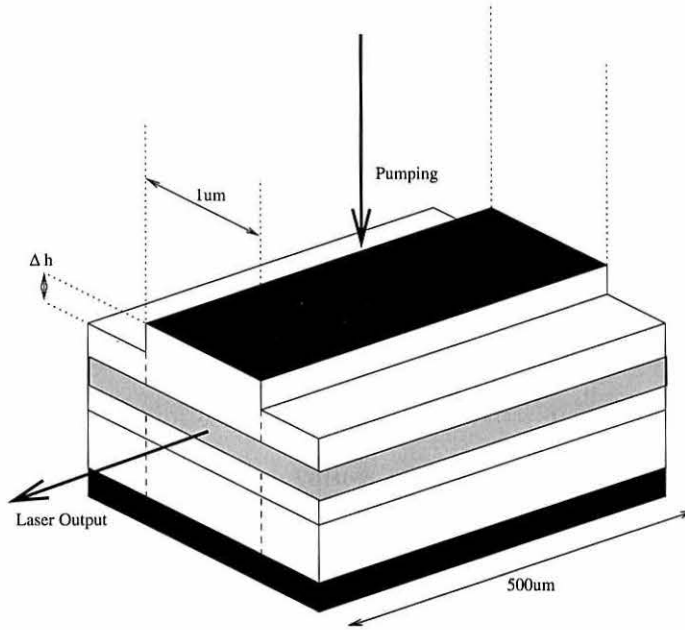
Figure 3.7: *Structure of the Ridge-Waveguide OSL*

To increase the lateral confinement of the OSL while retaining single mode operation, a *ridge waveguide* configuration (Figure 3.7) can be employed. A ridge waveguide has an increase in the thickness of the structure over the intended guiding region. This gives rise to an increase in the effective index over the pump stripe width. The variation in the effective index in the y direction thus forms a waveguide, and the electromagnetic wave is confined

51

totally to an area of the transverse (x,y) plane.

Figure 3.8. shows how the effective index of the transverse mode E_0^x varies as the thickness of the top layer is increased by Δh, the ridge height. A previously optimised active layer thickness of 0.15μm is assumed.

3.3.1 Changing the Ridge Dimensions
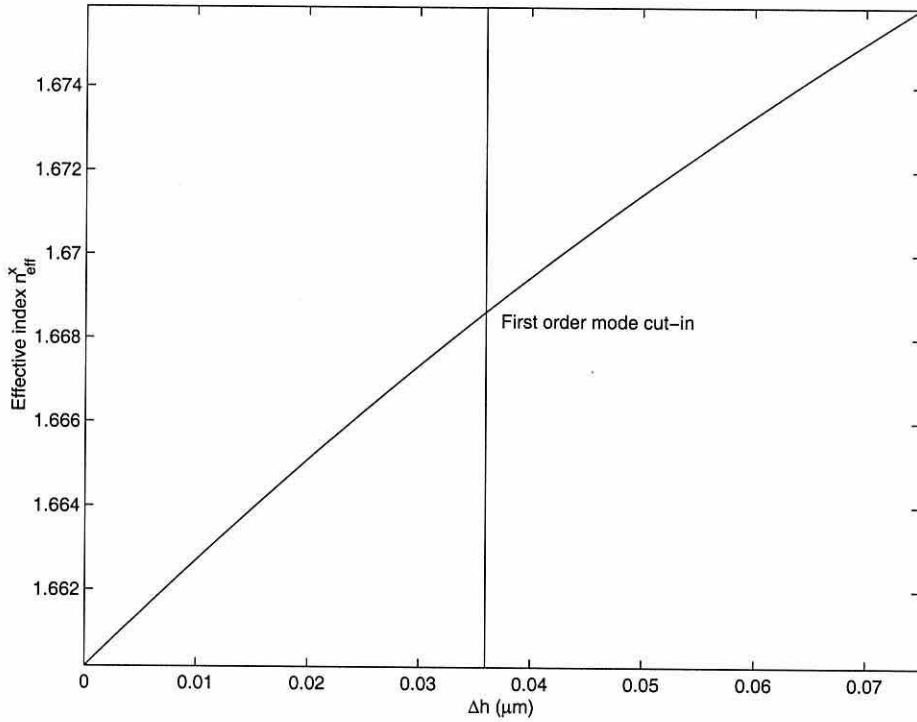
Figure 3.8: *Effect of varying rib height Δh on optical confinement of the $E_0^x(y)$ mode*

From Figure (3.8), it is seen that for rib height, Δh, greater than $\approx 0.04\mu$m, the waveguide structure becomes multi-mode in the transverse plane. Figure (3.9) shows the effect of varying the capping layer thickness on lateral confinement. Choosing a required lateral confinement of $\Gamma^y = 0.5$, it can be seen

from Figure (3.9) that $\Delta h \approx 0.025 \mu$m is required. $\Gamma^y > 0.5$ is possible with this configuration, but may lead to multi-mode operation in the transverse coordinate.

As seen in Section 3.1, the presence of gain in the active region gives rise to a difference in the imaginary part of the refractive index of around $\Delta Im(n) \approx 5 \times 10^{-5}$. The difference in the real refractive index in the rib laser is of order, $\Delta Re(n) \approx 10^{-2}$. In the rib-waveguide laser, $\Delta Re(n) >> \Delta Im(n)$ and so the imaginary part of the refractive index variation is negligible. The propagation constants of the mode are therefore unaffected by changes in gain due to optical pumping.
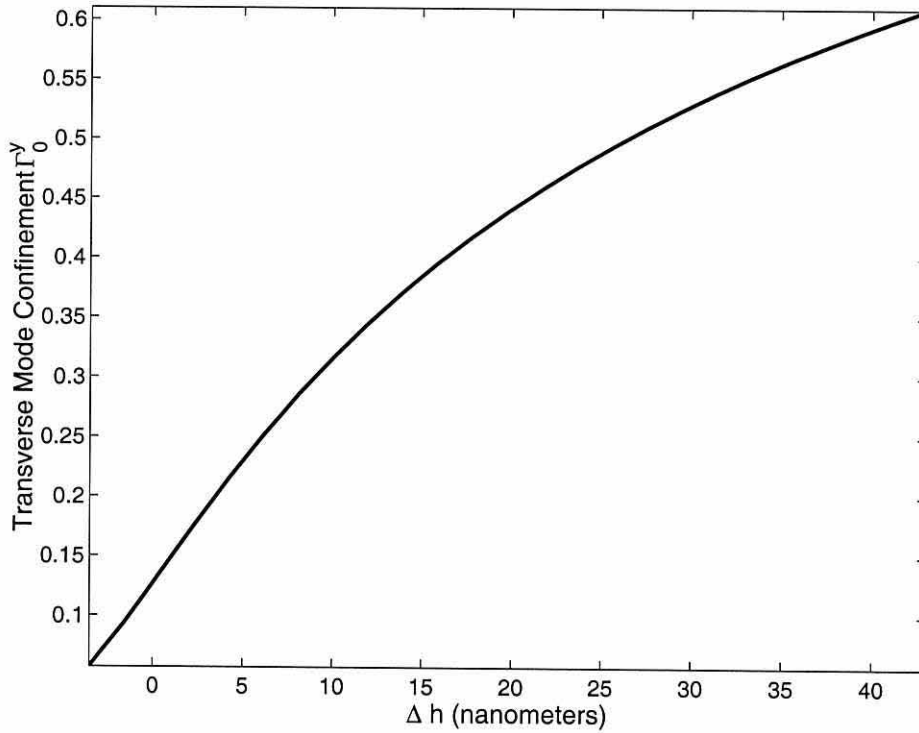
Figure 3.9: *Effect of varying the thickness on optical confinement*

3.4 Summary

In the above analysis the OSL design suggested in [16] has been optimised in terms of optical confinement. The effects of using both gain-guided and ridge guided configurations for lateral confinement have been explored. It has been seen that the gain guided structures offer higher confinement, but require a significant reduction in gain for single mode operation at larger pump beam widths.

Rib wave-guide configurations provide comparable confinement in the y direction that is independent of gain. For an active region width of 1μm, optical confinement of $\Gamma^y = 0.5$ can be achieved using a rib height of $\Delta h = 0.025\mu m$ over the active area (Figure 3.6.).

The dependence of the threshold gain of a laser on confinement has been discussed. The most striking improvement in confinement was seen in the transverse mode. By increasing the active layer thickness from 0.05μm to 0.15μm, the transverse confinement is increased from 0.2 to 0.5. This suggests that there is a considerable advantage in increasing the active layer thickness in optically pumped lasers.

Chapter 4

Analysis of Parallel Grating DFB lasers

4.1 Analysis of DBR Reflectors

It is widely known that low threshold gain lasers may be fabricated using Distributed Bragg Reflectors (DBRs), also known as Bragg mirrors.

The most common method of implementing Bragg reflectors in semiconductor lasers is by a periodic variation in the thickness of one of the planar layers comprising the laser waveguide. A DBR grating reflects light incident at an angle normal to the plane of the perturbation provided the Bragg condition is satisfied;

$$\Lambda = \frac{l\lambda'}{2} \tag{4.1}$$

where Λ is the grating period, $\lambda' = \lambda/n$ is the wavelength of light inside the medium of refractive index n and l is a positive integer.

The wavelength selectivity of Bragg gratings is of considerable importance in their application to the design of semiconductor laser systems. By using Bragg reflectors of specific wavelengths, it is possible to select the allowed frequency of oscillation in the laser. Alternatively, DBR gratings may be used to select allowed angles of emission or absorption of radiation into or out of the laser.

4.1.1 Maxwell's Wave Equation in a Perturbed Waveguide

A planar, or slab waveguide is considered having a periodic perturbation in the thickness of the guiding layer, as seen in Figure 4.1. The waveguide is

assumed to be semi-infinite in the y and z directions, and the perturbation occurs only in the z direction.
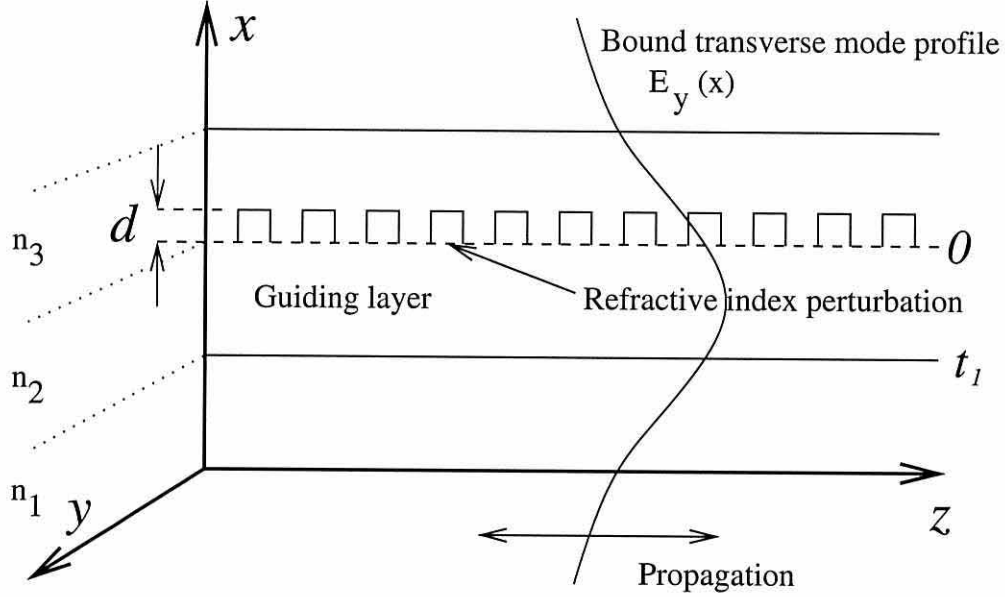
Figure 4.1: *Slab waveguide with a refractive index perturbation forming a DFB grating.*

Assuming a harmonic time dependence, light in the waveguide propagates as a linearly polarised wave obeying:

$$\nabla^2 \mathbf{E}(x, z) + n(x, z)^2 k_o^2 \mathbf{E}(x, z) = 0 \tag{4.2}$$

The refractive index perturbation is represented by:

$$n^2(x, z) = n'^2(x) - \Delta n^2(x, z) \tag{4.3}$$

It is expected that the amplitude of the electromagnetic wave oscillation will vary as it propagates along the z direction in the structure, therefore for

the TE modes, the field takes the form of the general solution;

$$\mathbf{E}(x,z) = E_y(x)(A(z)e^{j\beta z} + B(z)e^{-j\beta z}) \tag{4.4}$$

with $A(z)$ and $B(z)$ as constants to be determined.

The variation in refractive index is not so large as to significantly alter the transverse mode profile from that of an 'unperturbed' structure. The planar wave equation is therefore still satisfied;

$$(\frac{\partial^2}{\partial x^2})E_y(x) + (n'^2(x)k_o^2 - \beta^2)E_y(x) = 0 \tag{4.5}$$

Variation of the field amplitude in the z direction due to the refractive index perturbation is very much less than the periodic variation of the propagating wave, so that;

$$\frac{\partial^2}{\partial z^2}A(z) \approx \frac{\partial^2}{\partial z^2}B(z) \approx 0 \tag{4.6}$$

Using (4.6) and (4.5) in (4.2) and substitution of (4.3) and (4.4) into (4.2) leads, after multiplication by $E_y(x)$ and integration over all x to:

$$\begin{aligned} &\frac{\partial}{\partial z}A(z)e^{-j\beta z} - \frac{\partial}{\partial z}B(z)e^{j\beta z} = \\ &\frac{jk_0^2}{2\beta C}\int \Delta n^2(x,z)E_y^2(x)(A(z)e^{j\beta z} + B(z)e^{-j\beta z})dx \end{aligned} \tag{4.7}$$

Where C is a normalisation constant given by;

$$C = \int_{\infty} E_y^2(x)dx \tag{4.8}$$

58

4.1.2 The Refractive Index Perturbation

The unperturbed refractive index profile shown in Figure 4.1 may be described outside the grating depth, d, by;

$$n'^2(x,z) = \begin{cases} n_1 & (x < t_1) \\ n_2 & (t_1 < x < 0) \\ n_3 & (0 < x) \end{cases} \tag{4.9}$$

The index perturbation, $\Delta n^2(x,z)$, is zero everywhere outside the region $x < -d < 0$. Within the grating region, the refractive index perturbation is periodic in y and for the rectangular perturbation shown in Figure 4.1 can be expressed as a Fourier series having harmonic components of order m. :

$$\Delta n^2(x,z) = \sum_{m \neq 0} \Delta n^2(x,y) e^{jm(2\pi/\Lambda)z} \tag{4.10}$$

Substitution of (4.10) into (4.7) with $m = l$ and equating coefficients of the backward and forward travelling waves gives:

$$\frac{\partial}{\partial z} A(z) = j\kappa_l B(z) e^{-2j\Delta\beta z} \tag{4.11}$$

$$\frac{\partial}{\partial z} B(z) = j\kappa_l^* A(z) e^{2j\Delta\beta z} \tag{4.12}$$

Where $\Delta\beta = \beta - \frac{l\pi}{\Lambda}$ is the detuning of the grating from the propagation constant at the Bragg wavelength, $l\pi/\Lambda$. l is the diffraction order of the grating, defined as the harmonic order of the grating coupling the backward and forward propagating waves. Λ is chosen so as to ensure that, for a particular value of l, $\Delta\beta$ is zero. The contributions to the coupling from

59

other grating orders is then negligible, as they are far from satisfying the Bragg condition. The coupling coefficient, κ_l, for the lth diffraction order is given by:

$$\kappa_l = \frac{k_0^2}{2\beta} \frac{\int \Delta n^2(x,z) E_y^2(x) dx}{\int E_y^2(x) dx} \qquad (4.13)$$

4.1.3 Calculating the Coupling Coefficient

The Fourier coefficient $\Delta n^2(x)$ for the lth diffraction order may be calculated as:

$$\Delta n^2(x) = \frac{1}{\Lambda} \int_0^\Lambda \Delta n^2(x,z) e^{\frac{-2\pi j l z}{\Lambda}} dz \qquad (4.14)$$

For the planar waveguide with a rectangular index perturbation shown in Figure 4.1, $\Delta n^2(x,z) = n_2^2 - n_3^2$ when $-d < x < 0$ and $0 < z < \Lambda$. The integral of (4.14), when $(-d < x < 0)$, can thus be evaluated analytically as:

$$\Delta n^2(x) = (n_2^2 - n_3^2) \frac{sin(\pi l \Lambda'/\Lambda)}{\pi l} \qquad (4.15)$$

The coupling coefficient of the lth harmonic of the rectangular grating is thus given by substitution of (4.15) into (4.13):

$$\kappa_l = \frac{k_o^2(n_2^2 - n_3^2)}{2\pi\beta_l} \int_d [E_y(x)]^2 sin(\frac{\pi m \Lambda'}{\Lambda}) dx \qquad (4.16)$$

The integral in (4.16) is evaluated numerically using a Gaussian quadrature. A variety of symmetric grating shapes may be analysed by replacing the constant Λ' by an x dependent function describing the required profile. For a sinusoidal grating;

60

$$\Lambda'(x) = \frac{\Lambda}{\pi}cos^{-1}(\frac{2x}{d}) \tag{4.17}$$

is adopted, and for a symmetric triangular grating the expression;

$$\Lambda'(x) = \Lambda(\frac{1}{2} - \frac{x}{d}) \tag{4.18}$$

is substituted for Λ in (4.16).

4.1.4   The DBR Reflectivity Function

Equations (4.11) and (4.12) describe the coupling of the counter propagating electromagnetic waves. By assuming a general solution for the equations and integrating over the length of the grating, L, an expression is derived for the complex reflectivity of the perturbed waveguide after [1].

$$R(\Delta\beta) = \frac{j\kappa_l sinh(SL)}{\Delta\beta sinh(SL) - jScosh(SL)} \tag{4.19}$$

Where $S = \sqrt{\kappa^2 - \Delta\beta^2}$ and the complex reflectivity takes the form;

$$R(\Delta\beta) = r(\Delta\beta)e^{j\Theta(\Delta\beta)} \tag{4.20}$$

With $r(\Delta\beta)$ describing the amplitude reflectivity and $\Theta(\Delta\beta)$ representing the change in phase of the reflected wave.

The reflectivity of the DBR grating decreases rapidly with increasing detuning from the Bragg condition. The reflectivity of a typical DBR grating is shown in Figure 4.2.

In DBRs it is more convenient to consider the longitudinal modes of the optical field as standing waves. In this way, the DBR analysis is exactly
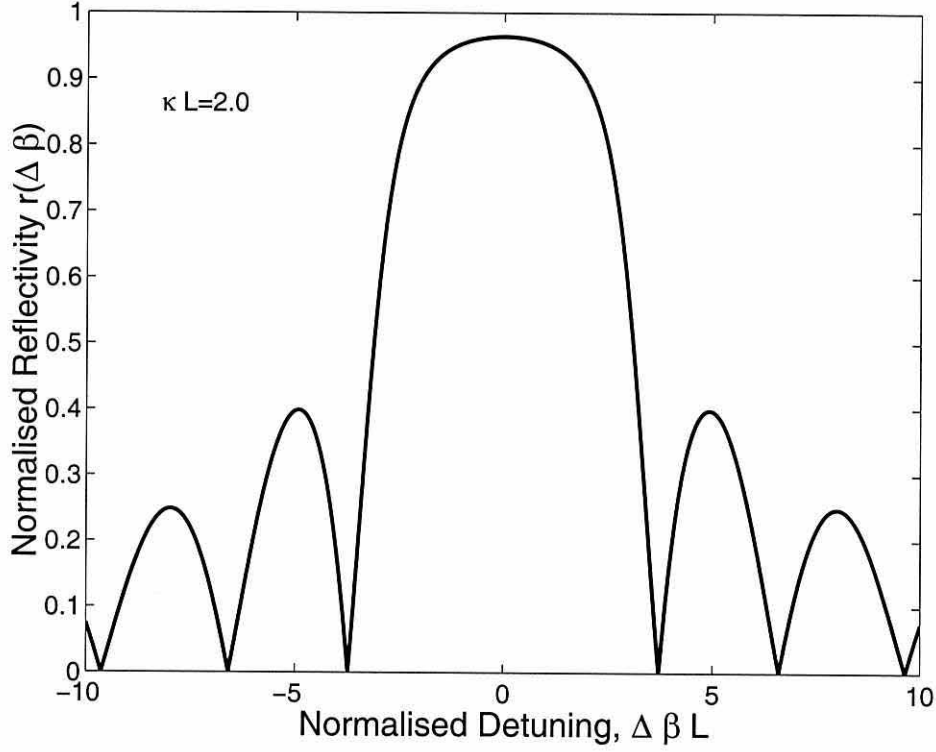
Figure 4.2: *Reflectivity function $r(\Delta\beta)$ for a DFB grating having $\kappa L = 2.0$.*

equivalent to that of an electron wave-function in a one dimensional semi-conductor crystal. The periodicity of the potential function of such a crystal restricts the propagation of the electronic wave-function to certain energy levels, with stop bands in between. In a similar manner a DBR grating imposes a 'stop band' around the Bragg wavelength.

4.2   DBR and DFB Laser Configurations

There are two ways in which DBRs are commonly used to construct semi-conductor lasers, known as DBR and DFB configurations;

(a) DBR Laser

Pump Applied only Between Reflectors

Periodic
Corrugation
Of Rib

Pumping Applied Over Length of Entire Structure

(b) DFB Laser
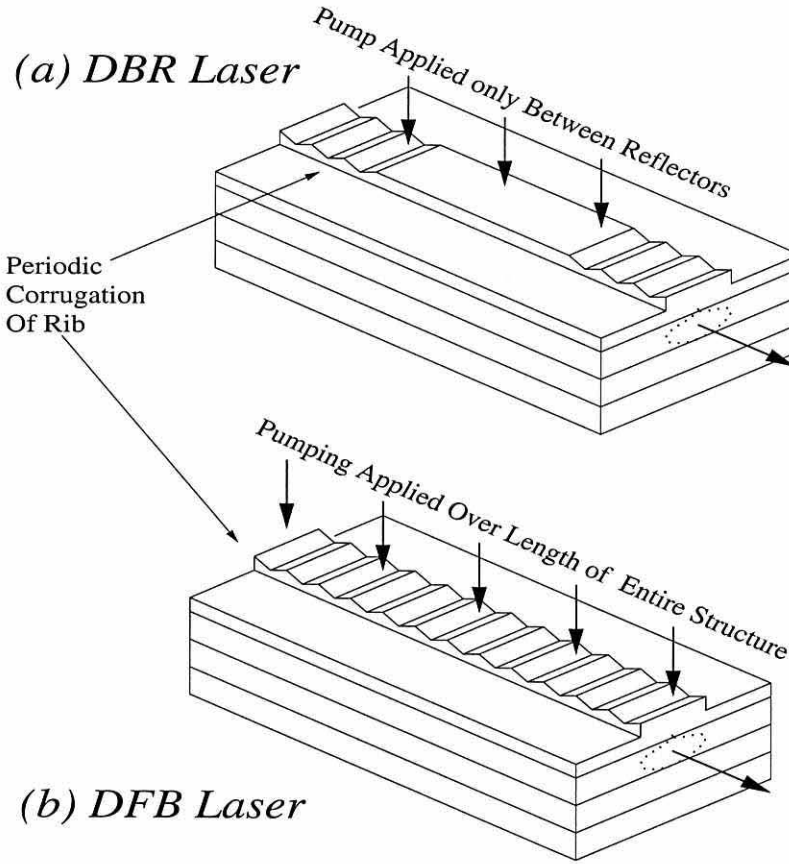
Figure 4.3: *Structure geometry of typical DFB and DBR lasers, showing the different grating configurations used to achieve feed-back.*

4.2.1 DBR Lasers

The first method, shown in Figure 4.3(a), is to fabricate the DBR reflectors as distinct un-pumped sections at either end of a central active section. Here, the DBR gratings act as a replacement for the end facet reflectors used to form a Fabry-Perot laser. From [1] the analysis of round-trip cavity losses in a Fabry-Perot laser cavity of length, L, results in the following threshold gain condition;

$$r_1(\Delta\beta)r_2(\Delta\beta)e^{-j\beta 2L}e^{j[\Omega_1(\Delta\beta)+\Omega_2(\Delta\beta)]} = 1 \qquad (4.21)$$

where $r_1(\Delta\beta)$ and $r_2(\Delta\beta)$ are the amplitude reflectivities of the two end gratings and $\Omega_1(\Delta\beta)$ and $\Omega_2(\Delta\beta)$ are the amount by which they alter the phase of the incoming wave.

The complex propagation constant β, where $k_0 = 2\pi/\lambda$ is the free space wavenumber, is given by;

$$\beta = k_0 n + j\zeta \qquad (4.22)$$

n is the refractive index of the medium and ζ is the sum of the gain and loss in the media, so that;

$$\zeta = \gamma - \alpha \qquad (4.23)$$

if γ is the material gain and α the material loss.

The real and imaginary parts of (4.21) can be separated to give the following expressions for the gain and phase detuning $(\Delta\beta)$ values at threshold. From the real part;

$$\gamma_{th}(\Delta\beta) = \frac{1}{2L}ln(\frac{1}{r_1(\Delta\beta)r_2(\Delta\beta)}) + \alpha \qquad (4.24)$$

and from the imaginary components:

$$(\Omega_1(\Delta\beta) + \Omega_2(\Delta\beta)) + 2nk_0L = m2\pi \qquad (4.25)$$

m is any non-zero integer. The locations of the discrete longitudinal modes are therefore found at points on the $\Delta\beta$ axis of the gain function

64

where (4.25) is also satisfied. It can be seen by inspection of (4.25) that the spacing of the modes along the detuning axis is dependent upon the phase change of the wave as it is reflected by the gratings.

4.2.2   DFB Lasers

Another method exists by which a laser may be constructed using DBR gratings, as seen in Figure 4.3. Unlike the DBR design, a Distributed Feed-Back (DFB) laser consists of a single longitudinal section. An analysis of a DFB structure may therefore be achieved via the reflectivity function for a single DBR mirror (4.19) by substituting $\Delta\beta$ with a complex independent parameter;

$$\Delta\beta' = \Delta\beta + j\gamma \qquad (4.26)$$

It can be seen from (4.11) and (4.12) that the substitution of (4.26) is consistent with an exponential change in the amplitude of the propagating wave with distance, z, where γ is the gain coefficient.

The magnitude of the complex function $R(\Delta\beta')$ with $\kappa L = 1$ is shown in Figure 4.4 for normalised values of gain and detuning. The peaks represent poles of the function[1], suggesting that for certain values of gain and detuning, the reflectivity of the grating becomes infinite. In physical terms, the singularities arise due to the gain γ overcoming the losses in the grating, resulting in stable oscillation of the electromagnetic wave within the grating

---

[1]Although the poles appear to have finite values of Reflectivity in Figure 4.4, this is due to the finite resolution of the graphing function
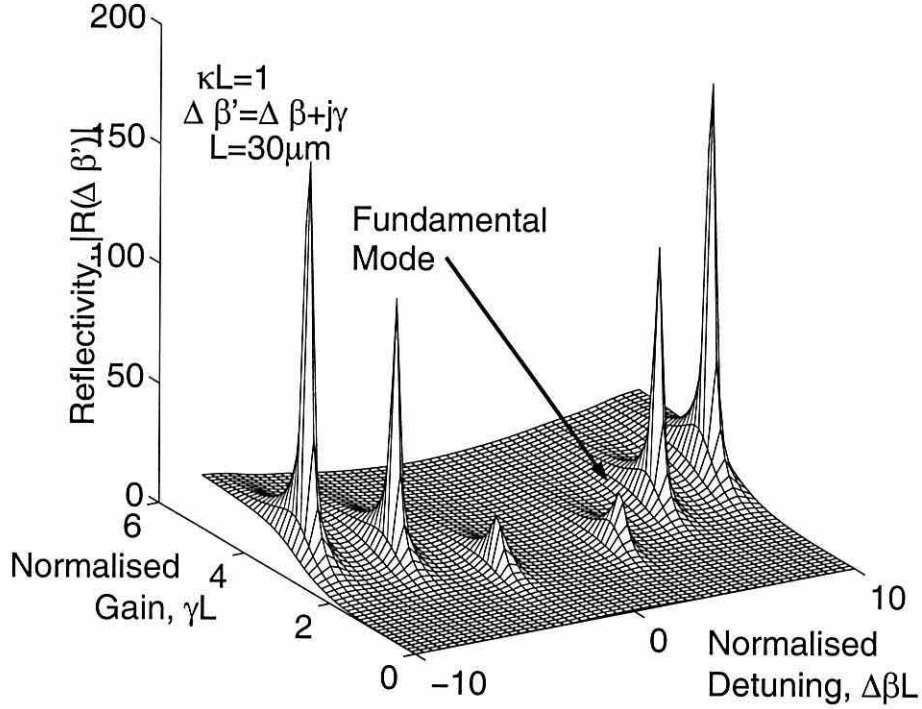
Figure 4.4: *Plot of the reflectivity function, R, showing six singularities representing the longitudinal modes of the structure.*

region. The poles of Figure 4.4 therefore represent the longitudinal modes of the DFB laser.

It is evident from Figure 4.4 that the modes appear degenerate around the Bragg frequency, with the mode spectra being symmetrical around $\Delta\beta = 0$. The modes are not quite degenerate however as there will be a minute difference between the threshold gains of the modes. this is because of the slightly weaker confinement of even modes, and will be ignored.

As they are composed of a single grating section, DFB designs are more straightforward to fabricate than DBR lasers and have the advantages of low lasing threshold and compact size. It can be seen from Figure 4.4 however,

that the fundamental longitudinal mode is one of a degenerate pair. More than one mode can therefore oscillate simultaneously at threshold. As with DBR lasers, the location of the modes is determined by the phase shift experienced by a wave reflected by the grating. It is common practice [1] to include a quarter period phase shift in the grating to give single mode lasing at the Bragg wavelength.

4.3 APM Method for Locating the Longitudinal Modes of a DFB Laser

It is only the poles of the complex reflectivity function that are of interest in locating the longitudinal modes of the DFB laser. An inspection of (4.19) with the substitution of (4.26) reveals that the numerator contributes no additional poles to those attributed to the zeros of the denominator. The longitudinal modes may therefore be sought as the zeros of the function:

$$R(\Delta\beta + j\alpha) = (\Delta\beta + j\alpha)sinh(SL) - iScosh(SL) \qquad (4.27)$$

Where $S = \sqrt{|\kappa|^2 - (\Delta\beta + j\alpha)^2}$.

The solutions are conveniently located using an adaptation of the Argument Principle Method (APM) technique used to find the transverse waveguide modes in the previous chapter. For the location of the longitudinal modes, a rectangular contour is used that resides entirely on the positive side of the gain axis. The region of interest is defined by a maximum detuning range and maximum gain.

If necessary, the singularity of (4.27) at $S = \kappa$ may be excluded from the contour using a construction such as the one shown in Figure 4.5. The contour consists of an inner circle enclosing the singularity and connected to the (rectangular) outer perimeter by parallel paths. The contributions to the APM contour integral from the connecting bridges is zero, as the same path is traversed in opposite directions.
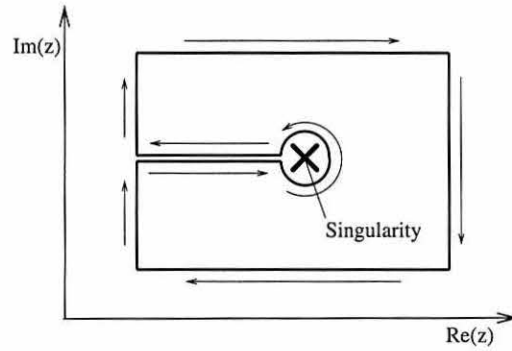
Figure 4.5: *Integration contour used to exclude the singularity at $s = 0$. The contour is bound by both inner and outer loops connected by a single bridge.*

In the limit as the radius of the inner contour tends to zero, the relevant contribution can be evaluated exactly as $S_m = \kappa^m$. Only the contribution from the outer contour must then be evaluated numerically. As for the location of transverse modes described in Section 2.5, the locations of the modes may then be found as the solutions to a polynomial;

$$p(z) = \prod_{i=1}^{S_0} (z - z_i) = C_1 z^1 + C_2 z^2 + C_3 z^3 + ... + C_{S_0} z^{S_0} \tag{4.28}$$

where the z_i are the zeros of $f(z)$, with $i = 1, 2, ..., S_0$. The coefficients C_n

68

are found, as before, using the recurrence relation:

$$C_k = \frac{1}{(k - s_0)} \sum_{j=1}^{k} S_j C_{k+j} \qquad (4.29)$$

Although normalised data exists giving values of threshold and detuning for a range of values of κ, extension of the APM to calculate longitudinal modes where it is already employed to locate transverse modes is relatively straightforward and yields a large number of solutions in a relatively short time.

The high-gain approximation (HGA) [1] is a common method of locating the modes analytically. Using the HGA, the assumption is made that the order of the gain greatly exceeds that of the coupling coefficient, κ, and detuning, $\Delta\beta$. It is then possible to derive equations giving the wavelengths and gains of the modes. For a large number of applications, however, it is a requirement that the gain in the laser is kept to a minimum and the assumption of the high gain approximation may be invalid.

A more accurate, but less convenient technique is to use an iterative downhill technique. This large class of numerical methods, including *Mullers method* and *Newtons method* as well as some less formal methods. An example of an appropriate technique not requiring the derivative of the function to be known is used in [4]. Although the accuracy of these methods is only restricted by the accuracy of the computer upon which they are executed, they do require an initial guess to be made. The provision of an initial guess is not always convenient, particularly if a large number of modes are to be found. The APM, however, requires no initial guess and can locate a large number of modes simultaneously. As the density of the longitudinal modes

69
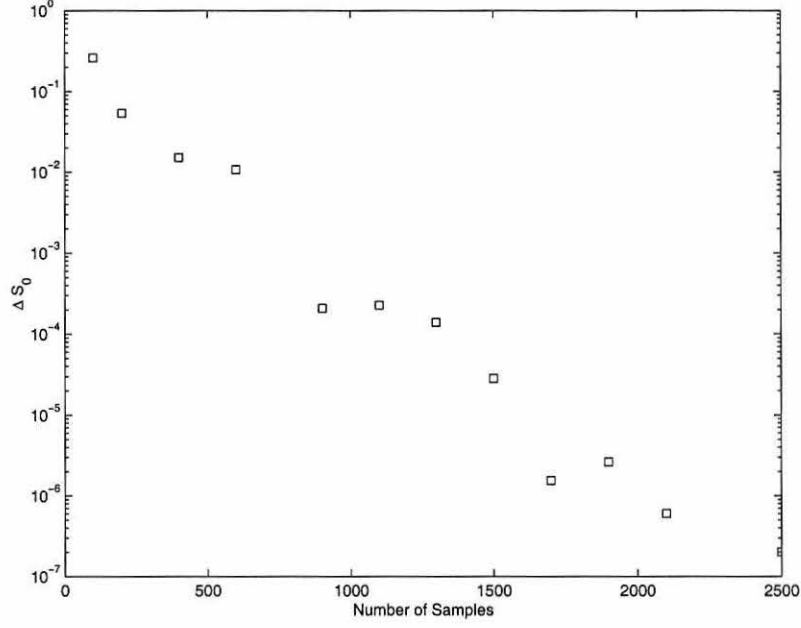
Figure 4.6: *Plot of the error in S_0 with increasing sampling. The distribution of the data can be attributed to the accumulation of overflow during the quadrature.*

is likely to be large due to the long length of the grating compared to the operating wavelength, the APM is chosen as the analysis technique for locating the modes of DFB lasers.

4.3.1 Application of the APM to a DFB Laser

Considering an in-organic DFB double-heterostructure laser structure, operating at 1.55μm, a typical value for κL, obtained by the coupled mode analysis described previously, is about 2.5.

The argument principle technique described in the previous section can be applied to give exact values for the modes using a rectangular contour

70
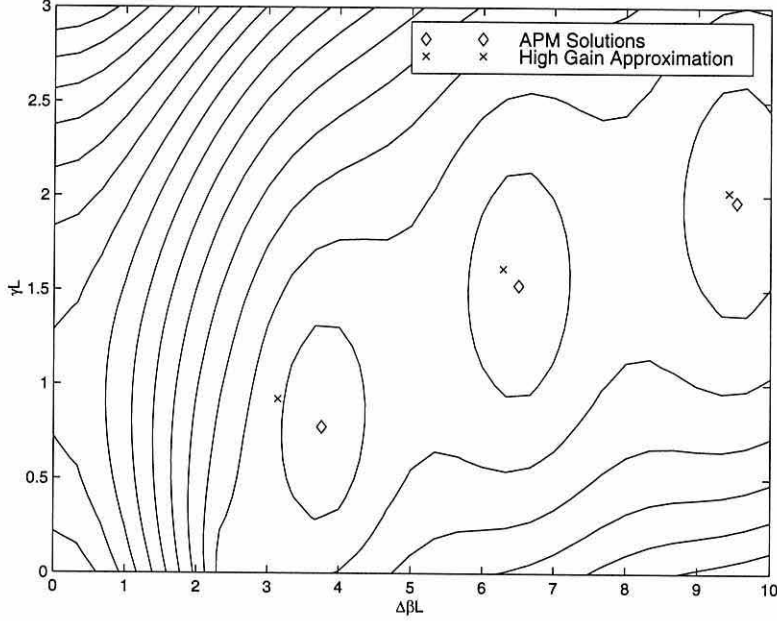
Figure 4.7: *Modes found by the APM. As expected, the Argument Principle Method locates all solutions of the function $R(z)$ exactly whereas the high gain approximation is only valid for $\gamma \gg \kappa$.*

enclosing the area shown. The success of the APM is greatly dependent on the accuracy of the numerical evaluation of S_m. A simple measure of the accuracy of the quadrature is the speed of convergence to an integer value in the evaluation of S_0, the contour integral used to determine the number of solutions present.

Figure 4.6 shows how the accuracy of the quadrature follows an inverse logarithmic relationship with the number of samples used in the evaluation.

The locations of the modes converge to a resolution within $\Delta z_1 \approx 10^{-5}$ with $\Delta S_0 < 10^{-6}$ (where Δz_1 is the error in the first mode) requiring ≈ 2500 samples for each side of the rectangular contour.

The APM found three longitudinal cavity modes within the contour, having values for $\Delta\beta L + i\gamma L$ of $3.7570 + i0.7748$, $6.5042 + i1.5252$ and $9.5330 + i1.9690$. All three modes were found simultaneously within five seconds on a Sun Workstation.

Figure 4.7 shows a plot of the modes in the solution space. For comparison, the locations of the modes provided by the analytic high gain approximation [1] are also shown.

It can be seen in Figure 4.7 that the high gain approximation may not provide sufficiently accurate solutions. For the lower order modes, the approximation may not even be of sufficient accuracy for use as the initial guesses of an iterative down-hill technique.

4.4 Discussion

It has been seen in this chapter how the high reflectivities characteristic of Distributed Bragg Reflector (DBR) gratings may be utilised in the design of semiconductor lasers.

A method for the analysis of DBR gratings, based on the the Coupled Mode Theory (CMT), has been presented.

An advantage of the CMT is that it is relatively straightforward to implement as an extension to the analysis of transverse waveguide modes. The CMT is also capable of analysing a wide range of designs involving DFB gratings, including non-rectangular gratings. As the transverse analysis is performed separately, and only the resultant wave-function describing the intensity of the optical field is required for the CMT analysis, the longitudi-

nal modes may be sought for any index guided transverse waveguide.

However as the CMT makes the approximation that the shape of the transverse mode profile does not change as material gain over the guiding section is increased, CMT analysis is most appropriately applied to strongly index guided channel waveguide structures, where this assumption is most accurate. Gain guided lasers may be analysed using the CMT provided that the lateral structure is highly multi-mode, where it is appropriate to adopt a planar approximation for the waveguide.

The use of the Argument Principle Method (APM) for the location of longitudinal cavity modes of a DFB/DBR structure, described in Section 3.3, is unique. The advantages of using the APM compared to more usual methods such as the High Gain Approximation (HGA) have been discussed.

In the next chapter, it will be seen how the methods presented here may be applied to the analysis of organic semiconductor DFB lasers.

Chapter 5

Investigation of DFB-OSL Designs

5.1 Introduction

DFB lasers are particularly attractive in the design of Organic Semiconductor Lasers for two reasons. Firstly, they offer a means by which the threshold gain required to operate the laser can be reduced by minimising optical power losses from facets of the laser cavity. Secondly, the mechanical properties of organic materials enable an alternative group of highly cost-effective and versatile fabrication techniques, known as "soft lithographic techniques" (SLTs), to be considered.

Soft lithography is still being developed as a practical manufacturing process [17] [19]. Of particular interest for cost-effective mass production of organic DFB lasers are the *contact imprinting* processes [17]. These are normally applied to polymeric materials that can be partially cured and shaped by contact with a pre-shaped mould or dye under pressure. The mould is usually manufactured using some durable material such as SiO_2. Although not readily applicable to amorphous organic semiconducting materials like Alq3, that are comprised of weakly bonded small molecules and are therefore mechanically brittle, imprinting may be used to form gratings in thin polymeric films spin-coated between deposited layers of organic semiconductor. Subsequent to performing this analysis, considerable success was demonstrated using a grating imprinted onto the Bromochlorophenol Blue (BCB) substrate of an Alq3:DCM laser [20].

It is envisaged that, when the process of contact imprinting is perfected, the mould used to shape the underlying polymer could be re-used many times. As a result, non-rectangular grating shapes that are normally only obtainable

through complicated and expensive ablation and etching techniques are more economically viable.

In this chapter the design of a linear grating DFB organic semiconductor laser is approached using the analysis techniques described in Section 4.3. The effects on threshold gain of using various grating shapes as well as different positions of the grating in the layer structure are quantified theoretically.

5.2 DFB OSL Construction

The transverse structure of the DFB OSL described in this theoretical analysis is based on the practical device detailed in [16] and analysed in Section 3.1. The OSL is constructed from tris-(8-hydroxyquinoline) aluminium (Alq_3) vapour deposited onto SiO_2 where the emission is confined to a $0.3\mu m$ thick film of Alq_3, with the middle $0.05\mu m$ being doped with DCM dye to act as the active region.

Figure 5.1 shows the transverse waveguide after the adjustments to the layer dimensions recommended as a result of the analysis of Section 5.3 to maximise optical confinement. A periodic refractive index perturbation at the air/cover interface of the OSL is also shown in Figure 5.1. This initial location for the grating is selected as the most convenient for contact imprinting, alternative positions for the grating will be discussed in the analysis.
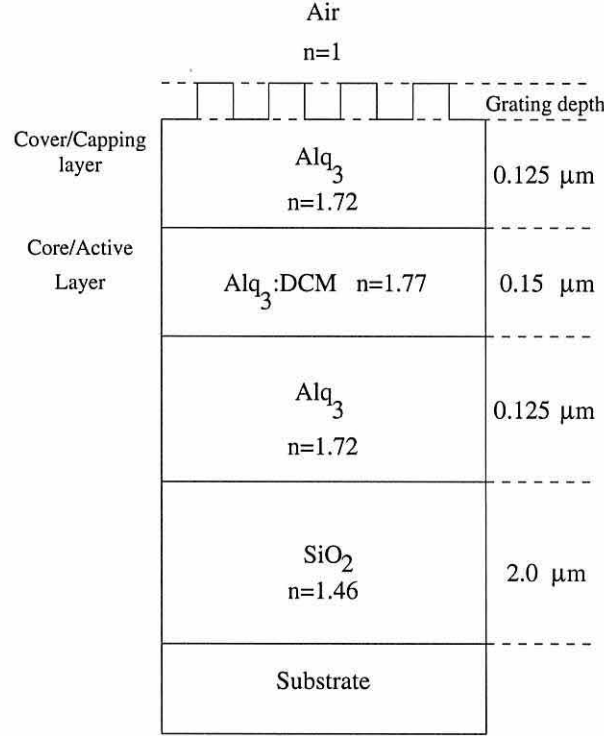
Figure 5.1: *Structure of the optimised OSL. The Active layer has increased width and the periodic grating at the air/cover interface is shown.*

5.3   Analysis of the DFB Structure

The threshold gain required to operate a laser is directly related to the amount of total optical loss from the active region. As well as reducing the loss in the transverse plane (by improving confinement to the active region), threshold gain may also be lowered by reducing the loss from the end facets of the laser cavity. In a DFB laser, optical confinement in the lateral direction may be improved by increasing the degree of *coupling* of the forward travelling wave to the reflected wave travelling in the opposite direction. A convenient parameter representing the coupling strength of a particular grat-

ing is the coupling coefficient, κ, which was seen in the previous chapter to be a function of an integration of the transverse mode field over the cross section of the grating.

5.3.1   Grating Shape and Thickness

By consideration of the Bragg condition ($\Lambda = m\pi/\beta_s$), a period of $\Lambda = 190nm$ is necessary to couple via the fundamental harmonic of the grating with the laser operating at 632nm.

Figures 5.2-5.4 show the effect of increasing the grating depth or *tooth height*, d, of the grating upon the coupling coefficient, κ, for the first three harmonics of rectangular, sinusoidal and triangular gratings respectively.

Although it can be seen that a rectangular grating profile provides a slightly better first order response, higher order harmonic rejection is improved with a sinusoidal or triangular grating. In practice, even a grating imprinted using a rectangular cast will have a significant degree of distortion. Figure 5.3 therefore shows both sinusoidal and rectangular grating data as effective upper and lower bounds of the true response of a practical rectangular structure. A grating depth of 50nm is selected for the DFB, a value well within an assumed practical limit of $\Lambda/2$ for imprinted gratings and yet giving a coupling coefficient of around $350cm^{-1}$ for a sinusoidal grating. Figure 5.5 shows the longitudinal modes of a 50μm long organic semiconductor DFB laser. The gain threshold of the fundamental mode is around $200cm^{-1}$ for a $50\mu m$ long grating, with a detuning of around 1.5 nm from the Bragg condition. This level of gain is comparable to that required to operate the

78

Figure 5.2: *Variation of coupling coefficient, κ, with tooth height for a rectangular grating imposed at the air/cover interface of a DFB OSL. Results are shown for $m = 1$ and $m = 3$, even order rectangular gratings produce no coupling.*

$500\mu m$ long FP-OSL described in Section 3.1. The DFB design therefore represents a considerable improvement in performance.

Substrate Gratings

Figures 5.6-5.8 shows the results of an analysis of the case where the grating is imposed upon the SiO_2 substrate of the device, which is a more typical configuration in many DFB OSLs to date [17].

It can be seen that the values of κ are generally lower, due to the lower index step either side of the corrugation. The longitudinal mode threshold
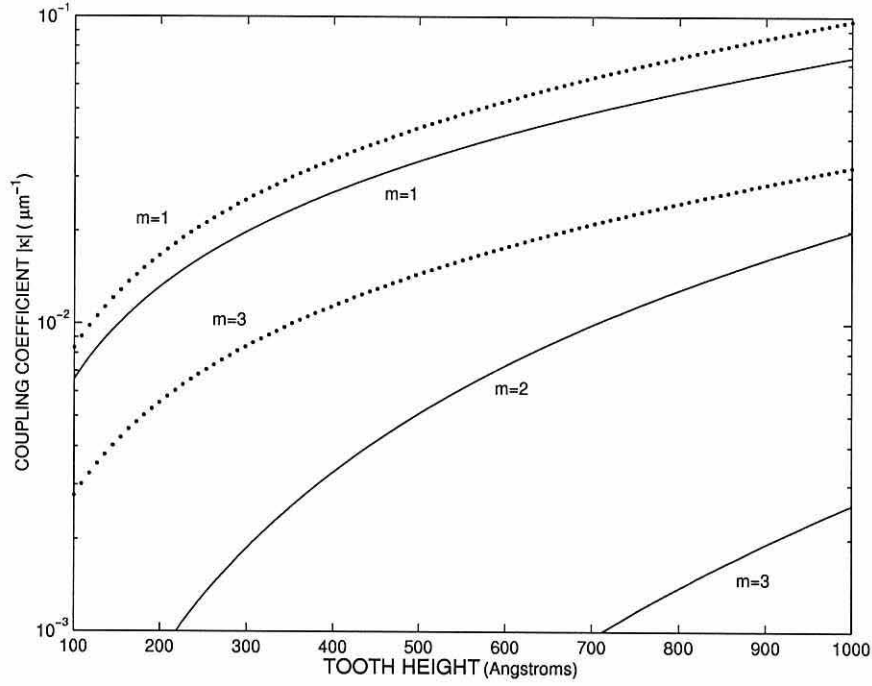
Figure 5.3: *Variation of coupling coefficient, κ, with tooth height for a sinusoidal grating at the air/cover interface of a DFB OSL. Results are shown for the first three values of grating order m. The dotted line shows the rectangular grating curve for comparison*

gains of a 50nm deep, 50μm long grating structure can be seen on figure 5.9. The gain thresholds of the modes are, as expected, slightly higher than for the surface imprinted grating.

5.3.2 Deeply Buried Gratings

Another common configuration for in-organic DFB lasers is to position the grating at the active region/cladding interface. This configuration is useful as it moves the grating near to the intensity peak of the transverse field profile, so affording greater overlap of the field with the grating. Calculations show
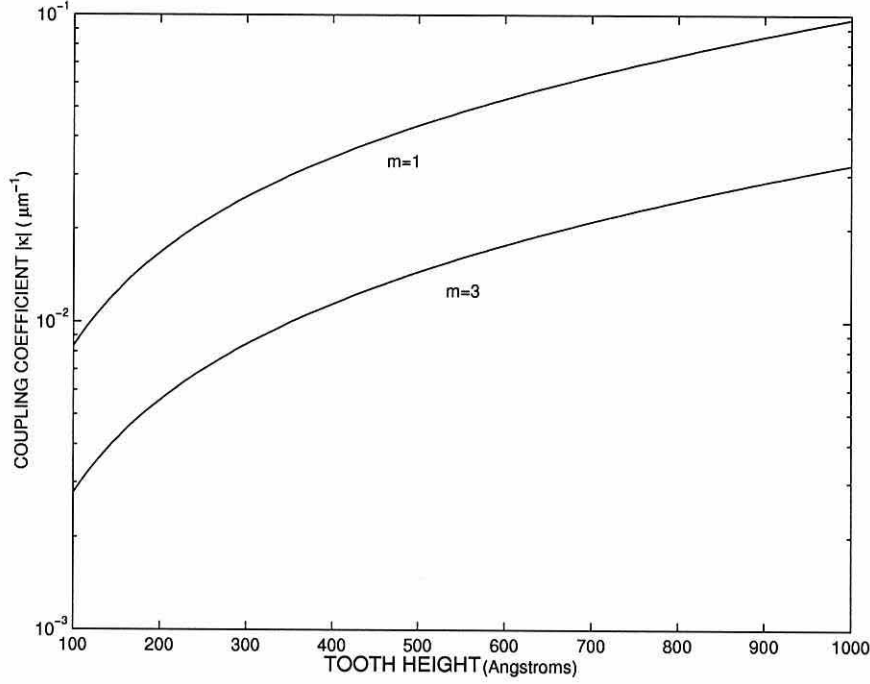
80

Figure 5.4: *Variation of coupling coefficient, κ, with tooth height for a triangular grating imposed at the air/cover interface of a DFB OSL. Results are shown for the first three values of grating order m.*

that for the OSL structure, however, this configuration yields a coupling coefficient of just 170cm^{-1}, and a threshold gain in the region of 400cm^{-1} for a 50nm deep grating and a 50μm long cavity. In OSLs, the low index step (Δn^2) between the doped active region and undoped cladding counteracts any benefit gained by having a greater overlap with the field profile. In fact Δn^2 at the active layer interface is just 10% of the index step at the air interface, whereas the overlap between the field and grating is improved by only 50% the total effect is therefore to reduce coupling by around 40-50%. The decrease in coupling efficiency is compounded by the fact that the *lower* index step at the air/cover interface gives a much smoother roll-off for the

81
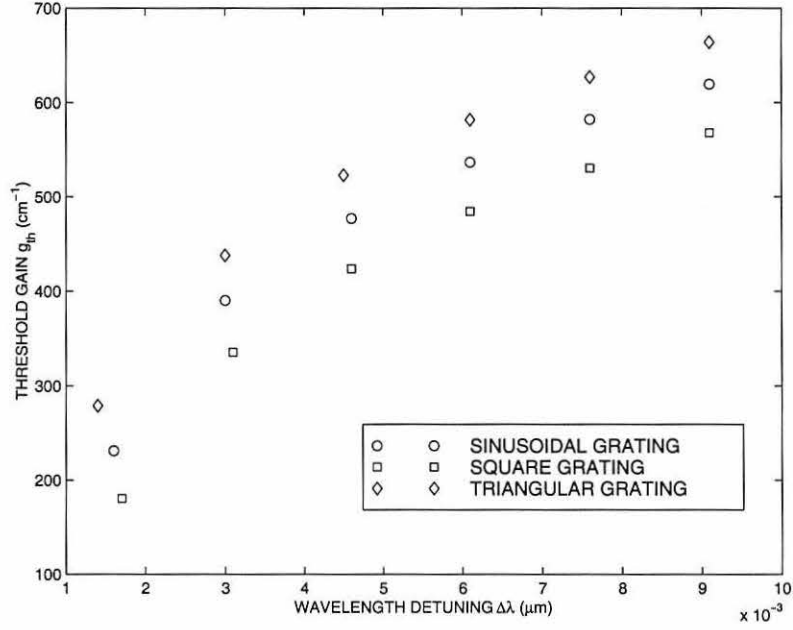
Figure 5.5: *Threshold gains of a 50μm OSL DFB with a 50nm deep grating at the air/cover interface.*

field profile and thus a higher overlap than is normally seen using a surface relief grating on an in-organic laser. By comparison, an in-organic DH laser typically has a relatively large index step at the active layer interface and a steep roll off at the surface, giving better coupling for gratings positioned deeply in the structure.

5.4 DBR Organic Semiconductor Lasers

In figures 5.10-5.11 the case is considered of a Organic Semiconductor DBR laser, having a central unperturbed length of active waveguide between two un-pumped gratings of length 50μm.

The gain is obtained by inclusion of the perturbed waveguide reflectivity
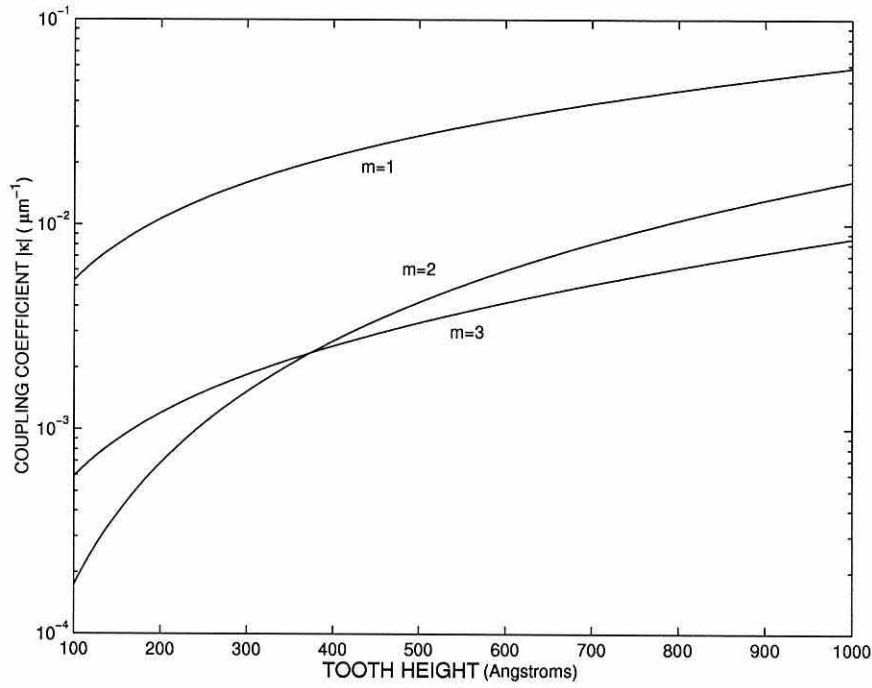
Figure 5.6: *Variation of coupling coefficient, κ, with tooth height for a rectangular grating imposed at the substrate interface of a DFB OSL. Results are shown for $m = 1$ and $m = 3$, even order rectangular gratings produce no coupling.*

function into the threshold condition for a Fabry Perot cavity. Figure 5.10 shows the gain of the DBR laser with several different lengths of centre section, L_c. The first order mode oscillating at the Bragg wavelength is shown to be dominant, with the gain threshold decreasing with each increase in L_c. Figure 5.11 shows a more detailed view of the first order mode peak. In both figures, the response for both sinusoidal and rectangular gratings is shown as an upper and lower bound on expected values.

Due to the 50% transverse confinement of the structure, the values for the gain threshold of both the DFB and DBR lasers may be assumed to be

83
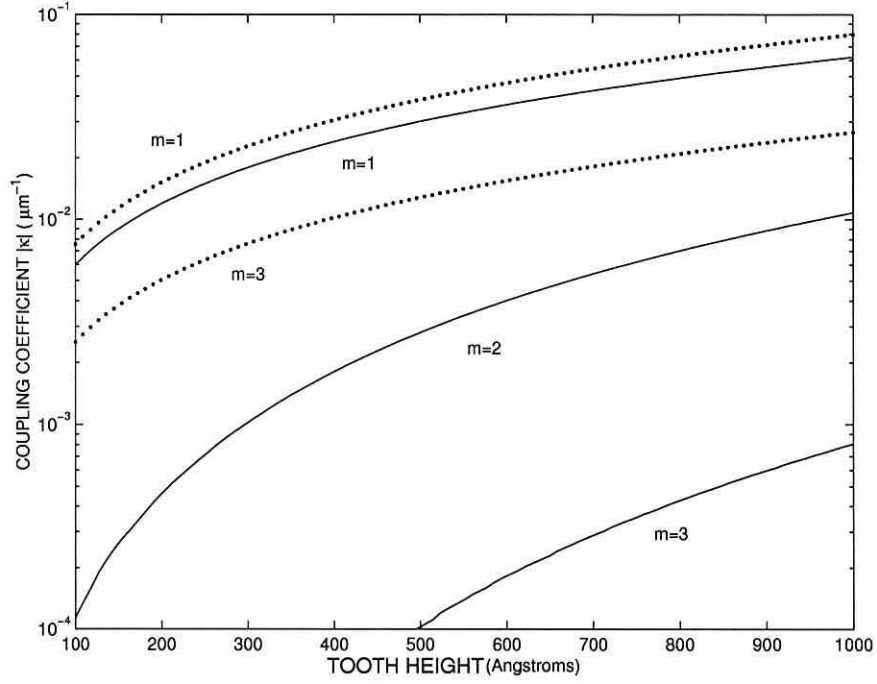
Figure 5.7: *Variation of coupling coefficient, κ, with tooth height for a sinusoidal grating at the substrate interface of a DFB OSL. Results are shown for the first three values of grating order m. The dotted line shows the rectangular grating curve for comparison.*

approximately twice that of the modal gain values given in the figures.

5.5 Discussion

The results of the previous section demonstrate the feasibility of using distributed feedback structures in the construction of low-threshold organic semiconductor lasers operating at 630nm. Modal gain values of around 200cm^{-1} are seen.

The lower index step at the air/cover interface might be expected to reduce the performance of any surface grating compared with the equivalent
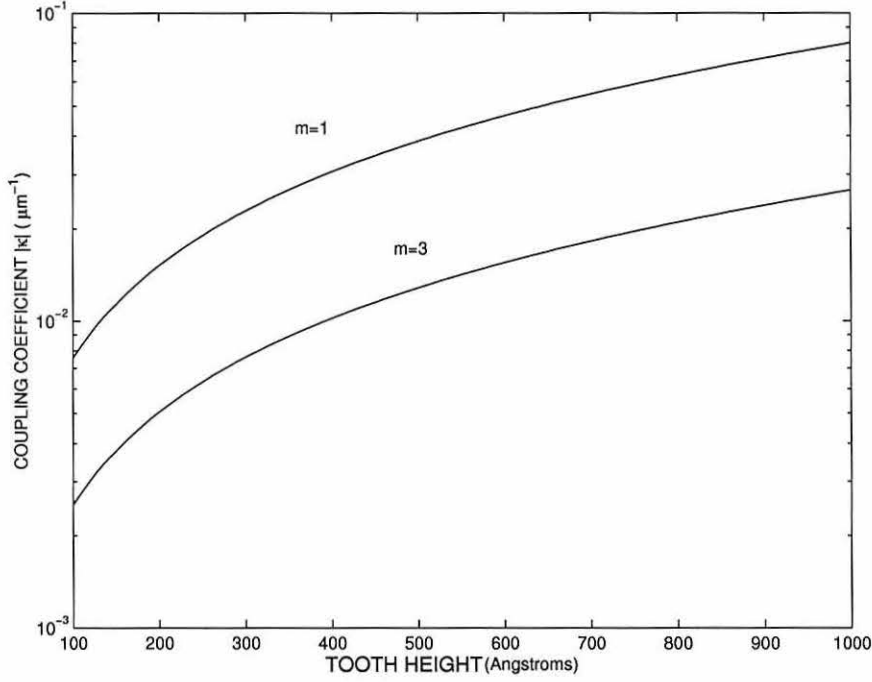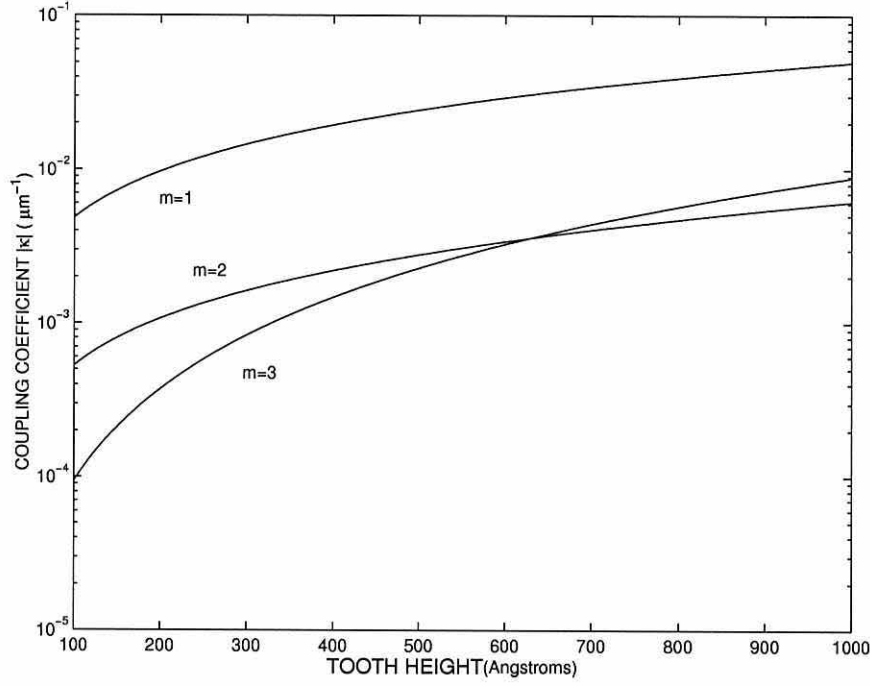
Figure 5.8: *Variation of coupling coefficient, κ, with tooth height for a triangular grating imposed at the substrate interface of a DFB OSL. Results are shown for the first three values of grating order m.*

in-organic semiconductor structure. However, in an in-organic semiconductor laser, the transverse field profile rolls off much more sharply at the cover due to the high index step there ($\Delta n \approx 3.0$), thus reducing the result of the overlap integral in the calculation of κ, the coupling coefficient. The advantages of having a surface grating in terms of a high index step are, in in-organic lasers, often sacrificed in favour of a higher overlap, as might be obtained by placing the grating deeper in the structure or at the substrate interface. With the much lower refractive indices of organic materials, gratings can be placed at the air/cover interface, giving a high index step and improving the convenience of manufacture, whilst maintaining a large coupling coefficient.

85
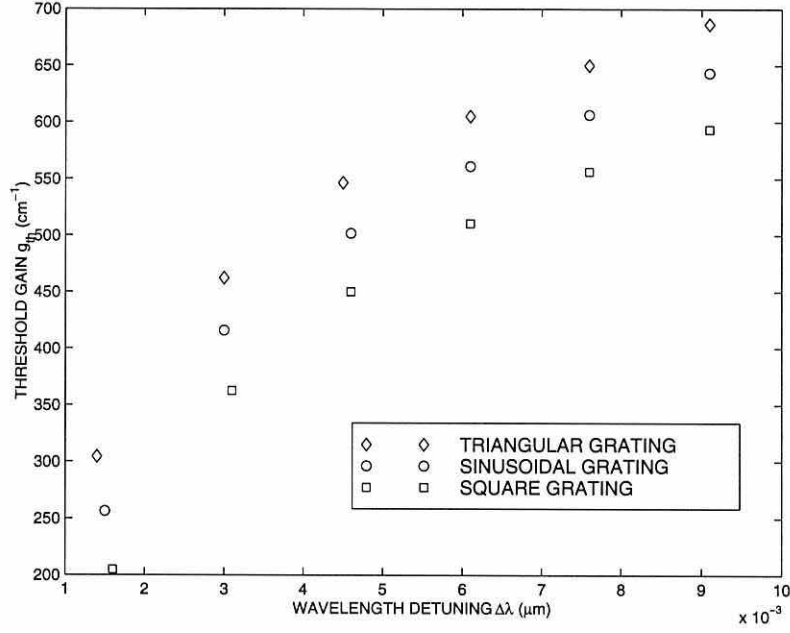
Figure 5.9: *Threshold gains of a 50µm OSL DFB with a 50nm deep grating at the air/cover interface.*

The combined advantages of a high coupling coefficient and long grating period for the operating wavelength, indicate that surface relief structures are an effective way of improving confinement in organic semiconductor lasers. To compare with the 500µm unperturbed Fabry Perot OSL discussed in [16], the observed αL product of the organic DFB laser with a 50nm deep rectangular/sinusoidal grating is ~ 2, giving a modal threshold gain of 40cm^{-1} compared to the value of 100cm^{-1} given for the laser analysed in [16].

Although offering a significant improvement over the performance of lasers employing Fabry Perot cavities, the DFB and DBR lasers described in this chapter use parallel gratings to provide feedback in one direction only. It is perceived that further advantages may be obtained by using more complex

86

grating shapes obtainable via contact imprinting.
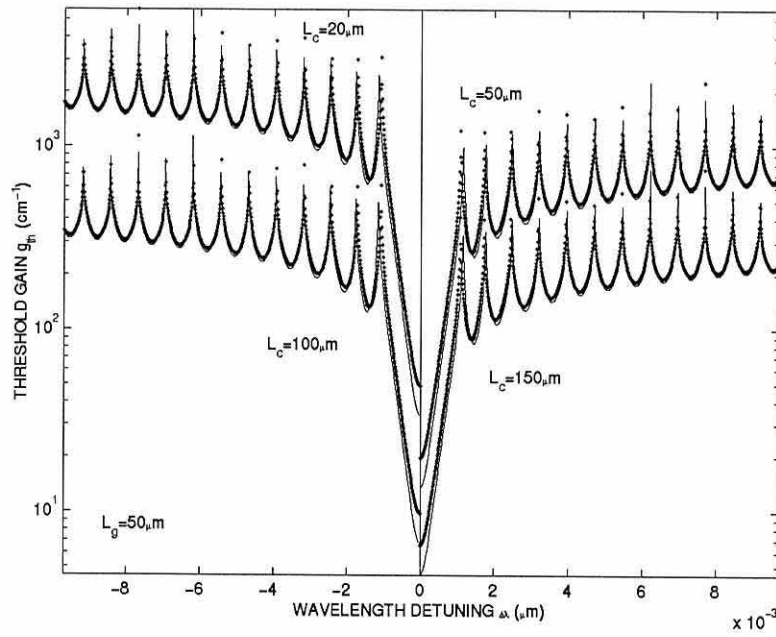
Figure 5.10: *Threshold gain for an OSL DBR structure having an unperturbed gain region of length L_c, bound by two $50\mu m$ Bragg reflectors. Although symetric about the origin, the gain curves for each value of L_c are shown on one side of the detuning axis origin only as an aid to clarity.*

Figure 5.11: *Detail of fundamental mode gain peak, the solid line represents a rectangular grating, and the dotted line denotes results for a sinusoidal grating. Although symmetric about the origin, the gain curves for each value of L_c are shown on one side of the detuning axis origin only as an aid to clarity.*

Chapter 6

Threshold Current Analysis of Parallel Grating DFB-OSLs

6.1 Introduction

In the previous chapters, it has been seen how a threshold gain analysis of an Organic Semiconductor Laser (OSL) may be performed in order to gauge the performance of a particular design. Until very recently [26], all practical Organic Semiconductor Lasers were optically pumped. Therefore the devices and designs so far discussed have been analysed under the assumption that they utilise optical pumping schemes. The problems arising from the electrical excitation of OSLs were discussed briefly in Section 1.1.2.

Recent experimental work [20] has provided sufficient information on the operating characteristics of practical DFB OSLs to enable initial optimisations of threshold current to be performed.

In this chapter, such an analysis is performed for a parallel grating DFB-OSL, to yield initial data on the optimum device geometries.

6.2 Phenomenological Gain Model of an OSL

In the standard phenomenological model of a semiconductor laser [2], a linear relationship between gain and carrier density is assumed, with the local gain coefficient, g, being defined as;

$$g = A_0(n - n_0) \tag{6.1}$$

where n is the density of charge carriers, n_0 represents the carrier density required to reach transparency and A_0 is the gain coefficient.

As mentioned previously, in an operational laser, the gain must overcome

losses in the resonant cavity, so that;

$$\Gamma g_{th} = \alpha_{cl} + \alpha_m \tag{6.2}$$

Where Γ is the transverse optical confinement to the active region, α_{cl} represents the resonant cavity losses and α_m is the sum of other losses experienced by the optical mode.

For an Alq_3:DCM laser, it is expected that the optical absorption of the mixture will be dominated by the absorption of Alq_3 at the DCM emission wavelength of 632nm. From [10] the optical absorption of Alq_3 at 630nm is taken to be negligible, hence n_0 can be assumed to be zero. α_m mainly represents losses due to scattering of light from impurities and defects in the bulk material and from facets formed by imperfections at the layer boundaries. Such losses are not expected to be important and are difficult to quantify theoretically. Losses not due to re-absorption or resonant cavity effects are therefore omitted from the present analysis.

Because electrons (and holes) are bound to individual molecules in Organic Semiconductors, transportation of charge may be thought of as a result of the motion of neutrally charged excitons. The phenomenological gain model may therefore be applied to the case of organic materials if the the density of excitons in the device is taken as the charge carrier density. Combining equations (6.1) and (6.2) gives the following simple expression relating the carrier (exciton) density to the cavity losses:

$$\frac{\alpha'_{cl}}{\Gamma} = A_0 \frac{n_{th}}{d} \tag{6.3}$$

Where n_{th} is the carrier density at threshold and d is the thickness of the active region.

Optical confinement in the transverse plane Γ may be obtained by the waveguide analysis of Chapter 2. The cavity losses at threshold, α'_{cl} are found as the result of the threshold gain analysis of a DFB laser, described in Chapter 4.

6.3 Threshold current analysis of an OSL

In an optically pumped OSL, each pump photon absorbed in the Alq$_3$:DCM layer gives rise to a local excitation (exciton) consisting of an associated electron/hole pair, in an Alq$_3$ ligand. Neglecting the possibility of delocalisation of the electrons/holes from the ligand, the density of excitons in the active layer is therefore equivalent to the density of photons absorbed. In [20], an approximate expression is given relating the exciton density to an injection current density. This can be used to provide an estimated current threshold:

$$j_{th} = \frac{2n_{th}e}{\psi\tau} \tag{6.4}$$

Where n_{th} is the density of excitons, the carrier density introduced in the previous equations, e is the electronic charge (with a factor of two to account for the charge pair needed to form an exciton), $\psi = 1/4$ is the ratio of excitons capable of radiative transitions to the total number of excitons formed by electrical injection and $\tau = 5ns$ is the DCM radiative lifetime.

By inspection of equations (6.1-6.4), it is apparent that, if the gain coefficient relating local gain to exciton density in an organic material were to be

determined, static structural analysis of Alq_3:DCM lasers may be extended to include a threshold current calculation. The determination of injection current thresholds is a critical task in designing optimum cavity geometries.

Although no direct analysis of A_0 has been documented, measurements providing the exciton density in the active layer of an optically pumped Alq_3:DCM DFB laser have been performed in [20]. Furthermore the description of the device structure provided in [20] is sufficiently complete to allow a comparison between the experimental values of threshold exciton density and the theoretical values of threshold gain for an identical structure. Equation (6.2) may then be employed to provide an estimate for the gain coefficient, A_0, of an Alq_3:DCM laser operating at 630nm. Once found, the A_0 parameter is valid for any structure employing similar Alq_3:DCM formulations as a lasing material.

6.3.1 Obtaining the Gain Coefficient of Alq_3:DCM

The transverse layer structure of the DFB OSL device documented in [20] is shown in Figure 6.1. The OSL is optically pumped at $337nm$ over a $50\mu m$ wide and $2cm$ long stripe. Feedback is provided by a $200nm$ period DFB grating etched into the SiO_2 substrate prior to deposition of the organic films.

Measurements undertaken in [20] of the output pulse energy showed the onset of lasing to occur at surface pump energies of around $0.2\mu J/cm^2$. Assuming the photon distribution to be uniform through the transverse layer structure, the absorbed photon density is approximately $3x10^{11}cm^{-2}$. The

93
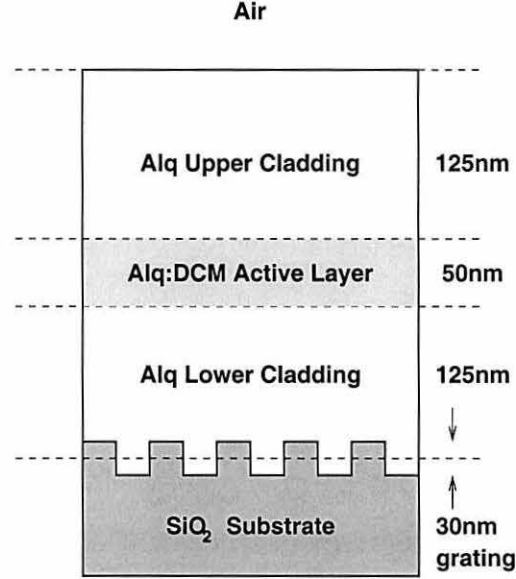
Figure 6.1: *Structure of the OSL DFB waveguide after reference [20]. The transverse composition of the OSL is shown.*

absorption of photons leads to an estimate of $n_{th} = 3\mathrm{x}10^{11}cm^{-2}$ excitons generated in the Alq$_3$:DCM active region.

Using the techniques detailed in the previous chapters, the lasing modes of an equivalent theoretical structure can be sought. The coupling coefficient, κ of the substrate grating is measured to be approximately $334cm^{-1}$, giving an exceptionally high κL product of around 668 for the $2cm$ long structure.

Figure 6.2. shows the locations of modes on a plot of gain and detuning for $\kappa L = 668$. Assuming that the majority of the excitation is initially coupled into the fundamental mode of the cavity, lasing should occur at $\alpha_{cl} = 1.12cm^{-1}$, with a detuning of around $0.004nm$. The confinement factor, Γ is then calculated numerically from the transverse field profile resulting
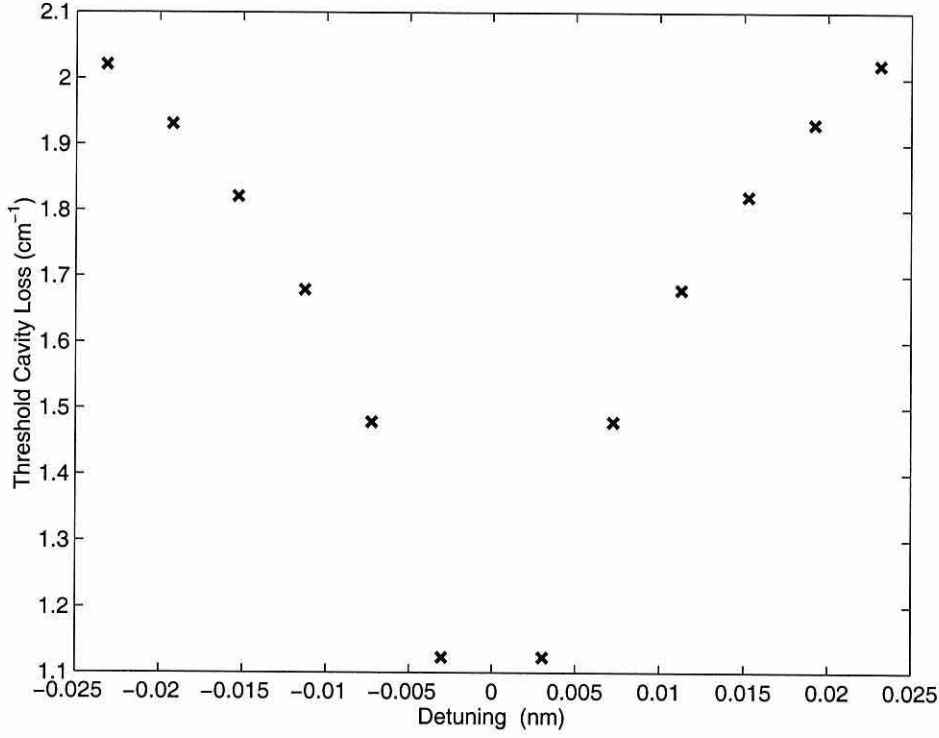
Figure 6.2: *Calculated longitudinal cavity mode spectra of the DFB OSL laser.*
The first order mode can be seen to commence lasing at low threshold gain
values ($\approx 1.1cm^{-1}$) by virtue of the 2cm long cavity length.

from the effective index method. For the equivalent OSL structure, Γ is
calculated to be around 19%. Using the calculated values of Γ and α_{cl}^{th}
with the measured value, n_{th}, in equation (6.2) gives an estimated value of
$A_0 = 1\text{x}10^{-18}cm^2$.

6.3.2 Optimisation of a DFB OSL

Figure 6.3 shows a threshold current density as a function of active region
thickness of the equivalent OSL for the fundamental lasing mode. It can
clearly be seen from the figure that the experimental layer thickness of $50nm$

95
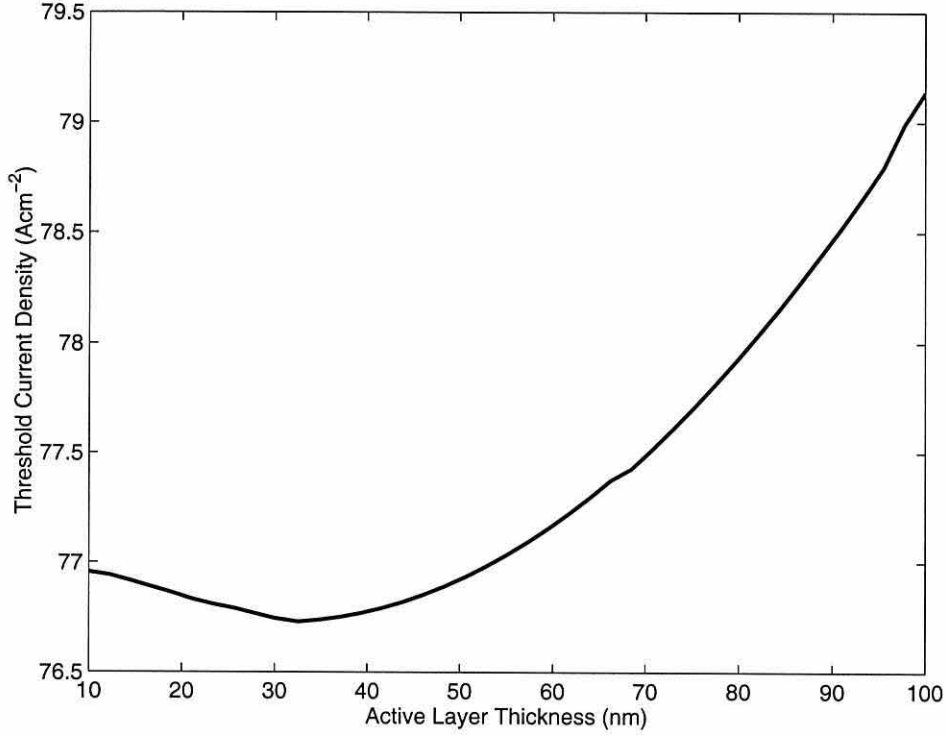
Figure 6.3: *Threshold current density optimisation curve for the active layer thickness of OSL DFB laser. The optimum width of the Alq_3:DCM layer lies around 30nm.*

lies close to the optimum value on the curve at $30nm$. With the $50nm$ active width reported in [11], the optimised current threshold is calculated by this method to be of order $77Acm^{-2}$.

Care must be taken during the analysis to account for the variations in the active layer by adjusting the widths of the upper and lower cladding regions to maintain a constant position in respect to the optical field profile (see Figure 6.4). Failure to do this results in the gain threshold being affected primarily by the coupling of the grating, thus eliminating the opportunity for optimisation of the active layer thickness.

A similar optimisation can be performed on the upper cladding region. Varying the thickness of this layer does not affect the grating coupling directly, but does alter the shape of the confined transverse mode significantly.
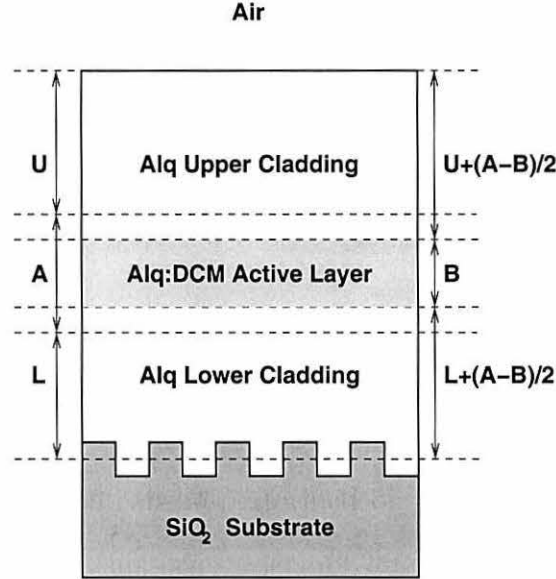
Figure 6.4: *Schematic diagram showing how the thickness of the cladding layers is adjusted to maintain the relative position of the active region in the structure during the optimisation (where A is the original thickness of the active region, B is the new thickness of the active region and U and L are the thicknesses of the upper and lower cladding respectively). This allows the separation of waveguide confinement and grating coupling effects on the threshold current density.*

The presence of the cladding avoids the reduction in active layer confinement seen when the active layer is interfaced directly to air. Beyond an optimum value, however, the cladding layer merely acts to broaden the mode

profile, weakening the overall confinement of the optical mode.
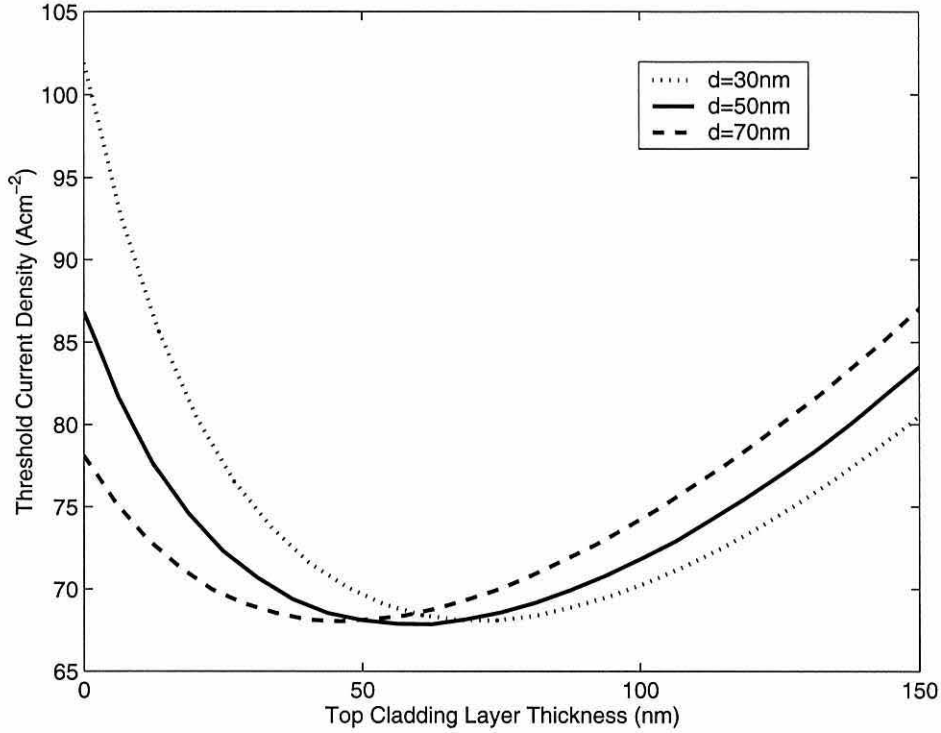
Figure 6.5: *Optimisation curve for the top cladding layer of OSL structures having varying active region thickness, d. Optimum values for the curves can be seen between thicknesses of 50 and 70 nm.*

Figure 6.5 shows the effect of varying the cladding thickness for DFB OSLs having active regions of 70, 50 and $30nm$. The apparent offset is due to the effect of changing the active region width on the thickness of the cladding layer, and the optimum value for the active layer thickness does not significantly alter in relation to the optical field profile. The optimum thickness of the top cladding layer for a $50nm$ active region is around 60nm, approximately half the thickness used in the experimental design.

Figure 6.6 shows the effect of varying the thickness of the lower cladding
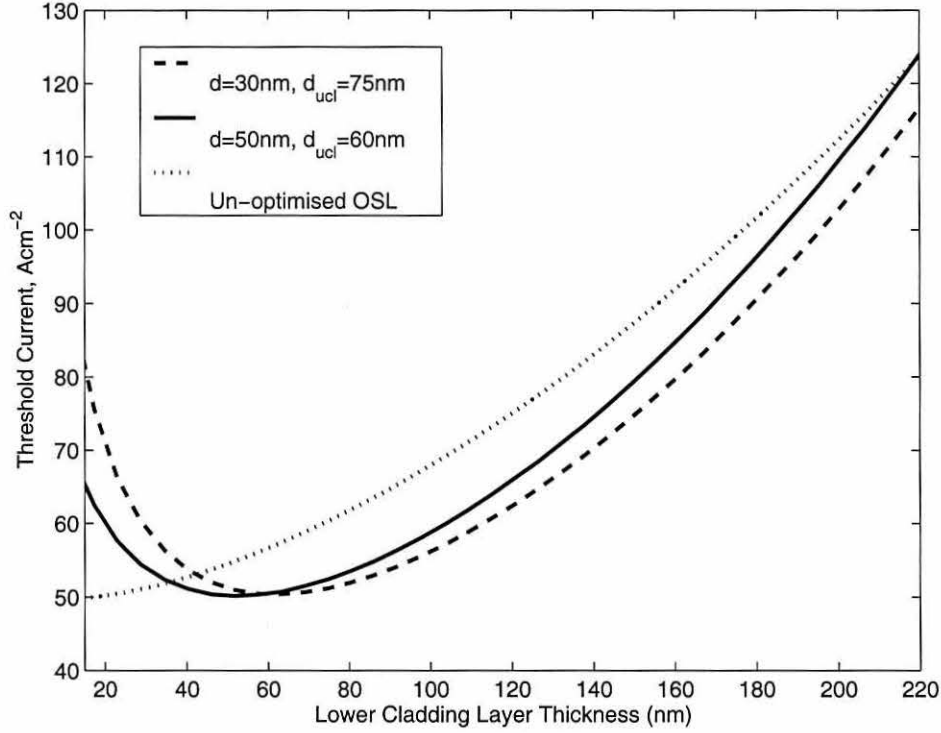
Figure 6.6: *Effect of varying the bottom cladding layer thickness of OSL structures having varying active region thicknesses, d and top cladding layer thicknesses d_{ucl}. An optimum for the lower cladding layer lies at a thickness of about 60nm for these structures.*

region for the original OSL [20], a structure having a 60nm thick top-cladding layer optimised for a $50nm$ active region and an OSL having a $75nm$ top cladding layer and a $30nm$ active region. For the published OSL, design, the threshold current is mostly affected by the grating coupling, and minimum threshold is achieved when the grating is as close as possible to the active region. With regard to the possibility of electrical pumping, however, it is highly beneficial to retain a lower Alq3 cladding layer to assist with charge transport across the device. For both of the structures having altered ge-

99

ometries, a lower cladding region of around 60nm gives the lowest current threshold density of around $50Acm^{-1}$.
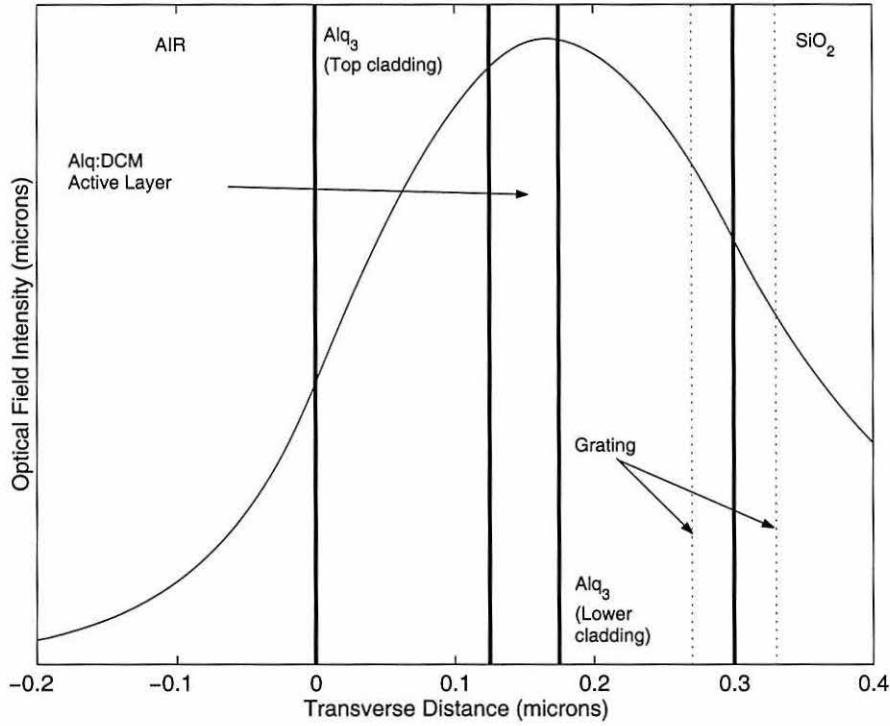
Figure 6.7: *Optical field profile for the single TE mode of the un-optimised DFB OSL. Shown for comparison, it can be seen that the grating region lies at a considerable distance from the optical field maximum.*

The effects of the optimisations on the optical field profile are shown in Figure 6.7 and Figure 6.8. Figure 6.7 shows the optical field of the un-optimised OSL for comparison with the optimised OSL field, shown in Figure 6.8. It can be seen from the two figures that the field peak of the optimised structure is shared more evenly between the active region and feed-back grating, thus affording optimum confinement to the active layer and feedback grating simultaneously. The new coupling coefficient provided by the grating
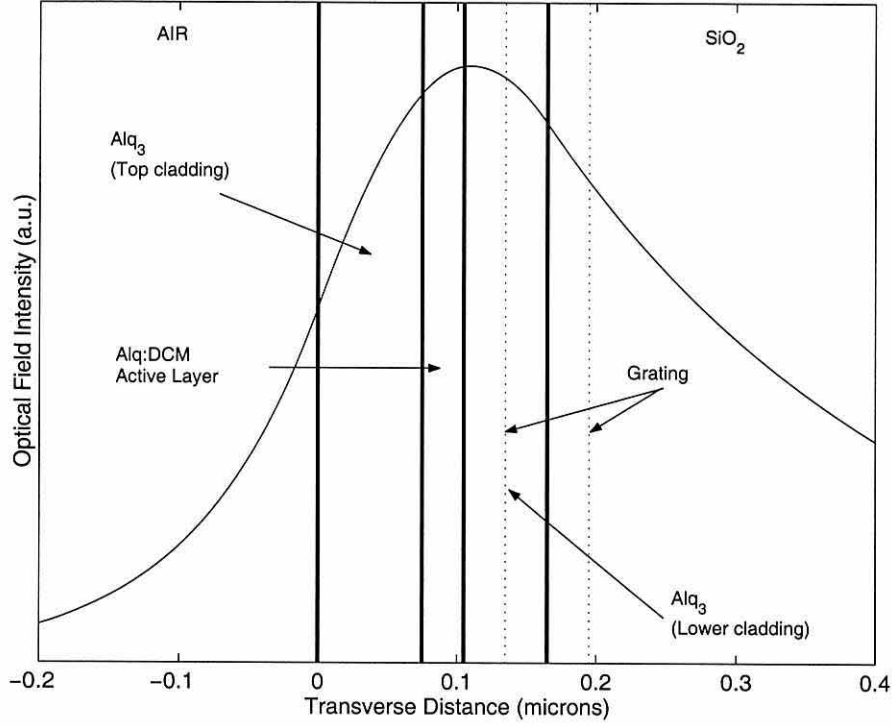
Figure 6.8: *Optical field profile for the single TE mode of the optimised DFB OSL having a 30nm thick active layer, a 75nm thick top cladding layer and a 60nm thick bottom cladding layer.*

was calculated to be $640cm^{-1}$, an improvement by a factor of two over the value of κ obtained for the un-optimised OSL.

The net effect of the optimisations described is to improve the threshold current density required to achieve laser action from $80Acm^{-2}$ found in [20] to the value of $50Acm^{-2}$ found here, a reduction of approximately 35%.

6.4 Discussion

It has been shown how the standard analysis technique of current threshold optimisation may be adapted to improve the design of Organic Semiconductor Lasers. An improvement of 35% has been seen in the current threshold and carrier density required for lasing in the OSL design investigated. It is likely that this is the optimum value obtainable from this device design. Although the optical confinement to the active region was reduced, the necessity for high coupling coefficients via the feed-back grating was improved by over 50%, high enough to overcome the optical mode losses and provide the overall reduction in threshold. This illustrates the point that, in OSL lasers employing distributed feed-back, effective grating positioning in the transverse structure is frequently of greater importance than high optical mode confinement.

Adopting the widely used phenomenological gain model of in-organic semiconductor laser design [2] provides an estimate for the gain/current relationship within organic materials. It is appreciated that the estimate of the current density as a function of carrier density, equation (6.4), is very approximate. However, although the magnitude of current density may be inaccurate, provided there is an approximately linear relationship between the number of excitons and the injected current, the changes in device geometry indicated in the optimisation will provide the same degree of overall improvement for the threshold current density.

The estimated value for the gain coefficient, A_0, in the analysis is appropriate for Alq$_3$:DCM OSLs operating at wavelengths of around 630nm. It

is therefore possible to use this value for analysis of a number of Alq_3:DCM OSL configurations subject to a more accurate value being determined experimentally. Furthermore, given similar experimental data regarding the pump power density at threshold, it is to be expected that the gain coefficient of lasers consisting of other organic materials can be estimated in a similar manner. Polymer materials in particular are an attractive alternative to low molecular weight organic semiconductors and sufficient data regarding their optical and electroluminescent properties is becoming available [21],[22].

Chapter 7

Analysis of Circular Grating DFB-OSLs

7.1 Introduction

It has been shown that using Distributed Feed-Back (DFB) designs for the manufacture of Organic Semiconductor Lasers (OSLs) offers considerable advantages in terms of the lowering the threshold gain. Specifically, DFB lasers made with gratings consisting of linear grooves, cut parallel to each other have been discussed. The use of organic materials and soft lithographic fabrication processes allow a wider scope of designs to be considered, however, including circularly symmetric gratings. The analysis of circularly symmetric lasers, known as Circular Grating, Distributed Feed-Back (CG-DFB) lasers, is the subject of this chapter.

For the analysis of CG-DFB lasers, it is convenient to adopt a cylindrical coordinate system, having radial (r), azimuthal (θ) and axial (z) components. A CG-DFB laser consists of a series of circular, concentric grooves (Figure 7.1) forming a periodic index perturbation dependent upon the radial coordinate, r.

In a similar manner to the linear grating, the circularly symmetric perturbation confines the emitted light of the laser in the radial direction. The circular grating therefore has the added advantage of confining the light simultaneously to the entire plane of the device, whilst confinement in the axial direction is achieved by the planar structure of the device.
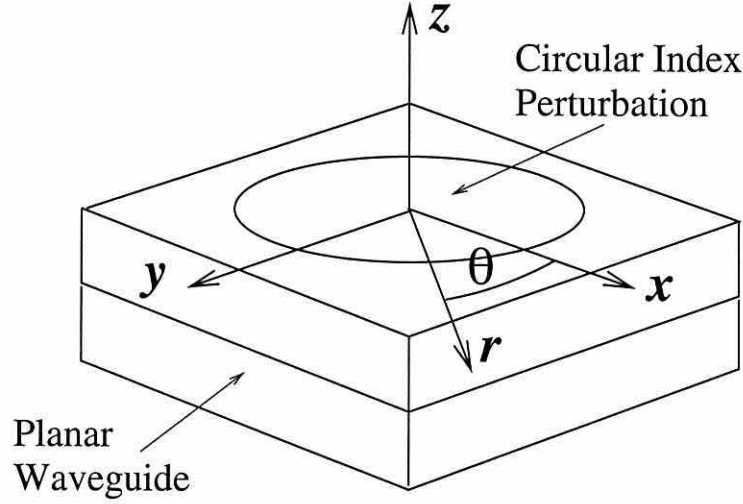
Figure 7.1: *A simple three layer planar waveguide with a circular index per-turbation. The cylindrical coordinate system adopted is shown.*

7.2 Coupled mode analysis of CG-DFB structures

7.2.1 Cylindrical waves in a planar waveguide

Attention is given to the dielectric waveguide of Figure (7.1). Given that the Laplacian operator in cylindrical coordinates is:

$$\nabla = \frac{\partial}{\partial r} + \frac{1}{r}\frac{\partial}{\partial \theta} + \frac{\partial}{\partial z} \tag{7.1}$$

Maxwells curl equations can be expanded to:

$$E_r = \frac{j}{\omega\epsilon}(\frac{1}{r}\frac{\partial}{\partial \theta}H_z - \frac{\partial}{\partial z}H_r) \tag{7.2}$$

$$E_\theta = \frac{j}{\omega\epsilon}(\frac{\partial}{\partial r}H_z - \frac{\partial}{\partial z}H_r) \tag{7.3}$$

$$E_z = \frac{j}{\omega\epsilon}(\frac{\partial}{\partial r}H_\theta - \frac{1}{r}\frac{\partial}{\partial \theta}H_r) \tag{7.4}$$

106

$$H_r = \frac{j}{\omega\mu}\left(\frac{\partial}{\partial z}E_r - \frac{1}{r}\frac{\partial}{\partial \theta}E_z\right) \tag{7.5}$$

$$H_\theta = \frac{j}{\omega\mu}\left(\frac{\partial}{\partial z}E_r - \frac{\partial}{\partial r}E_z\right) \tag{7.6}$$

$$H_z = \frac{j}{\omega\mu}\left(\frac{1}{r}\frac{\partial}{\partial \theta}E_r - \frac{\partial}{\partial r}E_\theta\right) \tag{7.7}$$

A time dependence of $e^{j\omega t}$ is implicit in (7.2-7.7). The four radial (r) and azimuthal (θ) field components can be obtained provided the transverse components E_z and H_z are known;

$$E_r = \frac{1}{\beta^2}\left(\frac{\partial^2}{\partial r \partial z}E_z - j\frac{\mu\omega}{r}\frac{\partial}{\partial \theta}H_z\right) \tag{7.8}$$

$$E_\theta = \frac{1}{\beta^2}\left(\frac{1}{r}\frac{\partial^2}{\partial \theta \partial z}E_z + j\mu\omega\frac{\partial}{\partial r}H_z\right) \tag{7.9}$$

$$H_r = \frac{1}{\beta^2}\left(j\frac{\omega\epsilon}{r}\frac{\partial}{\partial \theta}E_z + \frac{\partial^2}{\partial r \partial z}H_z\right) \tag{7.10}$$

$$H_\theta = \frac{1}{\beta^2}\left(-j\omega\epsilon\frac{\partial}{\partial r}E_z + \frac{1}{r}\frac{\partial^2}{\partial \theta \partial z}H_z\right) \tag{7.11}$$

where β is a constant to be determined. The reduction to two independent variables, E_z and H_z, is a feature of Maxwells equations in cylindrical coordinates, and is often utilised in the analysis of cylindrical waveguides such as optical fibres [1].

From the analysis in Section 2.2, it is known that there are two kinds of mode supported by a planar waveguide; Transverse Electric (TE) and Transverse Magnetic (TM) modes. The TE and TM waves are characterised by $E_z = 0$ and $H_z = 0$ respectively. So that, for the TE waves;

$$E_r = -\frac{j\omega\mu_o}{\beta^2}\frac{1}{r}\frac{\partial}{\partial \theta}H_z \tag{7.12}$$

107

$$E_\theta = \frac{j\omega\mu_o}{\beta^2}\frac{\partial}{\partial r}H_z \qquad (7.13)$$

$$H_r = \frac{1}{\beta^2}\frac{\partial^2}{\partial r\partial z}H_z \qquad (7.14)$$

$$H_\theta = \frac{1}{\beta^2}\frac{1}{r}\frac{\partial^2}{\partial\theta\partial z}H_z \qquad (7.15)$$

The TE modes of the planar waveguide having a z dependent refractive index, $n(z)$, may therefore be found as solutions to the scalar wave equation;

$$\nabla^2\psi(r,\theta,z) + k_0^2 n^2\psi(r,\theta,z) = 0 \qquad (7.16)$$

with $\psi(r,\theta,z) = H_z(r,\theta,z)$, and:

$$\nabla^2 = \frac{1}{r}\frac{\partial}{\partial r}(r\frac{\partial}{\partial r}) + \frac{1}{r^2}\frac{\partial^2}{\partial\theta^2} + \frac{\partial^2}{\partial z^2} \qquad (7.17)$$

The solutions to (7.16) thus take the form:

$$\psi(r,\theta,z) = R(r)Z(z)\Theta(\theta) \qquad (7.18)$$

Substitution of (7.18) into (7.16) and performing a separation of variables leads to;

$$\frac{\partial^2}{\partial z^2}Z(z) + (k_0^2\epsilon_r - \beta^2)Z(z) = 0 \qquad (7.19)$$

$$\frac{\partial^2}{\partial\theta^2}\Theta(\theta) + l^2 - \Theta(\theta) = 0 \qquad (7.20)$$

$$r\frac{\partial}{\partial r}(r\frac{\partial}{\partial r}R(r)) + (\beta^2 r^2 - l^2)R(r) = 0 \qquad (7.21)$$

where β and l are the constants of separation. (7.19) therefore defines the transverse modes of the slab waveguide, with β as the propagation constant of the modes. It was seen in previous chapters that a mono-mode planar waveguide is more commonly required in low-threshold DFB lasers. The analysis of lasers supporting only a single mode in the z direction also simplifies the coupling equations considerably, therefore it is useful to assume that there is a single solution to (7.19). (7.20) describes the azimuthal modes, which must be periodic such that $\Theta(\theta + 2\pi) = \Theta(\theta)$. A solution for the azimuthal modes is therefore:

$$\Theta(\theta) = e^{jn\theta} \tag{7.22}$$

$n = 1, 2, 3...$ etc. and is the integer order of the cylindrical waves. (7.21) is recognised as Bessel's equation describing the radial propagation of cylindrical waves. Solutions to (7.21) therefore take the form of Hankel functions of the first and second kind for the inward and outward propagating waves respectively. If $\beta r >> 1$ the large argument approximation for the Hankel functions applies, and the solutions for the lth azimuthal mode take the form:

$$R(\beta r) = H_l^{(1)} \approx \sqrt{\frac{2}{\pi \beta r}} e^{j(\beta r - l\pi/2 - n - \pi/4)} \tag{7.23}$$

$$R(\beta r) = H_l^{(2)} \approx \sqrt{\frac{2}{\pi \beta r}} e^{-j(\beta r - l\pi/2 - n - \pi/4)} \tag{7.24}$$

Substituting (7.23), (7.24) and (7.22) into (7.18) and assuming a single mode solution to the planar wave equation gives the general solution;

109

$$\Psi_l^{(p)\sigma}(r,\theta,z) = A_l^{(p)\sigma} R_l^{(p)}(\beta^\sigma r) Z^\sigma(z) e^{jn\theta} \qquad (7.25)$$

where $A_l^{(p)\sigma}$ is a normalisation constant, p is the propagation sign (positive for outward travelling wave, negative for inward travelling waves) and σ is the polarisation, so that $\sigma = TE$ or $\sigma = TM$, thus allowing coupling between modes of differing polarisations to be accounted for. Substituting (7.25) into (7.12-7.15) and recalling that the wavefunction is defined as $\psi = H_z$, the field distribution of the TE field may be written:

$$E_{lz}^{(p)TE} = 0 \qquad (7.26)$$

$$H_{lz}^{(p)TE} = A_l^{(p)TE} R_l^{(p)}(\beta^{TE} r) Z^{TE}(z) e^{jl\theta} \qquad (7.27)$$

$$E_{lr}^{(p)TE} = A_l^{(p)TE} \frac{l\omega\mu_0}{(\beta^{TE})^2} \frac{1}{r} R_l^{(p)}(\beta^{TE} r) Z^{TE}(z) e^{jl\theta} \qquad (7.28)$$

$$E_{l\theta}^{(p)TE} = A_l^{(p)TE} \frac{j\omega\mu_0}{(\beta^{TE})^2} [\frac{d}{dr} R_l^{(p)}(\beta^{TE} r)] Z^{TE}(z) e^{jl\theta} \qquad (7.29)$$

$$H_{lr}^{(p)TE} = A_l^{(p)TE} \frac{1}{(\beta^{TE})^2} [\frac{d}{dr} R_l^{(p)}(\beta^{TE} r)][\frac{d}{dz} Z^{TE}(z)] e^{jl\theta} \qquad (7.30)$$

$$H_{l\theta}^{(p)TE} = A_l^{(p)TE} \frac{jl}{(\beta^{TE})^2} \frac{1}{r} R_l^{(p)}(\beta^{TE} r)[\frac{d}{dz} Z^{TE}(z)] e^{jl\theta} \qquad (7.31)$$

Using (7.26-7.31) it can be shown that;

$$\left|\frac{E_{lr}^{(p)TE}}{E_{l\theta}^{(p)TE}}\right| = (\frac{l}{\beta^{TE} r} |\frac{R_l^p(\beta^{TE} r)}{R_l^{p'}(\beta^{TE} r)}|) \qquad (7.32)$$

110

(7.32) indicates that the radially dependent component $E_{lr}^{(p)TE}$ is nonzero for all values of l except $l = 0$. As there is no radial component of the electric field in the definition of a TE wave, only the zeroth order cylindrical TE wave resembles the equivalent slab mode. At higher values of the radial coordinate r, the ratio of (7.32) becomes much smaller, and tends to zero in the limit as $r \to \infty$. This can be interpreted in physical terms as the tendency of the curvature of the cylindrical coordinate system to reduce at higher radii. It will be revealed subsequently that the coupling of fields by the circularly symmetric grating comes to resemble closely the coupling in parallel gratings when r is assumed to be large.

7.2.2 Excitation of Cylindrical Waves

To analyse the coupling effect of a grating on the waves, it is useful to consider the case where the modes supported by the structure are excited by sources. Following the line of reasoning in [23], the source of excitation of the modes is represented by an induced polarisation, $\mathbf{P}(r, \theta, z)$. Maxwells equations are then:

$$\nabla \times \mathbf{E} = -j\mu\omega\mathbf{H} \qquad (7.33)$$

$$\nabla \times \mathbf{H} = j\omega\epsilon\mathbf{E} + \mathbf{P}j\omega \qquad (7.34)$$

Two such induced polarisations, $\mathbf{P}_1$ and $\mathbf{P}_2$, thus drive two separate fields $\mathbf{E}_1$ and $\mathbf{E}_2$.

It is possible to verify using (7.33) and (7.34) that:

111

$$\nabla \cdot (\mathbf{E}_1 \times \mathbf{H}_2^* + \mathbf{E}_2^* \times \mathbf{H_1}) = -j\omega \mathbf{P}_1 \cdot \mathbf{E}_2^* + j\omega \mathbf{P}_2^* \cdot \mathbf{E}_1 \qquad (7.35)$$

As there will be only one 'source' (the grating), $\mathbf{P_2}$ may be set to zero, so that the coupling between the waves may be studied. Integrating (7.35) over a cylindrical surface of radius r, the following expression is derived consisting of a driving term containing $\mathbf{P_1}$ and the transverse field components of the magnetic and electric fields:

$$\int_0^{2\pi} \int_{-\infty}^{\infty} \frac{\partial}{\partial r}[r(\mathbf{E}_{1t} + \mathbf{H}_{2t}^* + \mathbf{E}_{2t}^* + \mathbf{H}_{1t}) \cdot \hat{r}]d\theta dz = -j\omega \int_0^{2\pi} \int_{-\infty}^{\infty} r(\mathbf{P_1} \cdot \mathbf{E_2})d\theta dz$$
$$(7.36)$$

The subscript, t, in (7.36) denotes the cylindrical (θ, z) components of the fields. Expanding field 1 gives;

$$\mathbf{E}_{1t}(r, \theta, z) = \sum_{q\tau m} a_m^{(q)\tau}(r)\mathbf{E}_{mt}^{(q)\tau}(r, \theta, z) \qquad (7.37)$$

$$\mathbf{H}_{1t}(r, \theta, z) = \sum_{q\tau m} a_m^{(q)\tau}(r)\mathbf{H}_{mt}^{(q)\tau}(r, \theta, z) \qquad (7.38)$$

where $q = +\text{or}-$ is the direction of propagation, $\tau = TE$ or TM is the polarity of the field and m is the cylindrical order of wave 1. Let field 2 be one of the infinite number of cylindrical waves;

$$\mathbf{E}_{2t}(r, \theta, z) = \mathbf{E}_{lt}^{(p)\sigma}(r, \theta, z) \qquad (7.39)$$

$$\mathbf{H}_{2t}(r, \theta, z) = \mathbf{H}_{lt}^{(p)\sigma}(r, \theta, z) \qquad (7.40)$$

$p = +$ or $-$ is defined as the propagation direction, $\sigma = TE$ or TM and l is the cylindrical mode number of wave 2. Substitution of (7.39) and (7.40) into (7.36) leads, after manipulation, to;

$$p\frac{\partial}{\partial r}a_l^{(p)\sigma}(r) = -j\omega \int_0^{2\pi}\int_{-\infty}^{\infty} r[\mathbf{P}_1 \cdot \mathbf{E}_l^{(p)\sigma*}(r,\theta,z)]d\theta dz \qquad (7.41)$$

where use is made of the orthogonality relations given in [23];

$$\int_0^{2\pi}\int_{-\infty}^{\infty} r(\hat{r} \cdot [\mathbf{E}_{mt}^{(q)\tau} \times \mathbf{H}_{lt}^{(p)\sigma*} + \mathbf{E}_{lt}^{(p)\sigma*} \times \mathbf{H}_{mt}^{(q)\tau}])d\theta dz = pQ \qquad (7.42)$$

With Q a constant defined in [23] as the product of the Kronecker deltas describing the coupling between waves of different wave number, polarisation and direction. It can be seen from (7.41) that, as is to be expected, there is no change in the amplitude of the cylindrical waves when $\mathbf{P}_1 = 0$, which represents the case of no sources being present.

7.2.3 Cylindrical Refractive index Perturbation

To assess the effect of a circular DFB grating imposed on the waveguide, the induced polarisation is assumed to be the result of a circular refractive index perturbation:

$$\mathbf{P}_1 = \epsilon_0 \Delta\epsilon(r,z)\mathbf{E}_1 \qquad (7.43)$$

It can be easily proved by consideration of Maxwells equations that the radial component $\mathbf{E}_{1r}$ of the field can be expressed using the cylindrical (θ, z) components:

113

$$\mathbf{E}_{1r} = \frac{1}{j\omega\epsilon_0[\epsilon_r + \Delta\epsilon(r,z)]}[\nabla_t \times \mathbf{H}_1 t - \frac{\mathbf{H}_{1\theta}}{r}\hat{z}] \tag{7.44}$$

Making use of (7.38) and Maxwells equations then leads to:

$$\mathbf{E}_{1r} = \frac{\epsilon_r}{\epsilon_r + \Delta\epsilon(r,z)} \sum_{q\tau m} a_m^{(q)\tau}(r)\mathbf{E}_{mr}^{(q)\tau} \tag{7.45}$$

Combining (7.45) and (7.37) to give the field $\mathbf{E}_1(\mathbf{r},\theta,\mathbf{z})$ and substituting into (7.43) gives:

$$\mathbf{P}_1 = \epsilon_0\Delta\epsilon(r,z) \sum_{q\tau m} a_m^{(q)\tau}(r)[\mathbf{E}_{mt}^{(q)\tau} + \frac{\epsilon_r}{\epsilon_r + \Delta\epsilon}\mathbf{E}_{mr}^{(q)\tau}] \tag{7.46}$$

(7.41) and (7.46) then combine to give the general coupling equation;

$$p\frac{\partial}{\partial r}a_l^{(p)\sigma} = -j \sum_{q\tau m} \kappa_{l,m}^{(p)\sigma,(q)\tau} a_m^{(q)\tau}(r) \tag{7.47}$$

where $\kappa_{l,m}$ are the coupling coefficients given by;

$$\kappa_{l,m}^{(p)\sigma,(q)\tau} = \omega\epsilon_0 \int_0^{2\pi} \int_{-\infty}^{\infty} r\Delta\epsilon(r,z)[\mathbf{E}_{mt}^{(q)\tau}\cdot\mathbf{E}_{lt}^{(p)\sigma*} + \frac{\epsilon_r}{\epsilon_r + \Delta\epsilon(r,z)}\mathbf{E}_{mr}^{(q)\tau}\cdot\mathbf{E}_{lr}^{(p)\sigma*}]d\theta dz \tag{7.48}$$

Equations (7.47) and (7.48) can therefore be used to analyse a wide variety of mode couplings in the circular grating.

7.2.4 TE-TE coupling in a CG-DFB grating

By substitution of the field distributions (7.26-7.30) into (7.48), the coefficients for coupling between TE modes can be shown to be the product of a

114

Kronecker delta and the coupling coefficient for fields of the same cylindrical wave order:

$$\kappa_{m,l}^{(p)TE(q)TE} = \delta_{lm}\kappa_l^{(p,q)TE,TE} \tag{7.49}$$

δ_{nm} is given by;

$$\delta_{lm} = \frac{1}{2\pi}\int_0^{2\pi} e^{j(m-l)\theta}d\theta \tag{7.50}$$

and the coupling coefficient between modes of the same order, $\kappa_l^{(p,q)TE,TE}$ is defined as;

$$\kappa_l^{(p,q)TE,TE} = 2\pi r|A_l^{(q)TE}|^2\frac{\omega\mu_0}{(\beta^{TE})^4}\int_{-\infty}^{\infty}\{\Delta\epsilon(r,z)|Z^{TE}(z)|^2[\frac{d^2}{dr^2}R_l^{(q)TE}(\beta^{TE}r)] +$$
$$+ \frac{\epsilon_r}{\epsilon_r+\delta\epsilon(r,z)}(\frac{l}{r})^2|R_l^{(q)TE}(\beta^{TE}r)|^2\}dz \tag{7.51}$$

By writing down the field distributions for the TM field in a similar manner to the TE field of (7.26-7.30), and substituting into (7.48) it can be seen that, in general;

$$\kappa_{m,l}^{(p)\sigma(q)\tau} = \delta_{lm}\kappa_l^{(p,q)\sigma,\tau} \tag{7.52}$$

The coupling coefficients for TE-TM and TM-TM coupling can also be derived in a similar manner to (7.51). Substituting (7.52) into (7.47) results in the following coupling equations describing mode coupling between the TE and TM fields;

$$\frac{d}{dr}a_l^{+,TE} = -j[\kappa_l^{(+,+)TE,TE}a_l^{(+)TE} + \kappa_l^{(+,-)TE,TE}a_l^{(-)TE} +$$

115

$$+ \kappa_l^{(+,+)TE,TM} a_l^{(+)TM} + \kappa_l^{(+,-)TE,TM} a_l^{(-)TM}] \qquad (7.53)$$

$$\frac{d}{dr} a_l^{-,TE} = -j[\kappa_l^{(+,+)TE,TE} a_l^{(+)TE} + \kappa_l^{(-,-)TE,TE} a_l^{(-)TE} +$$

$$+ \kappa_l^{(-,+)TE,TM} a_l^{(+)TM} + \kappa_l^{(-,-)TE,TM} a_l^{(-)TM}] \qquad (7.54)$$

It is evident from inspection of (7.53) and (7.54) that only cylindrical waves of the same order are coupled in a circularly symmetric grating. The coupling of TE to TM modes is dissimilar to mode coupling in parallel DFBs, where there is no cross coupling between modes of different polarisation. Interestingly, by consideration of the coupling coefficients for the TE-TM coupling, it can be seen that cross polarisation coupling of zeroth order modes (where $m = l = 0$) gives $\kappa_{l,m}^{(p,q)TE,TM} = 0$, and the cross coupling terms vanish. Even for non-zero mode orders can also be proven [24] that inter polarisation terms become negligible under the large radius approximation, $(\beta r >> 1)$ and the coupled wave equations describing TE-TE coupling then reduce to;

$$\frac{d}{dr} a_l^+ = -j\kappa(r)[a_l^+(r) + j(-1)^l e^{j2\beta r} a_l^-(r)] \qquad (7.55)$$

$$\frac{d}{dr} a_l^- = j\kappa(r)[-j(-1)^l e^{-j2\beta r} a_l^+(r) + a_l^-(r)] \qquad (7.56)$$

With the coupling coefficient, $\kappa(r)$, being defined as:

$$\kappa(r) = \frac{k_0^2}{2\beta C} \int_{-\infty}^{\infty} \Delta\epsilon(r,z)|Z(z)|^2 dz \qquad (7.57)$$

where C is the normalisation constant given by;

116

$$C = \int_{-\infty}^{\infty} |Z(z)|^2 dz \qquad (7.58)$$

7.3 Modes of a CG-DFB laser

Consideration is given to the CG-DFB laser of Figure 7.2.
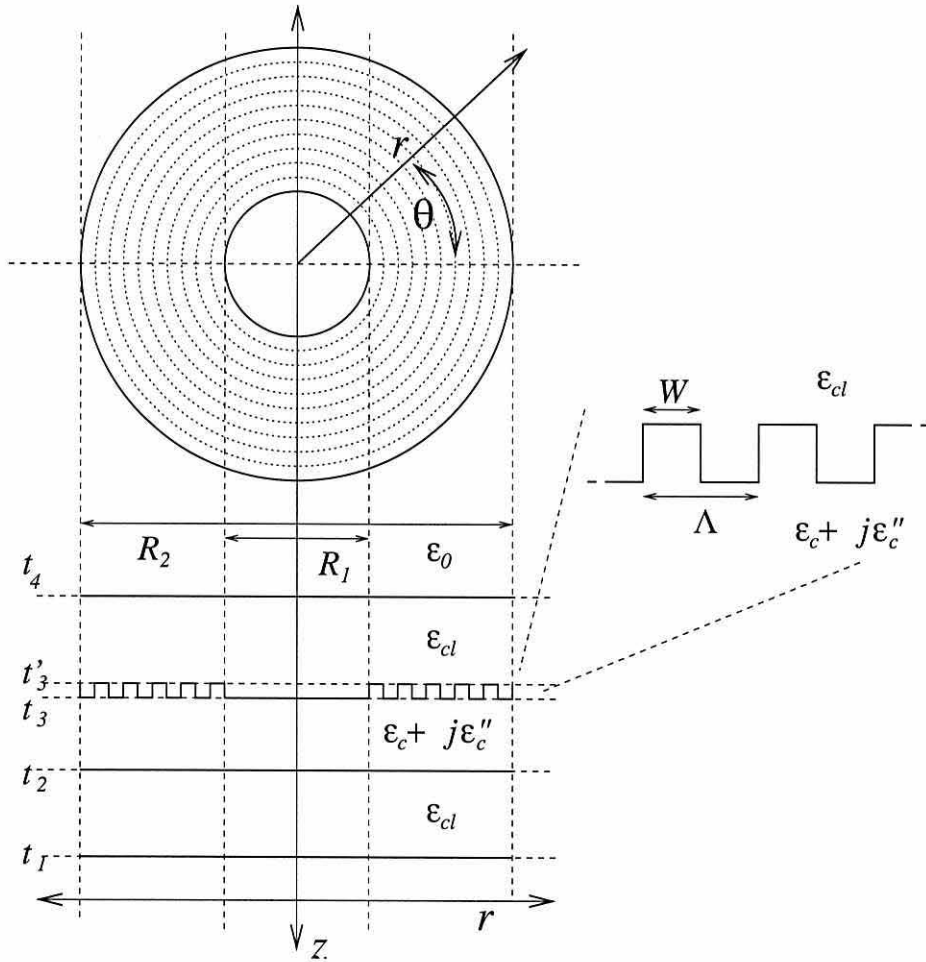
Figure 7.2: *CG-DFB Laser Structure, shown in plan and section. The grating wavelength (Λ) and tooth-width (W) are shown in the insert.*

The structure is composed of a multilayered slab waveguide with a circularly

symmetric refractive index perturbation of radius R_2, formed by concentrically arranged channels in the surface of the top layer of the device. The channels forming the perturbation are chosen to have a rectangular profile. A small, unperturbed central section is included, which may avoid fabrication problems as the radius of the grooves tends to zero. The active region of the laser is taken to include both the unperturbed centre section as well as the grating, consistent with optical pumping of the device.

7.3.1   Dielectric Perturbation of the CG-DFB Laser

The dielectric constant in the unperturbed centre section is;

$$
\epsilon(z,r) = \begin{cases}
\epsilon_{cl} & (t_1 > z < t_2) \\
\epsilon_c + j\epsilon_c'' & (t_2 < z < t_3) \\
\epsilon_{cl} & (t_3 < z < t_4) \\
\epsilon_0 & (t_4 < z)
\end{cases}
\tag{7.59}
$$

The imaginary part of the complex permittivity over the active layer may be included as an index perturbation, so that;

$$
\Delta\epsilon = j\epsilon_c'' \tag{7.60}
$$

7.3.2   Coupling Coefficients in the CG-DFB laser

By substitution for $\Delta\epsilon$ into (7.57), the coupling coefficient for $(0 < r < R_1)$ is therefore;

$$
\kappa(r) = j\alpha \tag{7.61}
$$

118

where;

$$\alpha = \frac{k_0^2}{2\beta}\epsilon_c''\Gamma_c \qquad (7.62)$$

Γ_c is thus the confinement of the light to the active region of the transverse planar waveguide, obtained by solving the planar waveguide problem in the manner discussed in Chapter 2 .

For the circularly symmetric perturbation ($R_1 > r > R_2$), the dielectric constant takes the form;

$$\epsilon(z,r) = \begin{cases} \epsilon_{cl} & (z < t_1) \\ \epsilon_c + j\epsilon_c'' & (t_1 < z < t_2) \\ \epsilon_{cl} & (t_2 < z < t_3) \\ \epsilon_g(z,r) & (t_3 < z < t_3') \\ \epsilon_0 & (t_3 < z < t_4) \end{cases} \qquad (7.63)$$

where the dielectric perturbation of the grating may be expressed as a Fourier series:

$$\epsilon_g(z,r) = \sum_{m=-\infty}^{\infty} \epsilon_{gm}(z)e^{j(2\pi/\Lambda)m(r-R_1)} \qquad (7.64)$$

with m the grating diffraction order, and where, for non-zero grating orders:

$$\epsilon_{gl} = -\frac{(\epsilon_c l - \epsilon_c)}{\pi l}e^{j(\pi/\Lambda)lW)} \qquad (7.65)$$

Substitution of (7.64) and (7.65) into (7.57) leads to the following expression for the coupling of the grating for ($R_1 > r > R_2$);

$$\kappa(r) = j\alpha - \sum_{l \neq 1}\kappa_m e^{-j(\Omega_l - (2\pi/\Lambda)l r} \qquad (7.66)$$

119

where

$$\Omega_l = \frac{\pi}{\Lambda} l (W_1 + 2R_1) \tag{7.67}$$

represents the change in phase of the coupled wave due to the centre section. κ_m in equation (7.66) is calculated numerically from the planar waveguide field profile in an identical manner to the coupling coefficient of a one-dimensional perturbed waveguide, which was discussed in Section 4.1.

7.3.3 Transfer Matrices for the CG-DFB Sections

Similar to the analysis in [25], transfer matrix techniques may be used to analyse structures having more than one section. For the unperturbed central region, (7.61) can be substituted into (7.55) and (7.56) to give;

$$\begin{bmatrix} a_l^{+'}(r) \\ a_l^{-'}(r) \end{bmatrix} = \begin{bmatrix} e^{\alpha r} & 0 \\ 0 & e^{-\alpha r} \end{bmatrix} \begin{bmatrix} a_l^{+'}(0) \\ a_l^{-'}(0) \end{bmatrix} \tag{7.68}$$

where $a_l^{+,-'}(r)$ is the amplitude of the cylindrical wave in the unperturbed region. Over the grating radius ($R_1 > r > R_2$), substitution of (7.66) into (7.55) may be performed. After neglecting non-resonant and fast oscillating terms from the resulting expression, as is performed in the standard Coupled Mode Theory (CMT) analysis of parallel gratings, (7.56) leads to:

$$\frac{d}{dr} a_l^+ = \alpha a_l^+ - (-1)^l \kappa_m e^{j\Omega m} e^{j2\Delta\beta r} a_n^-(r) \tag{7.69}$$

$$\frac{d}{dr} a_l^- = -(-1)^l \kappa_m e^{-j\Omega m} e^{-j2\Delta\beta r} a_n^+(r) - \alpha a_n^-(r) \tag{7.70}$$

120

β is defined as the propagation constant of the mode supported by the planar waveguide and $\Delta\beta$ represents the detuning from the Bragg frequency of the mode, so that $\Delta\beta = \beta - m\pi/\Lambda$. The solution of (7.69) and (7.70) may be written in the following matrix form;

$$\begin{bmatrix} a_l^+(r) \\ a_l^-(r) \end{bmatrix} = \begin{bmatrix} T_{11} & T_{12} \\ T_{21} & T_{22} \end{bmatrix} \begin{bmatrix} a_l^+(R_1) \\ a_l^-(R_1) \end{bmatrix} \tag{7.71}$$

where

$$T_{11}(r) = e^{j\Delta\beta(r-R_1)}\{cosh[s(z)(r-R_1)] + (\frac{\alpha - j\Delta\beta}{\gamma})sinh[\gamma(r-R_1)]\} \tag{7.72}$$

$$T_{12}(r) = -(-1)^l(\frac{\kappa_m}{s(z)})e^{j\Omega m}e^{j\Delta\beta(r+R_1)}sinh[s(z)(r-R_1)] \tag{7.73}$$

$$T_{21} = -(-1)^l(\frac{\kappa_m}{s(z)})e^{-j\Omega m}e^{-j\Delta\beta(r+R_1)}sinh[s(z)(r-R_1)] \tag{7.74}$$

$$T_{22} = e^{-j\Delta\beta(r-R_1)}\{cosh[s(z)(r-R_1)] + (\frac{\alpha - j\Delta\beta}{s(z)})sinh[s(z)(r-R_1)]\} \tag{7.75}$$

$$s(z) = \sqrt{\kappa_m^2 + z^2} \tag{7.76}$$

$$z = \Delta\beta + j\alpha \tag{7.77}$$

121

7.3.4 Gain Threshold Condition of the CG-DFB laser

In the present case, the only difference between the waveguide of the grating region and that of the unperturbed centre is a small periodic perturbation, the field therefore sees no discontinuity at the boundary $r = R_1$ and the matrix relating the field amplitudes at the centre of the structure to those at $r = R_2$ is derived from a multiplication of (7.68) and (7.71) as:

$$
\begin{bmatrix} a_l^+(R_1) \\ a_l^-(R_1) \end{bmatrix} = \begin{bmatrix} e^{\alpha R_1} & 0 \\ 0 & e^{-\alpha R_1} \end{bmatrix} \begin{bmatrix} a_l^{+'}(0) \\ a_l^{-'}(0) \end{bmatrix}
\tag{7.78}
$$

It is known [25] that in order to create self-sustaining oscillations, the ratio of the outgoing to the in-going waves must be zero at $r = R_2$, so that:

$$
\frac{a_l^-(R_1)}{a_l^+(R_1)} = 0
\tag{7.79}
$$

Combining (7.79) and (7.78) results in the following equation for the threshold condition;

$$
\rho_0 \rho_{R_1} e^{2\alpha R_1 - j\Omega m} = 1
\tag{7.80}
$$

where $\Omega = \frac{\pi}{\Lambda} m(W_1 + 2R_1)$ is the total phase shift of the grating and:

$$
\rho_0 = \frac{a_l^+(0)}{a_l^-(0)}
\tag{7.81}
$$

$$
\rho_{R_1} = -\frac{T_{21}}{T_{22}} e^{j\Omega m}
\tag{7.82}
$$

Therefore ρ_0 and ρ_{R_1} are the reflectivities at the centre of the grating and at $r = R_1$ respectively.

The reflectivity at R_1 is then given by substitution of (7.78) and (7.76) into (7.80) to give;

$$\rho_{R_1} = \frac{(-1)^l \kappa_m e^{j2\Delta\beta R_1} sinh[s(z)\Delta R]}{s(z)cosh[s(z)\Delta R] - zsinh[s(z)\Delta R]} \quad (7.83)$$

where $\Delta R = R_2 - R_1$. With the requirement that $a_n^+(0) = a_n^-(0)$, necessary to ensure a finite field at $r = 0$, the threshold condition is obtained using (7.83) and (7.80) as:

$$f_{cg}(z) = [(-1)^l \kappa_m e 2R_1 z - j\Omega + z] sinh[s(z)\Delta R] - s(z)cosh[s(z)\Delta R] = 0$$

$$(7.84)$$

With z as the independent variable, zeros of the complex function (7.84) may be sought. The modes of the CG-DFB laser in terms of particular values for gain (α) and detuning $(\Delta\beta)$ satisfying the threshold condition then follow directly.

7.3.5 Locating the Modes of a CG-DFB laser

The contours of the complex function (7.84) representing the threshold condition for a sample CG-DFB laser are shown in Figure 7.3, where $m = 1$, $\kappa_m R_1 = 1$, $R_2 = 0$, $n = even$ and $\Omega = \pi/2$.

From the figure, the function $f_cg(z)$ can be seen to have a number of poles near to the zeros representing the modes. By inspection of (7.84), the locations of the poles match those of the zeros of the function:

$$P(z) = s(z)cosh[s(z)\Delta\beta] + jzsinh[s(z)\Delta\beta] \quad (7.85)$$

123
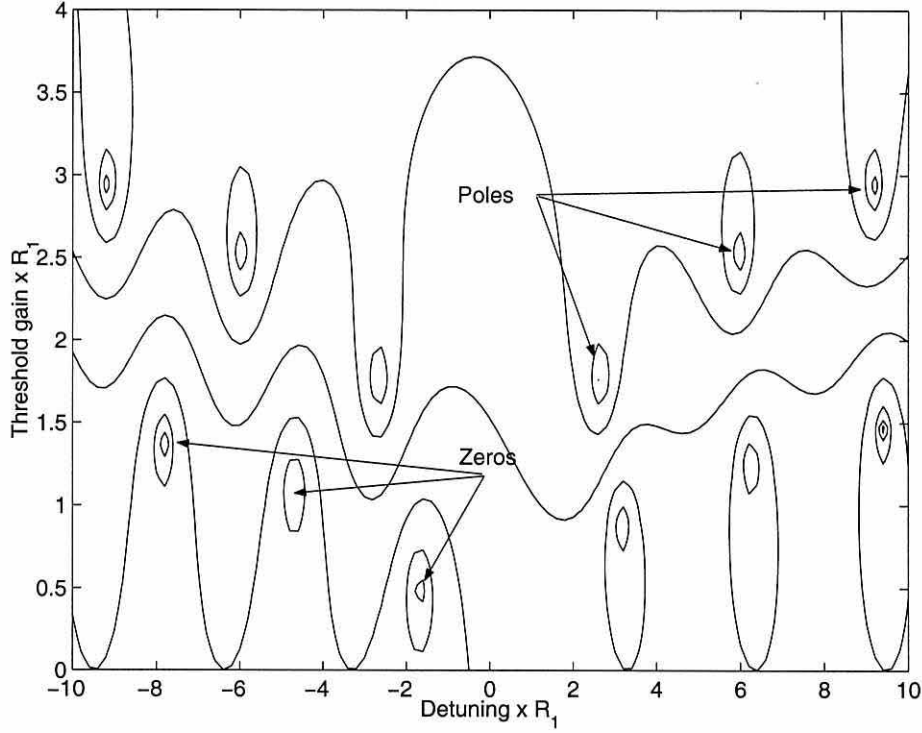
Figure 7.3: *Contour plot of $Ln(|c(z)|^2)$. The poles are the upper most features in the figure, and are symmetrical around the Bragg wavelength (Detuning=0). The zeros of the function are, for this case, asymmetric around the Bragg frequency and are seen in the lower portion of the contour.*

Locating the zeros of the threshold function $f_c g(z)$ (7.84) may therefore be undertaken using the Argument Principle Method (APM) of Section 2.5. This is achieved by first performing the APM using (7.85) to locate the poles of $f_c g(z)$. For each pole found, a contour integral may be evaluated numerically around a circular path, c_o, of small radius enclosing the 0th singularity. The result of the integration may then be subtracted from the integral used in the APM computation, so that

124

$$S_m = \frac{i}{2\pi} \left(\oint z^m \frac{f'(z)}{f(z)} dz - \sum_{o=0}^{p} \oint_{c_o} z^m \frac{f'_{cg}(z)}{f_{cg}(z)} dz \right) \qquad (7.86)$$

Where P is the number of poles of $f_{cg}(z)$ within the region bound by C, obtained by a numerical evaluation of the integral:

$$p = \frac{i}{2\pi} \oint_C \frac{P'(z)}{P(z)} dz \qquad (7.87)$$

7.4   Discussion

It has been shown in this chapter, how the coupling of modes in a circularly symmetric grating structure may be analysed. The field in a CG-DFB structure may be decomposed into a axially variant profile similar to that of a one dimensional planar waveguide, a periodic azimuthal component, and a radially variant field described by Bessel functions. The mode orders of the three components are independent of each other. Unlike coupling in a linear(parallel) grating DFB structure, TE-TM mode coupling is a feature of circular DFBs at cylindrical mode orders higher than the fundamental. This arises because, at small radii, the modes are dissimilar to the TE and TM modes of Cartesian planar structures, having non-zero E_z and H_z components respectively. As the radius increases however, and the curvature of the structure becomes less severe, the modes behave more like those in a parallel grating. If a large grating radius is assumed, the Bessel form of the radial field component may be replaced by an exponential approximation, and the corresponding equations for the coupling of the grating simplify considerably. A single complex expression describing the threshold condition of a CG-DFB

laser may then be derived, the zeros of which correspond to the oscillating modes. The modes are then sought using an adaptation of the APM method used in the analysis of parallel grating structures.

Chapter 8

Investigation of Optimum geometries for CG-DFB OSLs

8.1 Introduction

In the preceding chapters it has been seen how the use of particular lithographic techniques unique to organic materials leads to the consideration of non-parallel DFB gratings as a practical means of fabricating low volume, low threshold gain organic DFB lasers. Circularly symmetric DFB gratings are of particular interest due to their ability to confine emission in the plane of the laser. This is expected to lead to lower gain thresholds for smaller devices. It has also been suggested [27] that so-called Circular Grating Distributed Feed-Back Organic Semiconductor Lasers (CG-DFB OSLs) may also be fabricated using a second order grating leading to emission vertically from the cavity. Vertical emission and low volume make CG-DFB OSLs attractive for use in low-cost VCSEL arrays.

In this chapter, the techniques examined in Chapters 6 and 7 are employed in the analysis of a CG-DFB OSL design.

8.2 CG-DFB OSL Construction

The transverse structure of the CG-DFB OSL is shown in Figure 8.1. The layer structure is composed of Alq_3, with an Alq_3:DCM active region. The operating wavelength of the laser is taken to be around 630nm.

Consideration is given to a CG-DFB OSL having an annular grating with an outer radius, R_1 an inner radius R_2 and an unperturbed centre section. The air or substrate interface is the most likely location for the grating using soft lithographic fabrication techniques, as the grating may be formed either
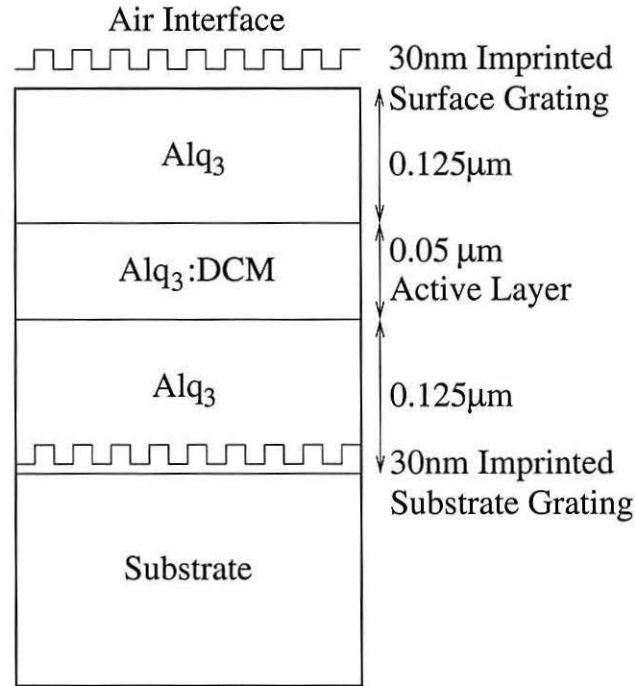
Figure 8.1: *Transverse Structure of the CG-DFB OSL. The grating is shown at the two most likely sites for fabrication, the air and substrate interfaces.*

prior to or after deposition of the laser multilayer, reducing the complexity of fabricating the device.

8.3 Threshold Gain Analysis of the CG-DFB OSL

8.3.1 Transverse Modes

In Section 7.2, it was shown how the field in the CG-OSL may be separated into Transverse (z dependent), Azimuthal (θ dependent) and Radial (r

dependent) components. The transverse modes can therefore be calculated separately as plane wave solutions to the Helmholtz equation for TE or TM modes of a slab waveguide, as in Chapter 2.

The use of Alq$_3$:DCM as the lasing materials permits the results of the threshold gain and threshold current analysis of previous chapters to be used in the analysis of the transverse (z dependent) waveguide. The transverse structure shown in Figure 8.1 is therefore known to support a single transverse TE mode, with a confinement of $\Gamma_z = 0.18$ and an effective index of $n_{eff,z} = 1.6083$.

8.3.2   Coupling of the Grating

It was noted in Section 7.2 that the coupling coefficient for the TE-TE mode coupling of a circularly symmetric grating in a single transverse mode CG-DFB laser is calculated in precisely the same manner as for a parallel (linear) grating DFB. Furthermore, under the large radius approximation, coupling between modes of differing polarisation (i.e. TE-TM and TM-TE mode coupling) is negligible. The TE-TE coupling coefficients for an air interface and substrate interface grating can therefore be obtained from the analysis of Chapter 4 as;

$$\kappa_{sg} = 352 cm^{-1} \tag{8.1}$$

for the substrate grating, and

$$\kappa_{ag} = 336 cm^{-1} \tag{8.2}$$

130

for the grating at the air interface. A sinusoidal grating of wavelength $\Lambda = 200nm$ and a depth (tooth-height) of $d = 30nm$ is adopted for a first order $l = 1$ grating.

The coupling coefficients for the two grating positions are not significantly different, and in the remaining analysis $\kappa = \kappa_{ag} \approx \kappa_{sg} = 350cm^{-1}$ is chosen as the TE-TE coupling coefficient.

8.3.3 Radial and Azimuthal Modes

To locate the cylindrical modes of the laser, roots are sought to the threshold gain equation;

$$f_{cg}(z) = [(-1)^l \kappa_m e 2R_1 z - j\Omega + z]sinh[s(z)\Delta R] - s(z)cosh[s(z)\Delta R] \quad (8.3)$$

using the adaptation of the APM described in Section 7.3.

Figure 8.2 shows the mode spectrum for a grating having an outer radius of $R_1 = 20\mu m$. The inner radius $R_2 << R_1$, so that R_2 may be set to be zero in the analysis. As the geometry at the centre of the grating will still effect the phase Ω of the grating, mode spectra for $\Omega = 2\pi$ and $\Omega = \pi/2$ are shown in the figure.

It may be seen in (8.3) that, due to the presence of the term $(-1)^l$, the even and odd order modes (of order l) will have different threshold gain conditions, and are sought separately. The even and odd order modes are distinguished on Figure 8.2, where it can be seen that they are degenerate for $\Omega = \pi/2$. In fact, the degeneracy of the modes is broken by the slightly better spatial confinement of the odd order modes resulting in a marginally lower

131
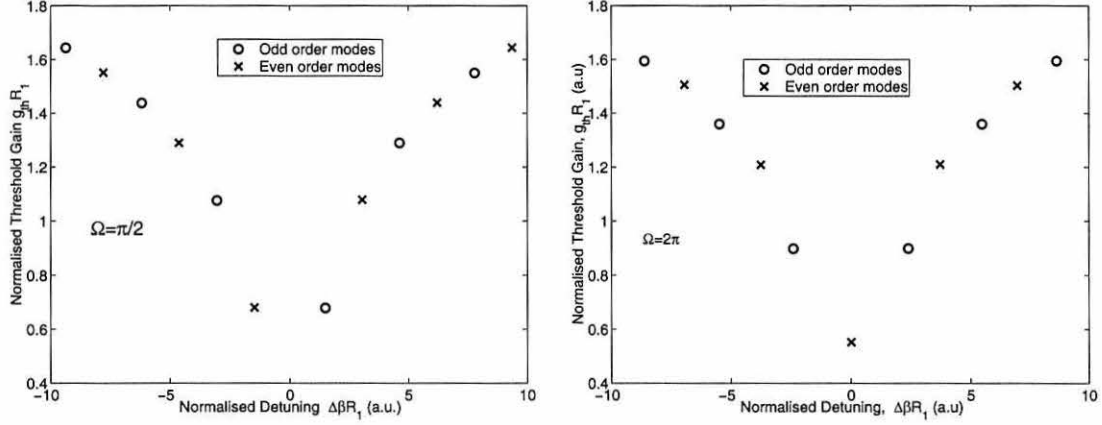
Figure 8.2: *Mode Spectra for a circular grating DFB having $R_1 = 20\mu m$. Spectra are shown for gratings having $\pi/2$ and 2π phase shifts at the centre of the grating.*

threshold gain. With $\Omega = 2\pi$, a single fundamental mode is seen oscillating at the Bragg wavelength with a threshold gain of $g_{th} = 200cm^{-1}$.

The situation is somewhat similar to that of a parallel (linear) grating DFB or DBR laser with a phase shift. As Ω is varied between 2π and $\pi/2$, the modes precess around a relatively simple line function. The threshold gain of the fundamental mode at $\Omega = 2\pi$ therefore has the lowest gain attainable for this grating.

8.3.4 Grating Radius

The relationship between the radius of the grating, R_1, and the threshold gain of the modes is shown in Figures 8.3 and 8.4. Results are shown for the lowest order odd and even modes of the laser. The fundamental even order mode at $\Omega = 2\pi$ retains the lowest gain threshold, however the difference

132

between the thresholds of the modes decreases as the R_1 gets larger.

Figure 8.3: *Variation in threshold gain of the modes of a CG-DFB OSL with radius R_1 and a phase shift of $\Omega = 2\pi$.*

8.3.5 Changing the Radius of the Inner Section

As well as affecting the phase of the CG-DFB structure, the radius of the inner section, R_2, is also expected to alter the threshold gain characteristic of the laser.

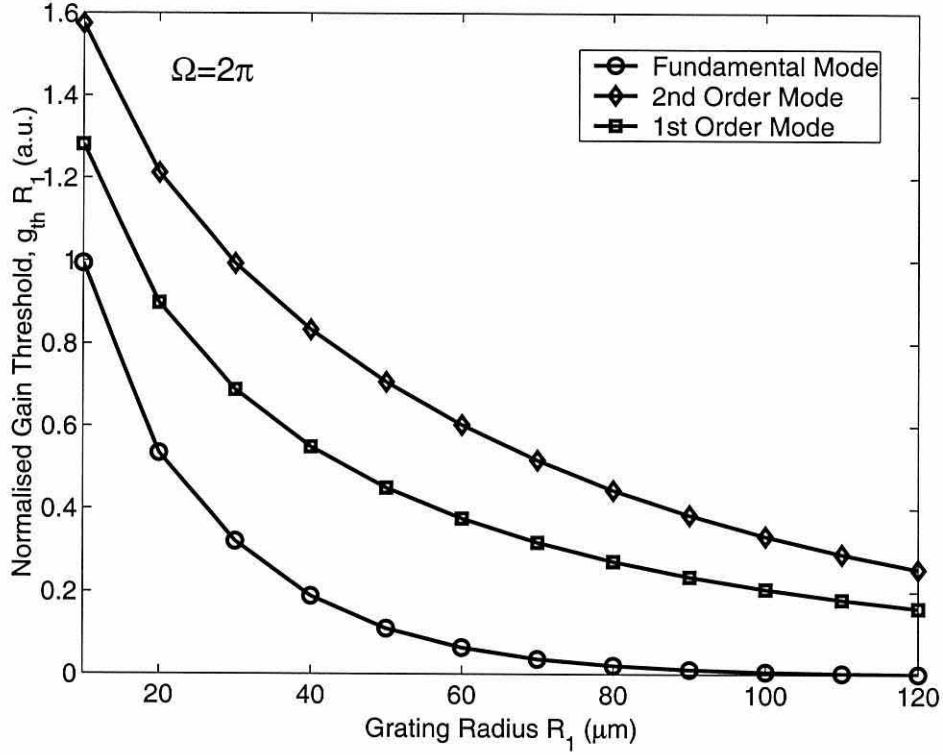Figure 8.5 shows the mode spectrum of a CG-DFB laser with $R_1 = 20\mu m$ and $R_2 = 1\mu m$. Comparison with Figure 8.2 shows how the presence of
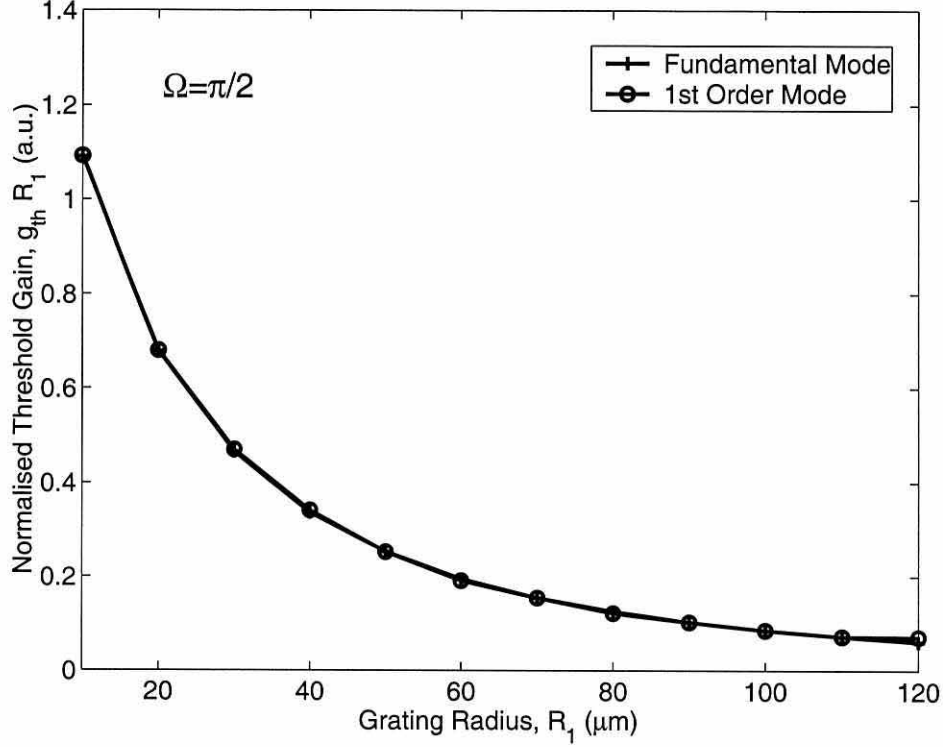
Figure 8.4: *Variation in threshold gain of the modes of a CG-DFB OSL with radius R_1 and a phase shift of $\Omega = \pi/2$.*

even a small unperturbed centre section results in an asymmetrical mode distribution around the Bragg wavelength. The modes lasing at wavelengths lower than the Bragg wavelength are more widely spaced and have lower threshold gains while the modes on the positive side of the detuning axis have higher threshold gain and are more narrowly spaced spectrally.

The reason for the spectral distortion may be seen by consideration of the modes of a parallel grating DBR laser, which the CG-DFB closely resembles in behaviour. In a DBR laser, gain is normally present in the central, un-
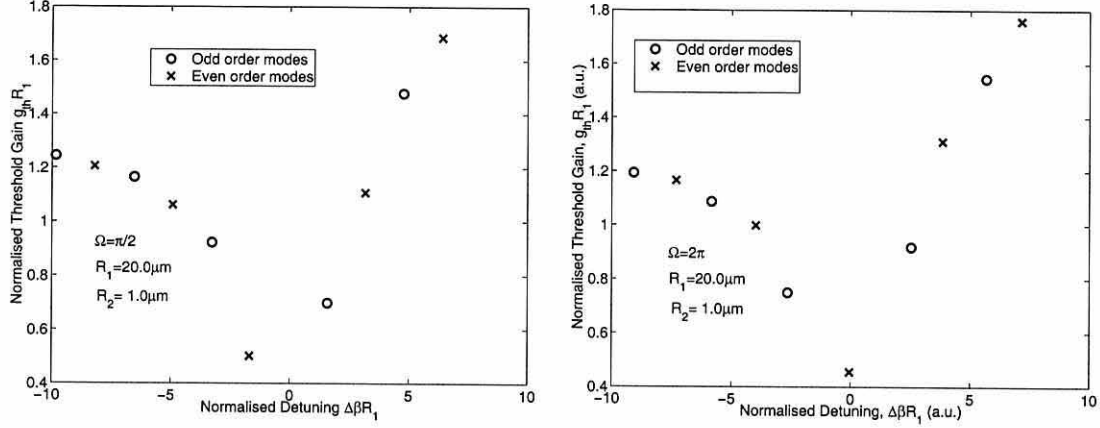
Figure 8.5: *Mode Spectra for a circular grating DFB having $R_1 = 20\mu m$ and $R_2 = 1\mu m$. Spectra are shown for gratings having $\pi/2$ and 2π phase shifts at the centre of the grating.*

perturbed region only, and the modes of this cavity form the mode spectrum of the laser. In the CG-DFB laser, the modes in the active grating region are the dominant modes of the device. As the size of the unperturbed section becomes non-zero, however, DBR-like modes are possible, albeit highly detuned and with much higher gain thresholds than the CG-DFB modes. Although not the operational modes of the laser, the DBR-like modes do influence the mode spectra of the CG-DFB modes. The resulting asymmetry of the modes may thus be due to the detuning of the DBR-like mode, governed by the phase change of the cylindrical wave as it traverses the unperturbed cavity.

Figure 8.6 shows how the threshold gains of the modes change with increasing inner radius (R_2). It can be seen in the figure that the negatively detuned modes are greatly affected by variations in R_2. As R_2 is increased

135

Figure 8.6: *Variation in threshold gain of the modes of a CG-DFB OSL with radius R_2.*

to around $5\mu m$ the fundamental mode reaches cut-off at the origin of the gain axis. Whether the use of larger unperturbed centre sections to further reduce the threshold gains of detuned modes is a practical possibility is a matter for experimental investigation.
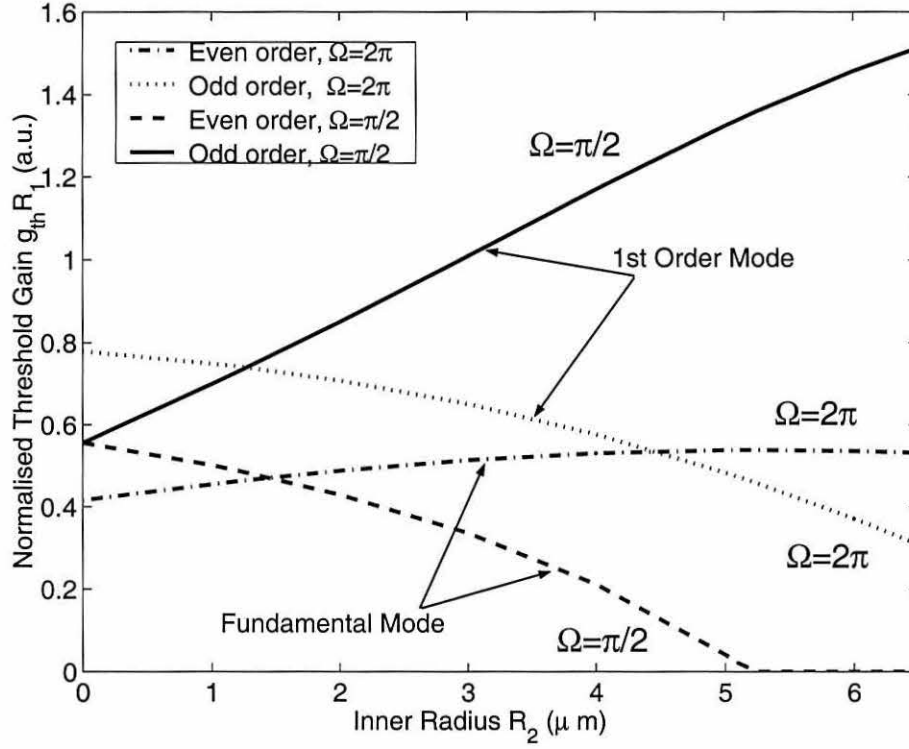
136

8.4 Threshold Current Analysis of the CG-DFB OSL

8.4.1 Threshold Current Optimisation of the Transverse Structure

The gain coefficient for the Alq$_3$ DCM material of the CG-DFB OSL is given , from Section 6.3.1, as $A_0 = 1 \times 10^{-18} cm^2$. As the transverse ($z$ dependent) modes of the CG-OSL are separable from the cylindrical waves and resemble closely the modes of a simple planar waveguide, the current threshold optimisation of the transverse structure is identical to that for the linear (parallel) grating DFBs discussed in Chapters 4,5 and 6.

8.4.2 Threshold Current Optimisation of the Grating Radius

The dependence of the threshold current density on the radius of the grating R_1 is shown in Figure 8.7, where it is seen that for the fundamental radial mode, a threshold current density of around $80Acm^{-2}$ is obtained using a radius of around $100\mu m$. This may be compared with the parallel grating device described in Section 6.3, which required a $2cm$ long grating to achieve similar values for the threshold current density. This illustrates the compact geometry of the CG-DFB design in comparison with linear structures.

Unlike linear structures, where the area of the grating (and therefore the net threshold current) increases proportionally with its length, the area of
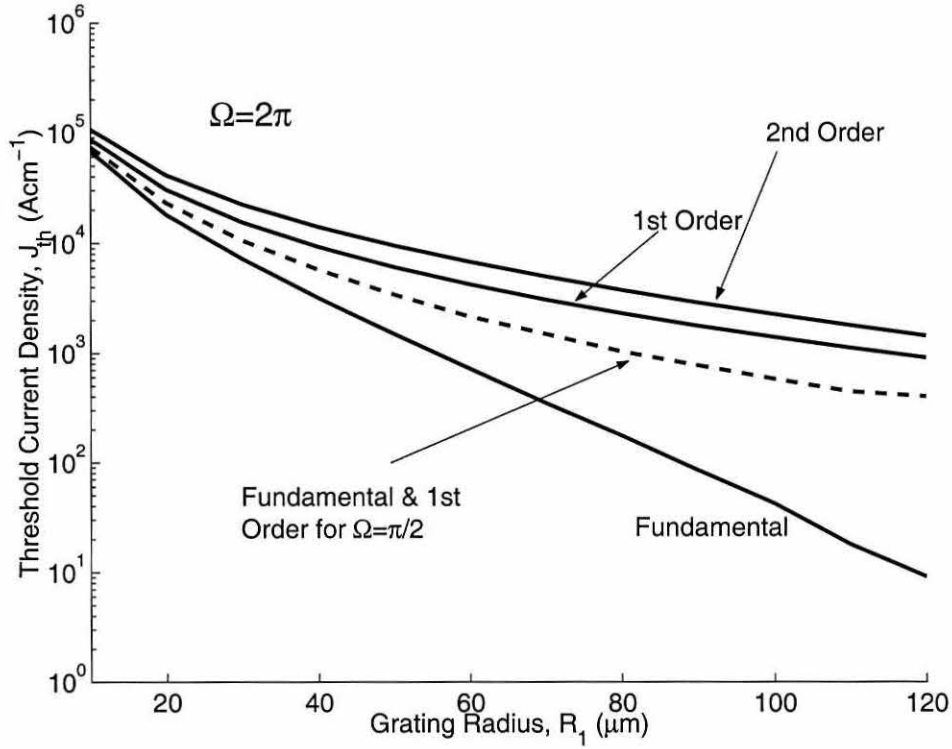
Figure 8.7: *Effect of outer grating radius R_1 on threshold gain of a CG-DFB OSL with $\Omega = 2\pi$. The dashed line indicates the degenerate fundamental and first order modes for a $\Omega = \pi/2$ grating.*

a CG-DFB scales with R_1^2. The greater increase in pump area with grating radius may possibly counteract the increase in coupling coefficient, it is therefore of interest to determine the effect of changing the grating radius on the net current applied to the device.

Figure 8.8 shows how varying the radius R_1 affects the net threshold current in the CG-DFB OSL. It can be seen that, for the fundamental mode of the laser, the net threshold current reaches a peak at around $R_1 = 20\mu m$. For

138

higher order modes, the current peak appears at larger radii. In general, the maximum in the net current occurs when the reduced losses of a larger grating overcome the increase in pumping area. It can be seen from the fundamental mode that the net threshold current reduces approximately exponentially after $R_1 = 40nm$.

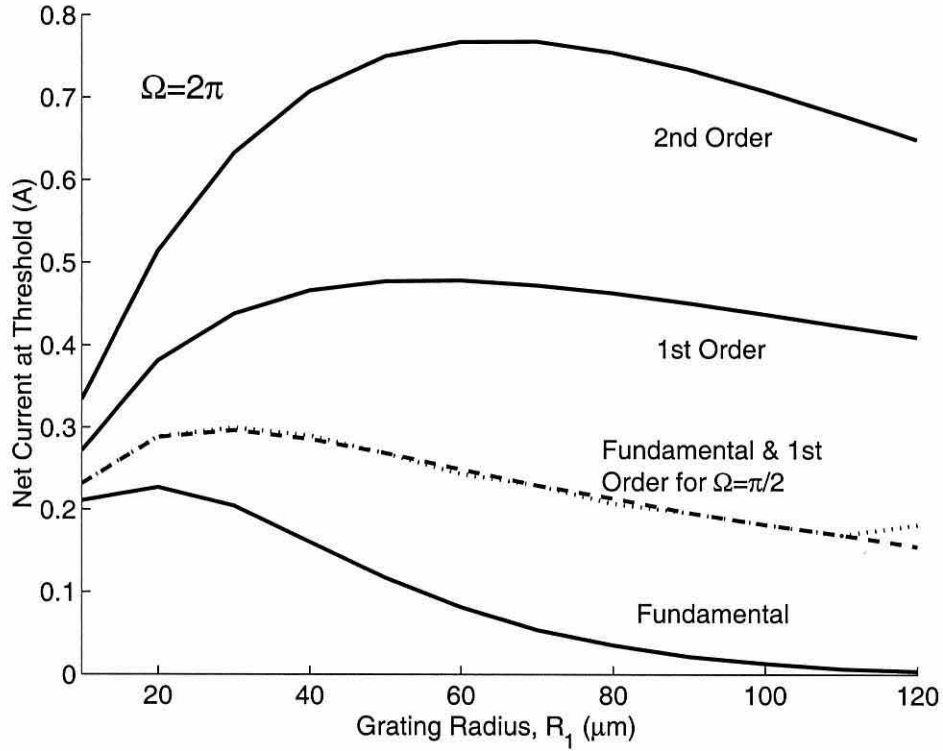Figure 8.8: *Effect of the outer grating radius R_1 on the net threshold current for the first three modes of a CG-DFB OSL with $\Omega = 2\pi$. The dashed line represents the degenerate fundamental and first order modes of a similar structure having $\Omega = \pi/2$*

8.5 Discussion

A gain threshold and current threshold analysis of a CG-DFB OSL design has been performed where the threshold gain and detuning of the cylindrical modes of the CG-DFB OSL are found using the APM technique discussed previously in Section 7.3.5. It has been shown that the threshold gains of the modes may be reduced by increasing the outer radius (R_1) of the grating and that the mode spectra also depends greatly upon the total change in phase experienced by the cylindrical wave. The phase of the grating is dictated by varying the size of an unperturbed central section. Increasing the size of the inner section radius R_2, however, to just a few microns results in an asymmetrical distortion of the mode spectra around the Bragg wavelength. The spectral distortion is possibly due to the influence of DBR-like modes arising from the presence of the unperturbed gain section at the centre.

Designing the CG-DFB OSL using Alq$_3$:DCM as the active material allows the current threshold of the device to be estimated as the gain coefficient of Alq$_3$ was calculated in Section 6.3. A threshold current density of $80 Acm^{-2}$ is achieved using a grating radius of order $100\mu m$. This may be compared to the linear structure described in [20], which required a grating length of $2cm$ to achieve similar results. As the surface area over which the current density must be maintained does not vary linearly with R_1, the net current at threshold for each cylindrical mode order peaks at particular value of R_1 where the reduction in losses in the laser begins to overcome the increase in surface area.

From the preceding analysis, it is concluded that CG-DFB lasers are an

excellent candidate for the implementation of Organic Semiconductor lasers due to their low threshold gains and small size. The low threshold gain is attributed to the low loss confinement in the plane of the device and the particularly high coupling coefficients seen using DBR gratings in Organic Lasers.

Chapter 9

Conclusion

9.1 Discussion

In the preceding chapters, the characteristics of several designs of Organic Semiconductor Lasers have been investigated using a variety of numerical techniques.

In Section 3.1 attention is initially given to a prototype, optically pumped, 630nm Alq$_3$:DCM OSL chosen from the literature [16]. Methods by which the modes of the OSL might be sought are discussed in Chapter 2 where a novel technique is described that uses the Argument Principle Method (APM), to determine the complex propagation constants of the modes of a multi-layer planar waveguide. The APM method has the advantage that is requires no initial guess and locates all the modes within a defined region of the solution space.

Using the APM method, the modes are sought for the gain guided OSL structure. It is shown in Section 3.2 that the 50μm wide pump region of this laser results in multi-mode operation at a gain threshold of 100cm^{-1}. In order to achieve single mode operation, a Ridge (or Rib) guiding configuration is considered in Section 3.3. The Rib guiding waveguide is single moded, but is found to have a lower lateral confinement than the multi-mode gain-guided design. The height of the Rib may be altered to maximise the lateral confinement, however, and it is found that a maximum lateral confinement of around 70% may be obtained before cut-in of the first order mode. The Rib waveguide design also has the advantage that the lateral confinement becomes independent upon the degree of pumping , and although the width of the rib is small ($\approx 50\mu m$) the pump can be focussed over a much wider

143

area without affecting the modes of the laser.

As a result of the low refractive indices (≈ 1.5) typical of organic semiconductor materials, the reflectivities of the end facets of the laser are found to be low ($\approx 7\%$), the use of DFB gratings as a means of further reducing the threshold gain is the subject of Chapters 4 and 5.It is shown in Chapter 4 how the APM may be adapted to find the longitudinal modes of a DFB laser as an extension to the widely used Coupled Mode Theory. DFB gratings at the surface and substrate interfaces of the laser are of particular interest in the analysis as they may be fabricated using a novel, potentially low-cost 'Contact Imprinting' technique particular to organic materials.

The coupling of surface and substrate gratings is found to be particularly good in organic multi-layers due to the comparatively small index steps typically seen at these interfaces. Gratings having rectangular, sinusoidal and triangular profiles are analysed in Section 5.3, where it is seen that rectangular gratings offer slightly superior confinement than sinusoidal profiles, while the sinusoidal grating achieves better rejection of higher grating orders.

Using a 30nm deep sinusoidal grating having a period of about $200nm$, a laser cavity length of $50\mu m$ is required to give the same threshold gain as the $500\mu m$ Fabry-Perot OSL, demonstrating the much higher degree of longitudinal confinement of DFB lasers.

A threshold current analysis of a DFB OSL is described in Chapter 6. The gain threshold of Alq$_3$:DCM is calculated by a comparison of experimental results on a $2cm$ long DFB-OSL documented in [20] with a numerical analysis of an equivalent structure performed using the techniques described in Chapter 4. The experimental device was predicted to achieve lasing under

144

electrical pumping at current densities of about $80 Acm^{-2}$. The transverse structure of the OSL can be optimised to give a $\approx 30 - 40\%$ reduction in threshold current.

The high confinement of the longitudinal field in the DFB OSLs analysed in Chapters 5 and 6 is at the cost of useful emission from the structure. However, a Circular Grating (CG)-DFB OSL may avoid this problem by emitting light vertically, through the comparatively transparent transverse layer structure. The CG-DFB OSLs analysed in Chapters 7 and 8 offer lower lasing thresholds than linear DFBs and occupy a much smaller surface area, making them suitable for possible applications in organic VCSEL arrays. The initial analysis of this structures suggests that current thresholds of less than $80 Acm^{-2}$ are possible for CG-DFBs having a grating radius of just $100 \mu m$. A consideration in the design of CG-DFB OSLs is the inner radius of the grating, causes distortion of the mode spectra when it is larger than a few microns.

9.2   Review

It has been seen that the geometry of Organic Semiconductor Lasers may be designed using a range of analytic techniques equally applicable to lasers made from in-organic materials. The main adaptations from traditional analysis techniques involve the use of unusually low refractive indices for the materials, and in the calculation of the threshold current. The exceptionally small gain coefficients seen in OSL lasers indicate that exceptionally low gain thresholds are required to achieve attainable levels of threshold current. The

145

provision of low gain threshold is achieved by the reduction of losses from the laser, which unfortunately also reduces the degree of emission. Although such operational characteristics are yet to be determined, it is anticipated that OSLs will be initially useful mainly in low-power applications.

9.3 Future Work

The work presented in this thesis has been concerned with Alq_3:DCM lasers because of the large amount of information available on this material system. As experiments using other materials continue, it is becoming possible to perform similar analyses of lasers utilising Polymers and other organic materials.

In lasers using the Alq_3:DCM material, the current analysis may be expanded to include the creation of a dynamical model of an OSL. Such work would be of significant interest because of the various dynamical processes relating to inter system crossing and polaron absorption typically seen in these materials. These effects have recently been well characterised [20], and the required time constants, along with information from the static analysis covered in this work could be inserted into a rate equation model to yield a valuable insight into this aspect of OSL design.

Further analysis of CG-DFB OSLs would also be a matter for future work, particularly in the area of using second order gratings to couple light out of the cavity. As CG-DFB OSLs have yet to be fabricated at the time of writing, it is also suggested that an experimental study of these lasers is timely.

Appendix A

Maxwells Equations in Isotropic Media

The standard analysis of optical waveguides begins with Maxwells equations governing the interaction of the electric and magnetic fields in a dielectric media

$$\nabla \times \mathbf{H} = \mathbf{I} + \frac{\partial \mathbf{D}}{\partial t} \qquad (A.1)$$

$$\nabla \times \mathbf{E} = -\frac{\partial \mathbf{B}}{\partial t} \qquad (A.2)$$

Where ∇ is the Laplacian operator, $\mathbf{H}$ is the vector field of magnetic flux, $\mathbf{I}$ is the current density vector through the media, $\mathbf{E}$ is the vector field of electric flux. $\mathbf{D}$ and $\mathbf{B}$ are the electrical and magnetic displacement vectors respectively, related to the vector fields by

$$\mathbf{D} = \epsilon_0 \mathbf{E} + \mathbf{P} \qquad (A.3)$$

$$\mathbf{B} = \mu_0 (\mathbf{H} + \mathbf{M}) \qquad (A.4)$$

Where P and M are the electric and magnetic polarisations of the medium. The electric polarisation, P, can be described as the dipole moment per unit volume of the material and is defined as $\mathbf{P} = \epsilon_0 \chi_e \mathbf{E}$. Where χ_e is, in general, a tensor of rank two. For the case of an isotropic material however, χ_e is scalar and substitution into (A.3) gives

$$\mathbf{D} = \epsilon_0 \mathbf{E} (1 + \chi_e) \qquad (A.5)$$

A relative permittivity can then be defined as $\epsilon_r = 1 + \chi_e$. The magnetic polarisation $\mathbf{M} = \chi_h \mathbf{H}$ can also be treated in a similar manner, with the

148

tensor χ_h reducing to a scalar quantity in the case of an isotropic media. Making the substitutions $\epsilon = \epsilon_0 \epsilon_r$ and $\mu = \mu_0 \mu_r$ results in the following simplified forms for equations (A.3) and (A.4)

$$\mathbf{D} = \epsilon \mathbf{E} \tag{A.6}$$

$$\mathbf{B} = \mu \mathbf{H} \tag{A.7}$$

Making the simplifying assumption that the current density in the media is zero, the substitution of (A.6) and (A.7) into (A.1) and (A.2) gives

$$\nabla \times \mathbf{H} = \epsilon \frac{\partial \mathbf{E}}{\partial t} \tag{A.8}$$

$$\nabla \times \mathbf{E} = -\mu \frac{\partial \mathbf{H}}{\partial t} \tag{A.9}$$

Taking the vector curl on both sides of each equation results in the expressions

$$\nabla \times (\nabla \times \mathbf{H}) = \epsilon \frac{\partial}{\partial t} (\nabla \times \mathbf{E}) \tag{A.10}$$

and

$$\nabla \times (\nabla \times \mathbf{E}) = -\mu \frac{\partial}{\partial t} (\nabla \times \mathbf{H}) \tag{A.11}$$

The preceding may then be simplified using the vector identity

$$\nabla \times (\nabla \times \mathbf{F}) = (\nabla \cdot \mathbf{F}) \nabla - \nabla^2 \mathbf{F} \tag{A.12}$$

It is a direct result of electrostatics that the divergence of an electric or magnetic field is zero in free space (to be otherwise would require an elementary charge to exist in an infinitesimally small volume), hence $\nabla \cdot \mathbf{E} = 0$ and with the substitution of (A.6) and (A.7), the previous expression takes the form of the wave equations

$$\nabla^2 \mathbf{H} = \mu\epsilon \frac{\partial^2}{\partial t^2} \mathbf{H} \qquad (A.13)$$

and

$$\nabla^2 \mathbf{E} = \mu\epsilon \frac{\partial^2}{\partial t^2} \mathbf{E} \qquad (A.14)$$

Solutions to these equations, in the form of the $\mathbf{H}$ and $\mathbf{E}$ vector wave functions thus represent the state of the optical field throughout a a structure defined by spatial variations of μ and ϵ. It can be seen from equations (A.8) and (A.9) that only one of the above two functions needs to be solved to describe both the magnetic and electric components of the optical field. As the two wave functions are identical in form, it is convenient to discuss only one component, conventionally the electric field.

For the dielectric materials of interest in this work, only the dielectric constant $\epsilon_r(\mathbf{r})$ is taken to vary in an inhomogeneous structure. The vector field is a function of both the spatial coordinates, $\mathbf{r}$, and time, t. The time dependence of the field is normally taken to be of the form $\mathbf{E}(\mathbf{r}, t) = \mathbf{e}(\mathbf{r}, t)e^{j\omega t}$, as arbitrarily time varying fields can be analysed as a Fourier synthesis of harmonic components. If the index of refraction is defined as $n(\mathbf{r}) = \sqrt{\epsilon_r(\mathbf{r})}$, the wave-function becomes

$$\bigtriangledown^2 \mathbf{e}(\mathbf{r}) = k_0^2 n^2(\mathbf{r})\mathbf{e}(\mathbf{r}) \qquad\qquad (A.15)$$

Where $k_0 = \omega\sqrt{\mu\epsilon_0}$ is the free space wavenumber. In the case of a propagating plane wave, $k_0 = 2\pi/\lambda$. The time dependence of the $\mathbf{E}(\mathbf{r}, \mathbf{t})$ field has been suppressed in (A.15), the wave-function $\mathbf{e}(\mathbf{r})$ is therefore taken to be an envelope function for the time varying field.

Appendix B

TM Layer Matrices

For the evaluation of TM modes, the m_j matrices for the layers of the waveguide, are replaced with:

$$m_j = \frac{n_{j-1}}{2n_j} \begin{bmatrix} (\frac{n_j^2}{n_{j-1}^2} + \frac{\alpha_j}{\alpha_{j-1}})exp(-w_j) & (\frac{n_j^2}{n_{j-1}^2} - \frac{\alpha_j}{\alpha_{j-1}})exp(w_j) \\ (\frac{n_j^2}{n_{j-1}^2} - \frac{\alpha_j}{\alpha_{j-1}})exp(-w_j) & (\frac{n_j^2}{n_{j-1}^2} + \frac{\alpha_j}{\alpha_{j-1}})exp(w_j) \end{bmatrix} \quad \text{(B.1)}$$

The multiplication of these matrices to produce the dispersion matrix M then follows as for the TE solutions (Section 4.02).

In Section 4.03, it is shown that the Cauchy integral used to locate the zero's of the dispersion relation requires the derivative of the function with respect to the independent variable, U. $\frac{\partial M}{\partial U}$ can be found by applying the product rule to the individual layer matrices providing the derivatives of the individual layer matrices, m_j's are known. The derivatives of the m_j's can be found via the chain rule and are:-

$$d_j = C \begin{bmatrix} ((\frac{\alpha_{j-1}\alpha_j' - \alpha_j\alpha_{j-1}'}{y}) - x(p+z))exp(-w_j) & ((\frac{\alpha_j\alpha_{j-1}' - \alpha_{j-1}\alpha_j'}{y}) + x(p-z))exp(w_j) \\ ((\frac{\alpha_j\alpha_{j-1}' - \alpha_{j-1}\alpha_j'}{y}) - x(p-z))exp(-w_j) & ((\frac{\alpha_{j-1}\alpha_j' - \alpha_j\alpha_{j-1}'}{y}) + x(p+z))exp(w_j) \end{bmatrix}$$
$$\text{(B.2)}$$

Where:

$$x = \alpha_j' wj \qquad y = \alpha_{j-1}^2 \qquad z = \frac{\alpha_j}{\alpha_{j-1}} \quad \text{(B.3)}$$

For the TE modes;

$$C = \frac{1}{2} \qquad p = 1 \quad \text{(B.4)}$$

!dand for the TM Modes:

$$C = \frac{n_{j-1}}{2n_j} \qquad p = \frac{n_{j-1}^2}{n_j^2} \qquad\qquad (B.5)$$

The derivative of the α's with respect to U is obtained by differentiation of equation 4.19 in Section 4.03, and can be simplified to:

$$\frac{\partial \alpha_j}{\partial U} = \frac{\alpha_j \alpha_0}{U \alpha_j} \qquad\qquad (B.6)$$

Bibliography

[1] Amnon Yariv, *Optical Electronics, Fourth Edition*, Chapters 1,2,13 Saunders College Publishing, 1991.

[2] G.P. Agrawal and N.K. Dutta, *Long-Wavelength Semiconductor Lasers*, Chapters 2,7 Van-Nostrand Reinhold, 1986.

[3] E. Anemogiannis and E.N. Glytsis, "Multilayer Waveguides: Efficient Numerical Analysis of General Structures," *Journal of Lightwave Technology*, **10**, 10, pp. 1344-1351, 1992.

[4] K.H. Shlereth and N. Tacke, "The Complex Propagation Constant of Multilayer Waveguides: An Algorithm for a Personal Computer," *IEEE J. Quantum Electron.*, **26**, 4, pp. 637-630, 1990.

[5] R.E. Smith, S.N. Houde-Walter and G.W. Forbes, "Mode Determination for Planar Waveguides Using the Four-Sheeted Dispersion Relation," *IEEE J. Quantum Electron.*, **28**, 6, pp. 1520-1526, 1992.

[6] R.E. Smith, S.N. Houde-Walter and G.W. Forbes, "Unfolding the Multivalued Planar Waveguide Dispersion Relation." *IEEE J. Quantum Electron.*, **29**, 4, pp. 1031-1034, 1993.

[7] E. Anemogiannis, E.N. Glytsis and T.K. Gaylord, "Bound and Quasibound State Calculations for Biased/Unbiased Semiconductor Quantum Heterostructures," *IEEE J. Quantum Electron.*, **29**, 11, pp. 2731-2740, 1993.

[8] K.S. Chian, "Analysis of Rectangular Dielectric Waveguides: Effective-Index Method with Built-in Perturbation Correction," *Electron. Lett.*, **28**, 4, pp. 388-390, 1992.

[9] J.S. Lee and S.Y. Shin, "On the Validity of the Effective Index Method for Rectangular Dielectric Waveguides," *J. Lightwave Technol.*, **11**, 8, 1320-1324, 1993.

[10] K.S. Chian, "Analysis of the Effective-Index Method for the Vector Modes of Rectangular-Core Dielectric Waveguides," *IEEE Trans. Microwave Theory and Techniques*, **44**, 5, 692-700, 1996.

[11] K.S. Chian, "Performance of the Effective-Index Method for the Analysis of Dielectric Wave-guides," *Optics Letters*, **16**, 10, 714-716, 1991.

[12] A. Kumar, D.F. Clark and B. Culshaw, "Explanation of Errors Inherent in the Effective-Index Method for Analyzing Rectangular-core Waveguides," *Optics letters*, **13**, 12, 1129-1131, 1988.

[13] T.M. Benson, R.J. Bozeat and P.C. Kendall, "Rigorous Effective Index Method for Semiconductor Rib Waveguides," *IEE Proc. - J. Optoelectron.*, **139**, 1, 67-70, 1992.

[14] P.R Young and R.J. Collier, "Solution of Lossy Dielectric Waveguides using Dual Effective-Index Method," *Electronics Letters*, **33**, 21, 1788-1789, 1997.

[15] P.C. Kendall, M.S. Stern and P.N. Robson, "Discrete Spectral Index Method for Rib Waveguide Analysis," *Optical and Quantum Electronics*, **22**, pp. 555-560, 1990.

[16] V. G. Kozlov, V. Bulovic and S.R. Forrest, "Temperature Independent Performance of Organic Semiconductor Lasers," *Appl. Phys. Lett.*, **71**, 18, pp. 2575-2577, 1997.

[17] M. Berggren, A. Dodabalapur, R.E. Slusher, A. Timko and O. Nalamasu, "Organic solid-state lasers with imprinted gratings on plastic substrates," *Appl. Phys. Lett.*, **72**, 4, pp. 410-411, 1998.

[18] A. Dodabalapur, M. Berggren, R.E. Slusher, Z. Bao, A. Timko, P. Schiortino, E. Laskowski, H.E. Katz and O. Nalamasu, "Resonators and materials of organic lasers based on energy transfer," *IEEE J. Selected Topics in Quantum Electron.*, **4**, 1, pp. 67-74, 1998.

[19] B.L. Booth, "Low Loss Channel Waveguides in Polymers," *J. Lightwave Technol.*, **7**, pp. 1445-1453, 1989.

[20] V.G. Kozlov, G. Parthasarathy, P.E. Burrows, V.B. Khalfin, J. Wang, S.Y. Chou, and S.R. Forrest, "Structures for Organic Diode Lasers and Optical Properties of Organic Semiconductors Under Intense Optical and Electrical Excitations," *IEE J. Quantum Electron.*, **36**, 1, pp. 2596-2606, 2000.

[21] M.S. Weaver, D.G. Lidzey, T.A. Fisher, M.A. Pate, D. O'Brien, A. Bleyer, A. Tajbekhsh, D.C. Bradley, M.S. Skolnick and G. Hill, "Recent

Progress in Polymers for Electroluminescence: Microcavity Devices and Electron Transport Polymers," *Thin Solid Films*, **273**, pp. 39-47, 1996.

[22] M.D. McGhehee, M.A. Diaz-Garcia, F. Hide, R. Gupta, E.K. Miller and D. Moses, "Semiconducting polymer distributed feedback lasers," *Appl. Phys. Lett.*, **72**, 13, 1536-1538, 1998.

[23] C. Wu, T. Makino, J. Glinski, R. Maciejko and S.I. Najafi, "Self-Consistent Coupled-Wave Theory For Circular Gratings on Planar Dielectric waveguides," *J. Lightwave Technol.*, **9**, pp. 1264-1277, 1991.

[24] C. Wu, T. Makino, R. Maciejko and S.I. Najafi, "Simplified Coupled-Wave Equations for Cylindrical Waves in Circular Grating PLanar Waveguides," *J. Lightwave Technol.*, **10**, pp. 1575-1589, 1991.

[25] C. Wu, T. Makino, R. Maciejko and S.I. Najafi, M.Svilans, J. Glinski and M. Fallahi, "Threshold Gain and Threshold Current Analysis of Circular Grating DFB and DBR Lasers," *J. Quantum Electron.*, **29**, pp. 2596-2606, 1993.

[26] J.H. Schon, C.H. Kloc, A. Dodabalapur, B. Batlogg, "An Organic Solid State Injection Laser," *SCIENCE*, **289**, pp. 599-601, 2000.

[27] T. Erdogan and D.G. Hall, "Circularly Symmetric distributed feed-back semiconductor lasers: an analysis," *J. Appl. Phys.*, **68**, 4, pp. 1435-1444, 1990.

[28] N. Tessler, "Lasers based on semiconducting organic materials," *Advanced materials*, **11**, pp. 363-370, 1999.

[29] R.G. Kepler, P.M. Beeson, S.J. Jacobs, R.A. Anderson, M.B Sinclair, V.S. Valencia and P.A. Cahill, "Electron and hole mobility in *tris*(8-hydroxyquinolenolato-N1,08) aluminium," *Appl. Phys. Lett.*, **66**, 26, pp. 3618-3620, 1995.

Publications

Conference Presentations

G.F. Barlow and K.A. Shore, "Analysis of waveguide properties of organic semiconductor lasers", Polymer'98, Brighton, 1998

G.F. Barlow and K.A. Shore, "Analysis of distributed feed-back organic semiconductor lasers ", Semiconductor and Integrated Optoelectronics (SIOE'99), Aberdare Hall, Cardiff, April 1999

G.F. Barlow and K.A. Shore, Design of organic semiconductor laser structures for low threshold operation", IOP National Quantum Electronics conference (QE'14), Manchester, September 1999

G.F. Barlow and K.A. Shore, "Design of light confining structures for low threshold organic semiconductor lasers" , PREP'2000, University of Nottingham, 11-13 April 2000

G.F. Barlow and K.A. Shore, "Gain threshold optimisation of circular grat-

ing distributed feed-back organic semiconductor lasers", Semiconductor and Integrated Optoelectronics (SIOE'2000), Aberdare Hall, Cardiff, April 2000

G.F. Barlow and K.A. Shore, "Design of organic semiconductor laser structures with imprinted surface reliefs", paper QWI9, CLEO/QELS 2000, San Francisco, California USA.

G.F. Barlow and K.A. Shore, "Gain Threshold Analysis of Circular Surface Relief Distributed Feed-Back Organic Semiconductor Lasers", CLEO (Europe), paper CWK05, Nice, 10-15 September 2000

G.F. Barlow and K.A. Shore, "Threshold Current Analysis of Linear Grating Distributed Feed-Back Organic Semiconductor Lasers", IEEE LEOS 2000, 13th Annual Lasers and Electro Optics Society Meeting, Rio Grande, Puerto Rico, USA , paper WQ3, November 2000

Journal Publications

G.F. Barlow and K.A. Shore, "Analysis of waveguide properties of organic semiconductor lasers",*IEE Proc. Optoelectronics*, **146**, 15-20, 1999

G.F. Barlow and K.A. Shore, "Analysis of distributed feedback organic semiconductor lasers", *IEE Proc. Optoelectronics* ,**147**, 61-66, 2000

162

G.F. Barlow and K.A. Shore, "Design of Organic Semiconductor Laser Structures for Low Threshold Operation ", *J. Mod. Optics*, **47**, 1921-1932, 2000

G.F. Barlow and K.A. Shore, "Threshold Current Analysis of DFB organic semiconductor lasers", *IEE Proc. Optoelectronics*, Accepted for publication, 2001

G.F. Barlow and K.A. Shore, "Application of the Argument Principle Method to the Calculation of DFB Laser Diode Modes", *Int. J. Num. Model.*, Accepted for publication, 2001